Droplet impact and contact angle dynamics: From spreading and splashing to 3D printing

Miguel Angel Quetzeri Santiago

PhD Thesis

School of Engineering and Materials Science

Queen Mary, University of London

Submitted in partial fulfilment of the requirements of the

Degree of Doctor of Philosophy

May 2020

In that Empire, the Art of Cartography attained such Perfection that the map of a single Province occupied the entirety of a City, and the map of the Empire, the entirety of a Province. In time, those Unconscionable Maps no longer satisfied, and the Cartographers Guilds struck a Map of the Empire whose size was that of the Empire, and which coincided point for point with it. The following Generations, who were not so fond of the Study of Cartography as their Forebears had been, saw that that vast Map was Useless, and not without some Pitilessness was it, that they delivered it up to the Inclemency of Sun and Winters. In the Deserts of the West, still today, there are Tattered Ruins of that Map, inhabited by Animals and Beggars; in all the Land there is no other Relic of the Disciplines of Geography

—Jorge Luis Borges, *On Exactitude in Science*

An experiment is a question which science poses to Nature and a measurement is the recording of Nature's answer.

—Max Planck (1958 - 1947)

Acknowledgements

I would like to thank the National Council of Science of Technology of Mexico (CONACYT) and the Secretariat of Energy of Mexico (SENER) for their financial support.

I really want to thank my supervisor Dr. Rafael Castrejón-Pita who guide me through the PhD and help me when I needed with a lot of disposition and always with a smile. Also, I truly appreciate the help of Prof. Alfonso Castrejón-Pita, who I think of as my second supervisor. Additionally, I would like to express my gratitude to my collaborators Dr. Kensuke Yokoi and Dr. Lorenzo Botto for their assistance. I am also very grateful with Prof. Christophe Josserand, who supervised me and gave me the opportunity to gain research experience at the École Polytechnique. Thanks to my labmates and friends, Gannian, Clara and Francesco, they made my time in the lab much more enjoyable and their help and knowledge was invaluable.

In these years I made a lot of friends not only at QMUL but also outside, without hanging out with them and having small breaks from the PhD I would not have made it. I would like to thank my friends in QMUL that accompanied me through all the PhD: Jorge, Matt, Stef and Will. Likewise, I wish to thank Ana Karen, Elijah, Emilie, Ernesto, Eugenio, Gastón, Jasmin, Lino, Minerva, Soraya and Vali for the enjoyable lunch breaks and corridor conversations. Also, I am grateful to all the players in The Steven Thorpe Destroyers, my tag rugby team, game evenings made my life in London much more fun. As well, I would like to thank the two greatest flatmates I could have ever wished for, Alessandro and Carlos. The list of people would be too long if I mention everyone from whom I learned something or had a good conversation with. I am very grateful to all the people that crossed paths with me during this time.

As well, I would like to thank the del Rio Chanona family, for helping me find this PhD project and for all their advice in the application process. Specially, I would like to thank Rita for her support during the first years of my PhD.

Last but foremost, I would like to thank my parents, my sister and my grandparents for always encouraging me to continue and sending me their affection even when far.

Declaration

I, Miguel Angel Quetzeri Santiago, confirm that the research included within this thesis is my own work or that where it has been carried out in collaboration with, or supported by others, that this is duly acknowledged below and my contribution indicated. Previously published material is also acknowledged below.

I attest that I have exercised reasonable care to ensure that the work is original, and does not to the best of my knowledge break any UK law, infringe any third party's copyright or other Intellectual Property Right, or contain any confidential material.

I accept that the College has the right to use plagiarism detection software to check the electronic version of the thesis.

I confirm that this thesis has not been previously submitted for the award of a degree by this or any other university.

Signature:

Miguel A. Quetzeri Santiago

Date: 15-04-2020

Supervisory team

Primary supervisor Dr. J. Rafael Castrejón Pita

Details of collaborations

Collaborations of this thesis are:

- Chapter 2

- Prof. Alfonso A. Castrejón-Pita (Department of Engineering Science, University of Oxford, Oxford OX1 3PJ, U.K) contributed to the development of the Matlab routine to measure the dynamic contact angle.
- Dr. Kensuke Yokoi(School of Engineering, Cardiff University) performed the simulations presented in this chapter.

- Chapter 4

- Prof. Alfonso A. Castrejón-Pita (Department of Engineering Science, University of Oxford, Oxford OX1 3PJ, U.K) collaborated to the experimental work and the discussion.
- Dr. Kensuke Yokoi(School of Engineering, Cardiff University) contributed in the discussion and the model to fit the data.

- Chapter 5

- Dr. Gannian Zhang collaborated to the experimental work and the analysis.
- Dr. Lorenzo Botto (School of Engineering and Materials Science, Queen Mary University of London), contributed to the discussion.
- Corrine A. Stone provided the textile samples and revised the text.

- Chapter 6

- Dr. Clara L. Hedegaard (School of Engineering and Materials Science, Queen Mary University of London), collaborated in the experimental work and discussions.

Published Work

Most of the work presented in this thesis has been published in peer-reviewed journals. This is the list of papers:

- Chapter 2

  Quetzeri-Santiago, M. A., Castrejón-Pita, J. R., & Castrejón-Pita, A. A. (2020). On the analysis of the contact angle for impacting droplets using a polynomial fitting approach. *Experiments in Fluids* **in press**.

- Chapter 4

  Quetzeri-Santiago, M. A., Yokoi, K., Castrejón-Pita, A. A., & Castrejón-Pita, J. R. (2019). Role of the Dynamic Contact Angle on Splashing. *Physical Review Letters*, 122(22), 228001.

  Quetzeri-Santiago, M. A., Castrejón-Pita, A. A., & Castrejón-Pita, J. R. (2019). The Effect of Surface Roughness on the Contact Line and Splashing Dynamics of Impacting Droplets. *Scientific reports*, 9(1), 1-10.

- Chapter 5

  Zhang, G., **Quetzeri-Santiago, M. A.**, Stone, C. A., Botto, L., & Castrejón-Pita, J. R. (2018). Droplet impact dynamics on textiles. *Soft matter*, 14(40), 8182-8190.

- Chapter 6

  Quetzeri-Santiago, M. A., Hedegaard, C. L., & Castrejón-Pita, J. R. (2019). Additive Manufacturing with Liquid Latex and Recycled End-of-Life Rubber. *3D Printing and Additive Manufacturing*, 6(3), 149-157.

Abstract

Understanding the contact line dynamics during droplet impact is critically important for industrial processes such as coating, the spraying of pesticides and for the design of anti-icing surfaces or impermeable clothing. It is known that, upon impacting on a solid, a droplet can spread, bounce off the substrate or splash depending on the liquid characteristics, the solid properties, the impact speed and the ambient pressure. In this thesis, we explore droplet impact in terms of some of these variables. Consequently, this work is focused on the experimental study of the contact line dynamics of impacting droplets on substrates ranging from wettable to non-wettable and from porous to non-porous. In particular, we focus on the parameters affecting: i) the splashing threshold of impacting droplets on solid substrates and ii) the penetration of impacting droplets through textiles. Furthermore, we apply our findings to the development of a liquid latex droplet-on-demand printing system.

Most of the experiments in this thesis consist of the visualisation, by high speed imaging, of the impact of ethanol, water and aqueous glycerol droplets on solid and textile substrates. In addition, we present a custom-made Matlab algorithm that uses a polynomial fitting approach to extract the dynamic contact angle as a function of the contact line velocity. Moreover, we analyse the effect of droplet shape, the order of the fitting polynomial and the fitting domain, on the measurement of the contact angle on various stages following droplet impact.

We use our experimental setup to demonstrate the importance of wettability and substrate roughness on the contact line dynamics and the impacting outcome. For smooth surfaces, we show that the maximum advancing contact angle (θ_{max}) is greater than 87 degrees for all the liquid/substrates. Moreover, we show that splashing depends on the substrate wettability and its threshold can be parameterised by θ_{max} and the splashing ratio. Correspondingly, for rough surfaces, we determine that θ_{max} increases with increasing substrate roughness. Furthermore, we establish that the ratio of the peak to peak roughness to the surface feature mean width, in conjunction with θ_{max} and the splashing ratio, adequately predict the splashing threshold.

Similarly, for the droplet impact dynamics on textiles, we find that the textile characteristics, such as the pore size and solid fraction, are critical for the impact outcome. Correspondingly, we find three different impact regimes, namely, 'no penetration', 'capture' and 'complete penetration'. Additionally, by balancing the kinematic pressure with the capillary pressure, we find a critical pore size for the transition from capture to complete droplet penetration in terms of the Weber number.

Finally, we present a setup that permits the printing, by droplet impact, of liquid latex on paper with a high solid content (60 wt %). The process is controllable and reliable, making the printing of patterns possible. With this setup, multilayer objects were created from pure liquid latex, as well as from micronized rubber powder and latex suspensions. These results demonstrate the potential of droplet-based additive manufacturing processes to produce prints of liquid latex and tire rubber reuse.

Contents

List of Figures

List of Tables

Symbols

α	Wedge angle
β	Splashing ratio
Γ	Solid fraction
Δ	Average distance between the adsorption/desorption location on the solid surface
δ_n	Number of pixels fitted to the droplet profile by the Matlab algorithm presented in this thesis
η	Slip velocity
θ_a	Advancing contact angle
θ_{CB}	Cassie-Baxter angle
θ_D	Dynamic contact angle
θ_{DR}	Dynamic receding contact angle
θ_{DA}	Dynamic advancing contact angle
θ_{max}	Asymptotic dynamic advancing contact angle
θ_r	Receding contact angle
θ_s	Static contact angle
θ_W	Wenzel angle
θ_y	Young's angle
κ^0	Equilibrium frequency of molecular displacements
Λ	Slip length
λ	Displacement in pixels added to the true substrate position
λ_0	Wavelength
λ_c	Capillary length
λ_g	Mean free path of the gas molecules
μ	Liquid viscosity
μ_g	Gas viscosity
ρ	Liquid density
ρ_g	Gas density
σ	Surface tension
Φ	Camera inclination angle
ϕ	Substrate inclination angle
χ	$\pm$ 1 depending on if the contact line advances or recedes
ψ	Interface profile
Ω	Droplet volume
ω	Substrate inclination step rate
D_0	Initial droplet diameter
$D(t)$	Contact diameter dependent on time
$d(t) = D(t)/D_0$	Spread factor

D_a	Advancing contact diameter
D_{eq}	Equilibrium contact diameter
D_{max}	Maximum contact diameter
$d_m = D_{max}/D_0$	Maximum spread factor
d_{mesh}	Textile pore size
D_r	Receding contact diameter
E	Energy
f	Liquid-solid contact area
g	Acceleration due to gravity
H_t	Height of the lamella
k_b	Boltzmann constant
k_l	Constant
k_μ	Constant
L	Pillar height of a micro-structured substrate
P_D	Capillary Pressure
Q	Flow rate
R	Needle radius
r	Average roughness ratio
R_a	Average roughness
R_{pk}	Average peak to peak feature size
R_{rsm}	Root mean square roughness
R_{sm}	Surface feature mean width
R_{yarn}	Yarn size
s	Contact line position from the contact point
T	Temperature
t	time
$t^* = D_0/U_0$	Inertial time
t_e	Ejection time of the lamella
$t_{capillary} = \frac{\rho}{d_{mesh}^3}\frac{U_0}{D_0}$	Capillary time
U_0	Droplet impact velocity
U^*	Critical impact velocity for the transition from Cassie-Baxter to Wenzel state in micro-structured substrates
U_{sp}	Critical impact velocity for splashing
u_{cl}	Contact line velocity
V_t	Velocity of the lamella
w	Interpillar distance of a micro-structured substrate
$Ca = \frac{\mu U_0}{\sigma}$	Capillary number
$K = We^{1/2}Re^{1/4}$	Splashing parameter
$Oh = \sqrt{We}/Re$	Ohnesorge number
$Re = \frac{\rho D_0 U_0}{\mu}$	Reynolds number
$We = \frac{\rho D_0 U_0^2}{\sigma}$	Weber number

Chapter 1

Literature Review

This chapter provides the motivation behind the projects presented herein. Furthermore, it presents the overall thesis structure and provides a brief literature review on the wettability and droplet impact phenomena.

1.1 Introduction

Industrial systems such as coating, sprays, inkjet and 3D printing, and other natural phenomena like rain impacting on tree leaves or soil are processes where droplet dynamics play a major role. Therefore, the study of fluid dynamics can help us to optimise industrial processes and understand nature. A. M. Worthington is known to be one of the first researchers to study droplet dynamics in detail. In 1895, he studied the impact of liquid droplets onto solid dry substrates [1]. From this preliminary study, several researchers have continued to elucidate the physics behind droplet dynamics. Past works have revealed that drop impacting on a solid dry substrate can deposit, bounce or break into secondary droplets (splash) [2]. The result depends not only on the droplet properties and impact speed, but on a wide range of parameters including the atmospheric pressure and the surface properties such as roughness, temperature and stiffness [3, 4]. In this thesis, we focus mainly on the influence of the substrate wettability, roughness and porosity on the droplet impact dynamics. We also present a novel methodology to measure and analyse the contact line dynamics. Furthermore, we present a droplet-on-demand system that can successfully print liquid latex.

The thesis structure is as follows: In this chapter (Chapter 1) a brief literature review is presented; Chapter 2 shows the overall experimental methodology used throughout the thesis; chapters 3-5 include a study on droplet impact dynamics on dry solid substrates, from spreading (Chapter 3) to splashing (Chapter 4), and on textiles (chapter 5). Chapter 6 introduces a droplet-on demand latex 3D printer. Finally, Chapter 7 presents the summary of my results and discusses possible improvements and future work.

1.2 Contact angle

This section presents the key concepts that describe the shape taken by a droplet once it *sticks* to a dry solid substrate; also known as wettability. In other words, we focus on the study of wetting; the phenomena of a liquid contacting or moving

over a solid substrate. The wettability of a liquid on a solid substrate is critically important for situations where either liquid adhesion or repellency are required. Industrial processes such as coating and the spraying of pesticides are examples where maximising the liquid adherence to a solid is desired [5, 6]. In contrast, repellency is sought in the design of materials with anti-icing properties or impermeable clothing. Drop wettability is known to depend on the properties of both, the liquid and the solid substrate, and is commonly studied through the apparent contact angle. The contact angle is defined as the angle between the tangent of the droplet surface and the tangent to the solid surface at the contact line, i.e. the angle formed by the intersection of the liquid-solid interface and the liquid-vapour interface, as shown in Fig. 1.1 [7, 8]. According to the convention, a contact angle less than 90 degrees the surface is regarded as hydrophilic or wetting, in contrast, an angle greater than 90 degrees is regarded as hydrophobic or non-wetting. Experimental and theoretical efforts have been made to understand the contact angles of a droplet in motion, and the effects of surface wettability on droplet impact. However, it is generally accepted that this phenomena is yet not fully understood.

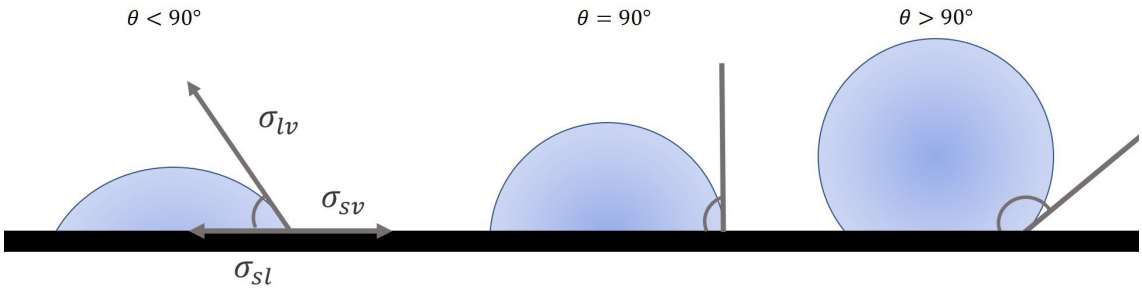

Figure 1.1: Diagram showing the contact angle of a droplet sitting on a solid surface. The figure shows examples of the different attainable values of the contact angle on a solid surface.

In most wetting phenomena, surface tension (σ) is the force that governs the equilibrium state. Surface tension acts as a force per unit length or energy per unit area and can be described with classical mechanics and thermodynamic arguments. From the mechanical point of view, surface tension arises as a competition of cohesive forces at the bulk of the liquid and cohesive forces at its interface with another material. From thermodynamics aspects, the surface tension can be defined as an increase of free energy E by an increase unit of surface area [9],

$$\frac{\partial E}{\partial A}. \tag{1.1}$$

In this thesis we adhere to this thermodynamic definition as it represents the ratio between different interface tensions such as liquid-gas, solid-liquid and solid-gas.

In the cases where a solid, a liquid droplet, and a gas are all in contact, three surface forces arise: the solid-liquid σ_{sl}, solid-gas σ_{sv} and liquid-gas σ_{lv}. The interface where solid, liquid and solid coexist is called the contact line. A droplet contacting a surface spreads and eventually tends to adopt a semi-spherical shape to reach a minimum energy state and equilibrium [9, 10]. This equilibrium state between the liquid droplet, the solid and the gas can be derived by considering a moving contact line over a distance dx. For a droplet on an ideal surface; smooth, homogeneous, rigid and insoluble the work per unit length done by the contact line is [11],

$$\delta W = (\sigma_{sl} - \sigma_{sv})dx + \sigma_{lv}cos(\theta_Y)dx. \tag{1.2}$$

If the droplet is at equilibrium, then the work done is zero and

$$\sigma_{sv} = \sigma_{sl} + \sigma_{lv}cos(\theta_Y), \tag{1.3}$$

where θ_Y is the Young's contact angle [12]. Equation 1.3, is known as Young's equation and represents the balance of the surface tension forces between solid, liquid and gas. Accordingly, Young's contact angle can be used to predict the equilibrium diameter of a droplet resting on a solid surface (D_{eq}) as

$$D_{eq} = D_0\, sin(\theta_Y) \left[\frac{4}{(1 - cos(\theta_Y))^2(2 + cos(\theta))}\right]^{1/3}, \tag{1.4}$$

where D_0 is the diameter of the original droplet (before contacting the surface), [11]. This way, if $\theta_Y \to 0$ then $D_{eq} \to \infty$ and the liquid tends to wet the surface completely. In contrast, if $\theta_Y \to 180^\circ$ then $D_{eq} \to 0$ and the droplet barely touches the surface. By convention, hydrophobic surfaces are defined as surfaces that form a contact angle $\theta_Y > 90^\circ$ and hydrophilic surfaces are the ones that have a contact angle of $\theta_Y < 90^\circ$. Equations 1.3 and 1.4 are only satisfied if the thermodynamic

equilibrium is reached, and an unique contact angle and equilibrium radius are obtained irrespective of how the droplet was deposited on the substrate [11]. However, in practice, the contact angle given by equation 1.3 cannot be measured, because even a small heterogeneity on the substrate can lead to thermodynamic meta-stable states affecting the contact angle [13]. In fact, it has been found that every surface has as least two asymptotic possible values of the contact angles, the advancing and receding angles (θ_a and θ_r respectively) [5]. The former is the contact angle measured during droplet spreading, and the latter is the contact angle measured as the droplet recedes after spreading [5]. Accordingly, assuming that the drop shape can be approximated as a truncated spherical cap, an advancing (D_a) and receding (D_r) diameter can be defined

$$\frac{D_i}{D_0} = 2\left[\frac{sin^3\theta_i}{2(1-cos(\theta_i)(2-cos\theta_i-cos^2\theta_i)}\right]^{1/3}, \tag{1.5}$$

where the subscript i refers to the advancing D_a and θ_a or receding case D_r and θ_r. The difference between the maximum θ_a and the minimum θ_r is known as contact angle hysteresis [12]. In fact, the contact line of drops resting on an inclined plane without slipping takes a range of contact angles along its length due to the contact angle hysteresis [11].

So far, we have referred to the contact angle in quasi-static conditions, i.e. the drop shape approximates to a spherical cap, but in practice there are many situations where the contact line is moving and the spherical cap approximation is no longer valid. In these cases a dynamic expression of the advancing and receding contact angles has to be defined to accurately model the wetting phenomena. The dynamic advancing and receding angles are found far from equilibrium with a contact line in motion [5]. The dynamic angles change with time and the contact line velocity [14]. Accordingly, is possible to define a *static* hysteresis and a *dynamic* hysteresis. Static contact angle hysteresis arises from a difference between the advancing and receding angles at zero contact line speed. The dynamic contact angle hysteresis is observable for moving contact lines and is caused by forces between the droplet and the surface - preventing the droplet from flowing freely. At high contact line

velocities, the dynamic hysteresis dominates the motion over the static hysteresis, whereas in slow drop motion (in a rough surface) the static hysteresis dominates [7]. The moving contact line problem is described in greater detail in subsection 1.2.2.

Many authors attribute the contact angle hysteresis to surface roughness, however, C. W. Extrand and Y. Kumagai found that roughness effects are smaller for static droplets than for moving droplets [15]. Other possible sources of hysteresis are surface heterogeneity, adsorption/desorption and deformation of the surface, nevertheless, the fundamental causes are not really understood [7, 13]. The mechanisms from which the contact angle hysteresis arises are not clear and consequently more theoretical and experimental work is needed to clarify the phenomena.

Substrate roughness affects wettability, and to quantify the effect of the substrate roughness on the contact angle, the Wenzel and the Cassie-Baxter models are widely used. In the former, Young's contact angle model (equation 1.3) is adjusted by the average roughness ratio r, defined as the factor by which roughness increases the solid-liquid interfacial area [16]. This is,

$$cos(\theta_W) = rcos(\theta_Y), \tag{1.6}$$

where θ_W is the Wenzel angle. In Eq. 1.6, $r = 1$ for smooth surfaces while $r > 1$, for rough ones. In the Wenzel state the droplet is placed between the grooves of the substrate, i.e. the droplet wets a larger area than if the substrate was completely smooth. The main conclusion of this model is that the rougher the surface the lower the contact angle. In contrast, the Cassie-Baxter model assumes the droplet is on top of the substrate asperities and the contact with the solid surface is minimised. The Cassie-Baxter model is expressed as follows [17],

$$cos(\theta_{CB}) = f(1 + cos(\theta)) - 1, \tag{1.7}$$

where f is the liquid-solid contact area. Examples of the Cassie-Baxter and Wenzel states are shown in Fig. 1.2. In the Cassie-Baxter state, high droplet mobility and contact angles larger than 90 degrees have been observed [18]. Recently, it has

been reported that, for substrates with different roughness scales, a mix between the Cassie-Baxter and Wenzel states can be achieved [18]. For example, a droplet can be in a Wenzel state at the nanometric roughness while staying in a Cassie-Baxter state at the micrometric scale and vice versa [18]. Understanding Wenzel and Cassie-Baxter states are key to many applications since it has been widely reported that droplets on the Cassie-Baxter state have a larger contact angle and have higher mobility than in the Wenzel state [19, 20]. Moreover it has been observed that a transition between the Cassie-Baxter state is possible. Patankar et. al. showed that if a drop in a Cassie-Baxter state is pressed against the substrate, the droplet transitions to a Wenzel state [20]. The transition happens when the air pockets on the substrate collapse and the liquid droplet touches the bottom of the substrate. This transition has also been studied at impacting conditions on microstructured substrates and it occurs above a threshold impact velocity [21, 22]. The threshold velocity has been shown to depend greatly on the surface morphology as well as the roughness scale [21, 22]. The Cassie Baxter to Wenzel transition is explored in greater detail in subsection 2.6.

In this subsection we have considered the wettability of a static droplet in contact of smooth and solid surfaces and how can be described with the Young's, Wenzel and Cassie-Baxter models. Assessing the wettability of a solid surface from the theoretical perspective is often challenging, in contrast, the experimental study of the contact angle is often more effective. In the next subsection we present some of the current experimental techniques used to measure the contact angle of droplets on solid substrates.

1.2.1 Experimental methods for measuring the contact angle

As described in the last section, the contact angle is an useful widely-used parameter for describing the wettability of a liquid on a solid. Therefore, several experimental techniques have been developed for measuring the contact angle. Most of these techniques rely on optic methods to detect the contact line and the droplet profile. The contact angle is normally obtained by doing a profile fitting to the droplet

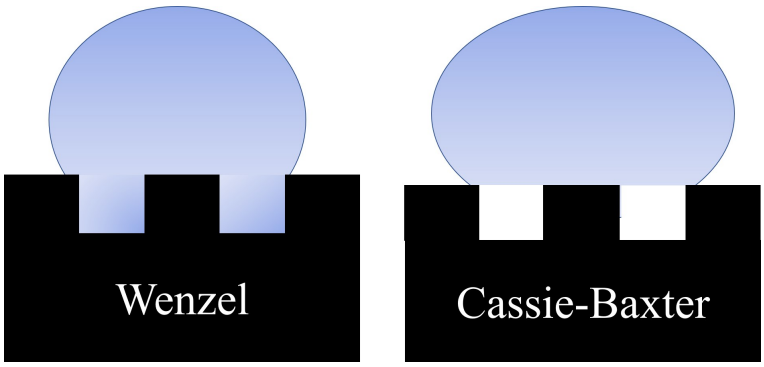

Figure 1.2: Wenzel and Cassie-Baxter states of a droplet standing on a structured surface. In the Wenzel state the droplet rests on the asperities. In the Cassie-Baxter state the droplet rests on top of the pillars.

boundary and calculating the tangent to the fitted boundary. It should be noted, that the angle obtained by all experimental methods is an *apparent* contact angle, i.e., is not the angle described in Eq. 1.3. In this section we review three of the most common methods to measure the contact angle, namely, the *sessile drop*, the *tilted plane* and the *Wilhelmy methods*.

The sessile drop method consists of pumping liquid into and out a droplet resting on a substrate- measuring the advancing and receding angles respectively [7]. The tilted plane method consists of placing a droplet on a tilting a plane. The droplet stays pinned to the tilted plane due to a difference in curvature between the leading and the trailing edges. This difference of curvature generates a pressure gradient inside the drop, that opposes the force of gravity. In this method, the advancing and receding contact angles are measured as soon as the droplet slides down [7]. Finally, the Wilhelmy method consists of driving in and out a solid body with a flat geometry from a liquid pool. In this method, the contact angle is determined at the solid-liquid interface [10]. Diagrams of the three methods are shown in Figs. 1.3 and 1.4.

In the Wilhelmy approach, the only required measurable quantities are the perimeter of the contact line and the weight of the plate, which can both be measured precisely with simple methods [10]. The disadvantage of this approach is that the liquid wets all the surface of the plate, so the plate requires a uniform topography, so it is not useful for anisotropic materials [7, 10]. The other problem is that border effects can affect the measurement [7, 10].

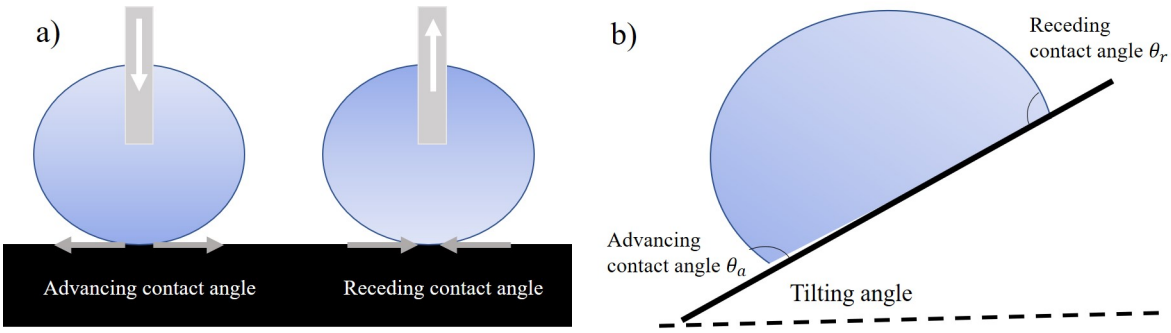

Figure 1.3: Schematic Diagram of: a) the sessile drop method; the droplet is pushed with a syringe and advances to measure the advancing contact angle or is sucked back and recedes to measure the receding contact angle. b) The tilted plate method, where a droplet rests on an inclined plane and the droplet is deformed due to gravity. This deformation leads to the possibility of measuring both, the advancing and receding angles.

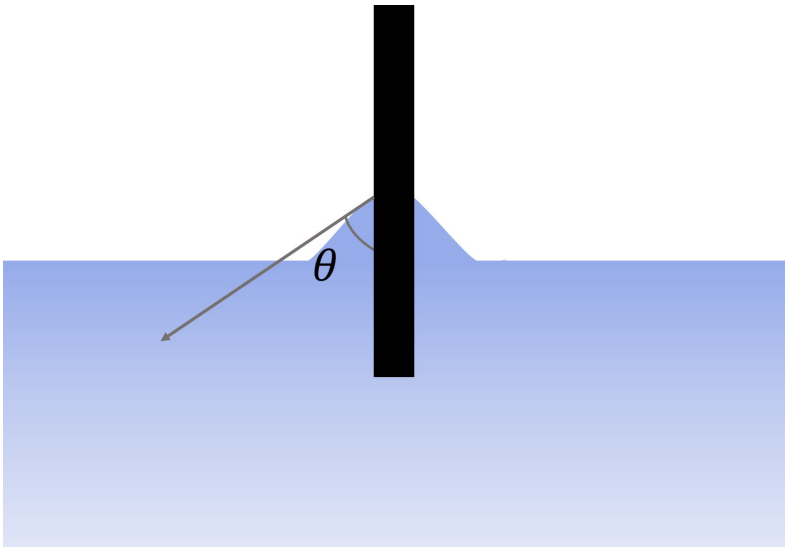

Figure 1.4: Diagram showing the Wilhelmy method. This method consists on plunging a solid into a liquid bath. Measuring the advancing contact angle while the solid is getting pushed into the liquid. Conversely, the receding angle is measured while taking the solid away from the liquid bath.

The tilted plate method setup is easy to construct as only a camera and an inclined substrate are required. Most of the work is done by image analysis. There is however a disadvantage of this method; it has been found that the droplet size and shape can affect the minimum angle for which the droplet slides [23]. Therefore, a small surface heterogeneity altering the drop shape could lead to errors on the contact angle measurements.

The sessile method requires the surface, a camera, a needle and a pump that can push in or out liquid from the droplet. The advantage of this method is that it also uses conventional optical imaging and the contact angle can be obtained directly.

The disadvantages are that is droplet-size-dependent and droplet shapes can distort the wettability at the feeding needle, changing the contact angle reading [7, 12]. Another problem arises for large ($\approx$ 180 degrees) or small ($\approx$ 0 degrees) contact angles [12].

A major complication of all these methods is that they strongly depend on the image analysis used to identify the liquid-vapour interface profile. The effect is further complicated by droplet curvature changes while in motion [7]. However, there have been different approaches to overcome this difficulty. One of the most common imaging analysis techniques is the axisymmetric drop shape analysis profile where the contact angle is measured by fitting a Laplace equation to the surface droplet profile. The angle between the slope of the theoretical profile at the contact point is then defined as the contact angle [24]. The drop needs to be perfectly axisymmetric to fit the theoretical curve to the drop profile [25]. To avoid the axisymmetric requirement, attempts have been made to calculate the contact angle using ellipsoidal approximation to the droplet profile [26]. Both methods show good agreement with the theory at static conditions, but are not suitable for conditions where a droplet is largely deformed. To overcome this issue the goniometric mask method has been used [27, 28]. In this method, a goniometer is digitally used around the edge of the droplet profile [29]. This method shows better results when compared to the axisymmetric shape analysis at static conditions and can track the evolution of the contact angle during droplet spreading. Another method that has shown good results, in static conditions, is the polynomial fitting approach. This method consist of extracting the droplet profile and fitting it with a polynomial function around the contact point. Previous research has focused on the effect of the number of pixels and the order of the polynomial on the contact angle measurement [25, 30]. In Chapter 2, we show a similar methodology to track the evolution of the dynamic contact angle of a spreading drop after impact. Moreover, in that section, we use various polynomial fittings to measure the *dynamic* contact angle and discuss their differences with other approaches. Additionally, we analyse the effect of an inadequate detection of the contact line (pinning points) on the measurement of the contact angle. The

dynamic contact angle is of critical importance for contact lines moving at large speeds, as shown in the next section.

1.2.2 Moving contact lines

The physics of droplets interacting with solid substrates is dominated by the wetting of the contact line. In this section, we discuss the problem of the moving contact line, i.e. the advancing or receding of the contact line over a solid substrate [5]. In this case, inertial, viscous and surface tension forces act on the fluid [31]. In fact the contact line movement can be described by a corner flow [32], where the viscous stress can be approximated as $\mu\, u_{cl}/s$ (where μ is the liquid viscosity, u_{cl} is the contact line velocity and s is the contact line position from the impact point), and diverges close to the contact line [31]. These dynamics may cause a strong curvature in the liquid interface near the contact line [33]. Therefore, Young's contact angle model ceases to be valid and a *dynamic* contact angle θ_D needs to be defined. The force experienced by an advancing liquid towards the dry region can be expressed as:

$$F(\theta_D) = \sigma_{sv} - \sigma_{sl} - \sigma_{lv} cos(\theta_D). \tag{1.8}$$

This force tends to zero as θ_D tends to θ_Y, and its magnitude depends on the fluid properties, the contact line velocity, and is quantified by the capillary number $Ca = (\mu\, u_{cl})/\sigma_{lv}$, [33] [34]. As noted by Huh and Scriven the system does not have an intrinsic scale [32]. However, for distances smaller than the capillary length ($\lambda_c = \sqrt{\sigma_{lv}/\rho g}$ where ρ is the density of the liquid and g is the gravity) the lubrication approximation can be used to describe the interface profile $\psi(x)$ this is [31]:

$$\frac{d^3\psi}{dx^3} = -\frac{3\chi\, Ca}{h^2}, \tag{1.9}$$

where χ is +1 or -1 for advancing or receding contact lines respectively.

In asymptotic cases this equation reduces to $\psi'(x) \approx \theta(x) \approx [9\, Ca\, ln(x/c)]^{1/3}$ [35]. If the motion of the contact line is dominated by viscous dissipation and the

fluid is divided into an outer section that do not slip on the substrate, and an inner region where the fluid can slip, one can write [31],

$$\theta_D^3 = \theta_Y^3 + 9\chi\, Ca\, ln\,(\frac{C_0\, l_0}{l_i}), \tag{1.10}$$

which is commonly referred to as the Cox-Voinov law. Here l_0 and l_i are the macroscopic and the molecular lengths respective and solve the singularity problem at the contact line and C_0 is a constant to take into account the system specific parameters.

Equations resulting from hydrodynamic theories are highly nonlinear and experimental methods are unable to reach molecular scale measurements. Therefore, numerical simulation are often used to gain some understanding on the moving contact line phenomena. There are two main approaches on numerical analysis. The first uses a continuum approach (volume of fluid simulations) and the second approach simulates each particle within the fluid (molecular dynamics simulations) [12]. Continuum simulations present major limitations at the contact line as the no-slip boundary condition leads to divergences in pressure and energy [36]. In contrast, molecular dynamics simulations are naturally consistent with the no slip boundary condition. A technique to circumvent the divergences around the contact line is to allow the fluid to slip within a fixed length. The Navier-slip is the most commonly applied model to enforce this condition [37]. Within this model, the shear stress governs the magnitude of the slip and can be expressed as,

$$\nu - u_{cl} = \Lambda \frac{\partial(\nu)}{\partial x}, \tag{1.11}$$

where ν is the slip velocity and Λ is the slip length; this equation is evaluated at the solid boundary ($x = 0$). The slip length is the region where the fluid can flow freely without the restriction of the no-slip boundary condition. The slip length has been proved to exist at the molecular level, which is normally too small to be resolved by numerical simulations [33]. Moreover, implementing this slip depends on the interface tracking of the droplet [38]. Methods that explicitly track the interface normally require a slip condition placed at the mesh node at the contact line [39]. VOF implementations include an effective slip length [40], because the interface is

advected not from the solid boundary, but from a distance from the solid boundary, where the no-slip boundary conditions does not apply [38]. This generates a problem because a smaller mesh gives a smaller effective slip and viceversa, therefore VOF is mesh dependant. S. Afkhami et al. showed in 2009 that a scaling for θ_D based on Eq. 1.10, the mesh size and the capillary number the dependence on the mesh spacing is removed and the solutions converge [33].

In 2009 K. Yokoi, et al. used a level set method coupled with a VOF function to track the contact line interface. The no-slip condition can be satisfied by extrapolating the fluid velocity into the solid and by using bilinear interpolation by a level set function [41]. This way, the no-slip condition is satisfied with no singularities. Furthermore, this method includes the effects of the contact angle dynamics in the spreading phenomena. These simulations were run with different contact angle models: dynamic, equilibrium and static contact angles, and the results were compared with experiments carried out by D. Vadillo et. al. [42]. The dynamic contact angle model produced the best agreement with experiments, with the simulation correctly predicting that the advancing (receding) contact angle tends to a limit as the velocity of the contact line increases (decreases). Moreover, it was shown that the contact angle has a maximum value while spreading and acquires different values at $u_{cl} = 0$ m/s (this can be understood as the contact angle hysteresis).

Other techniques used in the continuum approach include van der Waals interactions between the solid surface and the liquid and a diffuse interface. The diffuse interface is implemented by considering diffusion in the transition layers found between two different fluids, producing a continuous density gradient [43].

On the other hand, molecular dynamic simulations are automatically consistent with the no-slip boundary [44]. In these simulations, the motion of every particle in the solid and the fluid is taken into account, and the macroscopic behaviour can be obtained by averaging the momentum energy and exchange of these particle collisions [43]. This idea is based on the kinetic theory of gases, and is modelled by the Boltzmann transport equation [36]. Nowadays, the most used method of molecular dynamics is called Lattice Boltzmann, in which the motion of the contact

line is determined by molecules located at the triple line. In this model, the driving force per unit length of the contact line is given as:

$$F_w = \sigma_{lv}(cos(\theta) - cos(\theta_D)), \tag{1.12}$$

where θ_D is the dynamic contact angle and the wetting velocity is given by,

$$U(\theta) = 2\kappa^0 \Delta sinh\left[\sigma_{lv}(cos(\theta) - cos(\theta_D))\frac{\Delta^2}{2k_bT}\right], \tag{1.13}$$

where k_b is the Boltzmann constant, T the temperature, κ^0 the equilibrium frequency of molecular displacements occurring within the triple line and Δ is the average distance between the adsorption/desorption locations on the solid surface [7].

This section has reviewed some of the problems found on the study of the contact line motion and revised some models and numerical simulations to describe the contact line dynamics. The next section approaches the specific problem of liquid deformation and contact line motion, i.e. droplet impact on a dry solid surface.

1.3 Droplet impact on dry substrates: Contact line dynamics and splashing

Droplet impact phenomena on dry solid substrates have been widely studied since the work of Worthington in 1895, [1]. These phenomena is important in industrial processes such as coating, inkjet printing and combustion as well as in natural processes such as rain impacting on tree leaves or soil erosion. Rioboo et. al. in 2001 found that there are at least five different outcomes from a droplet impacting a solid surface, namely, deposition, partial and total rebound, receding breakup and splashing [2]. During droplet impact on a solid substrate, the inertial energy is transformed into surface energy [45]. However, there is also energy dissipation coming from the liquid viscosity and the no-slip boundary condition. This creates a thin boundary layer that arrests the fluid [45] and the impact is therefore governed by inertia, viscous and surface forces. Consequently, the drop impact dynamics are often

characterised by dimensionless numbers that take into account these parameters. The Weber number $We = \frac{\rho U_0^2 D_0}{\sigma}$, is the ratio of inertia and surface energy forces, and the Reynolds number $Re = \frac{\rho U D_0}{\mu}$ relates inertia with the viscous dissipation, here ρ, σ and μ are the liquid density, surface tension, and viscosity respectively, D_0 is the drop diameter and U_0 is the impact velocity. In this thesis, we focus on *large* Weber and Reynolds numbers, meaning that gravity effects can be neglected, the droplet greatly exceeds D_{eq} (as defined in Eq. 1.4) while spreading, and viscous effects are important just near the contact line [5].

This section is divided into 5 parts. Subsection 2.2 introduces the concept of smooth deposition and rebound and the definition the spreading factor. Section 2.3 introduces the concept of fingering and its causes. Section 2.4 focuses on the causes leading to the breakup into secondary droplets of an impacting droplet, i.e, splashing. Finally, section 2.5 reviews droplet impact on porous and microstructured substrates.

1.3.1 Spread factor on flat solid surfaces

The spreading (moving) front of a droplet impacting a solid substrate approaches a contact angle of 180 degrees at the first instant after impact. Immediately after this first contact, the droplet undergoes large deformations around the contact line, while the rest of the droplet remains in a spherical shape. As a result of this large deformation an air bubble is often entrapped inside the droplet at the centre of impact; although this bubble has not been observed to influence the subsequent dynamics [46, 47]. During this first stage of impact, the vertical momentum of the droplet is transformed into horizontal momentum which results from a strong pressure at the contact line. This pressure decays rapidly and, after a time $t* = D_0/2U_0$ (inertial time), the vertical motion of the droplet stops, and the droplet deformation can be described by a hyperbolic flow bounded by a viscous boundary layer growing as $\sqrt{\mu/\rho t}$, [45].

In particular, for an impacting droplet on a solid surface, the contact diameter $D(t)$ is characterised by a $t^{1/2}$ growth until it reaches a maximum contact diameter

D_{max} [48]. In this initial stage, droplets can slowly recede to acquire a smaller equilibrium contact diameter D_{eq}. Under some conditions, a second spreading/receding phase is observed that ends with the drop oscillating around the equilibrium contact diameter [2, 49]. The first spreading stage is commonly characterised in terms of the spread factor $d(t) = \frac{D(t)}{D_0}$, or the *maximum* spread factor $d_m = \frac{D_{max}}{D_0}$, where D_0 is the diameter of the drop prior impact. The maximum spreading factor typically ranges from 1.25 to 5 [48, 50]. For a droplet that does not recede, d_m, can be predicted by a lubrication approximation and energy balance methods. In contrast, if the droplet recedes over the surface these approximations are no longer valid and a free rim surrounding the lamella governs the droplet dynamics [45]. Other models are based on a mass and momentum balance and use a thin film approximation for the spreading dynamics.

Using scaling arguments, Clanet et al. in 2004 found that d_m is a function of $We^{1/4}$ for both hydrophobic and hydrophilic surface [51]. This scaling was subsequently validated by experimental data for drops impacting in the range of $2 \leq We \leq 900$. However, this scaling was proved to be valid just in a set of particular conditions [52]. Additionally, other different regimes dominated by viscous and capillary forces have been found by Eggers et al. in 2010 and Lagubeau et al. in 2012 [45, 53]. In this case $d_m \approx Re^{1/5}$. In contrast, at high We numbers viscosity can be neglected and $d_m \approx We^{1/2}$ [45, 53]. In a different work, for the viscous regime, Lee et al. in 2016 proposed a scaling of d_m in terms of $Re^{1/5}$ and θ_D at d_m for low impact velocities [27, 28]. The study concludes that θ_D parametrises the liquid characteristics and substrate roughness. Further studies by Laan, et al. in 2014, used a Padé first approximation to conclude that $d_m \propto Re^{1/5} f(WeRe^{-2/5})$, validating previous works that argued that both viscous and capillary forces are needed for an accurate description of the dynamics [45, 52].

Numerous experiments have been conducted to validate scaling theories and study the influence of the parameters governing the spreading of a droplet upon impact. Experiments conducted by Visser, et al., on micrometer sized droplets, explored the droplet size dependence on d_m. The study concluded that d_m depends

on the We and Re numbers and not on D_0 [54]. However, experimental studies by Vsikalo, et. al., suggest that viscosity effects are more important for smaller droplets and d_m tends to be smaller. Other studies have shown that the role of wettability of the substrate on spreading is not clear [50]. Most of the scientific community agrees that wettability influences the receding process of the droplet but there is no agreement as to whether it influences its spreading. Experimental data from Bayer and Megaridis suggest that there is no relationship between the contact angle and the contact line speed [49]. In contrast, some studies of droplet impacting on stainless steel, glass and paraffin substrates, argue that wettability influences d_m under a critical Weber number [9, 55, 14, 42]. Moreover, experimental data have shown that for $We < 200$, d_m is a monotonically decreasing function of θ, while for $We > 200$ $d_m \approx We^{1/5}$ [56]. Simulations based on the finite element method, implementing a changing contact angle between θ_a and θ_r during droplet spreading and receding, showed agreement with experiments [57]. Volume of fluid simulations with constant and variable angles have been implemented, where a variable angle showed a better matching to experimental results. Experimental studies and numerical simulations have concluded that the dynamic contact angle is largely influenced by the wettability of the substrate, and the viscosity of the fluid [14, 41]. These simulations can predict $d(t)$, by adjusting the numerical simulation using experimental data for the dynamic contact angle. These simulations were run with different contact angle models: dynamic, equilibrium and static contact angles. The model which produced the best agreement with experiments was the dynamic contact angle model. Another important result is that, for hydrophobic surfaces, the dynamic advancing (receding) reaches a maximum (minimum) asymptotic value.

It also should be noted that, despite having different approaches and scaling arguments, all of the previous models fit well with experimental data. This is because the value of d_m varies less than an order of magnitude, making power laws difficult to identify [47]. In fact, increasing the Weber and Reynolds numbers lead to instabilities and splashing, altering the spreading mechanisms, making asymptotic testing impossible [47]. As we already mentioned, increasing the impact velocity

lead to instabilities during the spreading. In the next subsection, we discuss one of these instabilities known as *fingering*.

1.3.2 Fingering

Fingering refers to a phenomena where, after an impact on a dry substrate, the spreading lamella *separates* at the spreading edge to form jet structures that resemble fingers [5]. Fingering studies are useful to forensic sciences as its splatter pattern can provide information about the drop size and trajectory [58, 59]. Fingering is attributed to a Rayleigh-Taylor type instability on the lamella edge [60, 61]. Linear stability analysis of a liquid rim further supports this theory. During droplet impact on a solid surface, the lamella decelerates by friction forces from the solid surface which in turn causes a perturbation [5]. The perturbation travels with a wavelength $\lambda_0 = 2\pi(3\sigma/\rho a)^{1/2}$, where a is the deceleration of the droplet normal to the wall. Based on λ_0, the number of fingers can be determined as $N_f = \pi D_{max}/\lambda_0$ [5]. However, Rayleigh-Taylor instability models are unable to predict the merging and splitting of the fingers as observed in the experiments [61]. In addition, fingering is suppressed by reducing the ambient pressure [62]. Furthermore, at a critical impact velocity, fingers can break into droplets; this phenomenon is called splashing and is the subject of study the upcoming subsection.

1.3.3 Splashing of droplets on smooth substrates

An impacting droplet reaching sufficiently high We and Re numbers will break up into secondary droplets, these phenomena is known as splashing [5, 47]. Splashing occurs when the contact line speed exceeds certain velocity, air is entrained and there is a dynamical wetting transition. Splashing is generally divided into two different phenomena called corona and prompt splashing [47]. Corona splashing refers to the phenomena where a thin sheet of liquid is ejected upwards and outwards from the droplet and the liquid sheet breaks up into small droplets. Prompt splashing refers to the phenomena where small drops detach from the fingers created at the outer rim of the spreading droplet. There is no formal definition of corona and

prompt splashing apart from the one based on the observable shape and timing of splashing. As observed by Latka et al. in 2012, both types of splashing can occur within at the same We and Re numbers [62]. Numerous studies have tried to predict the critical impact conditions that generate the splashing of an impacting droplet [62, 63, 64, 65, 66, 67, 68]. The community agrees that, accurately describing the physics and finding the important parameters governing splashing is still a challenge. The most commonly used parameter to predict splashing is the splashing parameter $K = We^{1/2}Re^{1/4}$ [69] and other parameters include a combination or slight modification of the We and Re numbers, including the capillary number $Ca = \frac{We}{Re}$ [68]. Interestingly, using the Ca number to describe the splashing threshold would imply that, the more viscous the fluid, the lower the critical impacting speed needs to splash. However, studies suggest that the role of viscosity in splashing can be non-monotonic [70, 71]. In 2013 Palacios et al. [64], found that at $Re > 1000$ viscosity promotes both splashing and the gliding of the lamella. In contrast, at small Re numbers, viscous dissipation reduces splashing by inhibiting the break up of the lamella [64, 72]. Further studies conclude that increasing viscosity delays the splashing process [73]. In addition, if the liquid is not in contact with the solid but spreading over a thin sheet of air, viscosity effects are negligible [74, 75].

An important parameter ruling splashing is the ambient pressure. Past studies have found that the ambient pressure can change the critical splashing impact speed. In 2005 Xu et al., concluded that by reducing the ambient pressure splashing can be suppressed, highlighting the relevance of the surrounding air properties [3]. Accordingly, it has been suggested that the air viscosity is the most influential parameter on splashing, with a small contribution from the gas inertia [76]. Surprisingly, it has also been shown that air, at the impact point, plays no significant role on splashing, but is the air at the spreading edge that influences it [46, 63, 77]. Liu, et al. in 2015 conducted an experiment where a droplet impacted substrates with micrometer pores; splashing could be observed for cases where the pores were found around the impact centre but, if the pores were situated near a critical radius from the centre, splashing was not longer observed [77]. Moreover, in a recent work at high We-

ber and Reynolds numbers, Burzynski and Bansmer concluded that splashing is not caused by gas entrainment on glass substrates [78]. The exact mechanism for lamella formation remains unresolved, but the strong influence of air under the expanding liquid suggests that splashing might be initiated by a Kevin Helmholtz (KH) instability [77, 79]. This is, as the air density increases, the number of air molecules at the surrounding volume increases and the shear stress increases [70, 76]. At high impact velocities, the shear molecular forces between air and the liquid film initiates a KH instability that produces splashing at a small spatial scale. From these observations further theoretical and empirical studies have aimed to study the role of the gas dynamics on the lubrication force lifting the lamella [65, 67, 76]. In fact, in 2014, Riboux and Gordillo, using potential flow theory and momentum balance equation, calculated the ejection time of the thin sheet prior splashing and defined a paramater (β) that quantifies the aerodynamic forces needed to overcome the surface tension [65]. This parameter includes the liquid properties and the ambient gas pressure.

On the other hand, there is no accepted consensus on the effect of the substrate wettability on drop splashing. As previously discussed, wettability of a substrate is normally characterised for a liquid droplet at rest (or during a quasistatic process) on a solid surface by the *static* contact angle θ_s, where θ_s is defined as the angle between the tangent of the droplet surface and the tangent to the solid surface at the pinning point. During droplet impact and spreading, the pinning line moves so wettability should be studied in terms of the *dynamic* contact angle θ_D [56]. The dynamic contact angle is measured as the contact line moves, and can be divided in two components: the advancing dynamic contact angle θ_{DA} for spreading droplets, and the receding dynamic contact angle θ_{DR} for receding lines.

Latka et al. in 2017, conducted experiments with silicon oils and water-glycerol solutions at Ca$>$ 1.5 concluding that wettability (in particular θ_s) does not affect the splashing threshold [75]. At this range of capillary numbers the lamella is not in contact with the solid, but glides over a thin sheet of air. Furthermore, a study in rough and porous substrates, with different wettabilities and varying ambient pressures,

found no direct effect of θ_a or θ_r on the splashing behaviour [66]. Therefore, it has been proposed that the splashing threshold depends on the density, surface tension, and diameter of the droplet, and the air viscosity. In contrast studies of solid spheres impacting on liquid pools have found an effect of the wettability on the splashing phenomena and air entertainment [72, 80, 81, 82]. Duez et. al. in 2007, found that the critical velocity for air entertainment on solid spheres impacting a liquid pool is independent of wettability for hydrophilic surfaces (i.e. $\theta_a < 90$ degrees) but the critical velocity scales as $\theta_a^{-1/3}$ for hydrophobic surfaces. The later is an example where surface wettability plays an active role on cavity formation and splashing of solids plunging into a liquid [82]. Changing the wetting properties of the liquid pool (and not the sphere properties) leads to the same conclusion [81]. In the context of drop impacting solids, experimental data has shown that splashing effectively depends on the surface wettability [72, 80]. Experimental studies on oblique impact have shown that hydrophobic substrates exhibit a low-velocity splashing threshold [80]. Simulations have also demonstrated the influence of the dynamic contact angle (θ_D) on the splashing threshold [83]. In these simulations, drop parameters were kept constant and the contact angle was varied. Prompt splash only occurs if θ_D is greater than 90 degrees. Kensuke Yokoi in 2011 also found that spreading (and splashing) is solely govern by inertia at times $t < 0.3$ ms after the impact [83]. In chapter 4 we present our work on the influence of θ_{DA} on splashing.

In the last two subsections we have focused our attention on the droplet impact dynamics on smooth surfaces. However, in most industrial and natural scenarios surfaces are not smooth but have a certain degree of roughness. In the next section we present a review of past works on the droplet impact dynamics on rough substrates and compare it to the the dynamics on smooth surfaces.

1.3.4 Droplet impact on rough and microtextured surfaces: From spreading to splashing

In practice, most surfaces have a certain degree of roughness. Examples of these are the surfaces widely used in industry such as rough metals and paper, to surfaces in

nature such as plant leaves and butterflies wings. In fact, the best-known method to achieve super-hydrophobicity is by adding surface roughness to a material [21, 22]. For these reasons there have been many studies trying to understand the influence of the roughness on the substrate wettability and the influence of the impact outcome [10, 16, 17, 66, 84, 85, 86, 87]. In static conditions, substrate roughness is the responsible for contact angle hysteresis, i.e. the difference between the advancing and the receding contact angles [10]. For a hydrophilic substrate, roughness promotes hydrophilic behaviour, while for a hydrophobic substrate roughness enhances hydrophobicity [10]. For dynamic conditions, roughness alters the contact line dynamics and the splashing threshold [49, 86].

As in smooth surfaces, there is a great interest in finding the maximum spreading diameter d_m upon impact on rough surfaces. In a recent work, surface roughness was parametrised using a scaling that included the dynamic contact angle at maximum spreading [27]. This scaling was used to effectively predict d_m in terms of the We number. For grooved substrates it has been argued that the reduction of d_m in the direction perpendicular to the grooves is due to the pinning of the edge of the drop at the edge of the substrate pillars, causing the contact angle to increase [88]. This defines a pinning coefficient that is proportional to the advancing contact angle and the surface hysteresis. Moreover, it has been found that the slip length is influenced by substrate roughness [49]. In particular, d_m is affected by substrate roughness for water impacting hydrophilic grains [89]. However, for water drops on hydrophobic grains substrate roughness has a minor effect on d_m [89]. The latter experiments show that the substrate roughness is just one of the many variables affecting the dynamics with a certain influence of the intrinsic wettability of the substrate. Experiments have shown that droplets impacting on micro-architectured tapered microposts result in either a pancake bouncing or a recoiling-bouncing regime [90]. For straight posts, the liquid menisci are subjected to constant deceleration, resulting in droplet recoiling before bouncing. Other experiments have shown that an irregular surface roughness results in diverse bouncing regimes, ranging from conventional spreading to partial bouncing due to droplet pinning at the roughness elements [91].

Superhydrophobic micro-patterned substrates can be flooded by liquid due to impact, evaporation and/or condensation, and such *invasion* can be promoted by local extreme roughness protrusions [21, 92]. Surface patterning leads to partial wetting and pinning of the liquid at the substrate surface too. In this transition, a droplet goes from being *suspended* above the substrate to being impaled at the microposts. Whether a sessile droplet impales or remains suspended depends on the architecture of the substrate, the cavity size, θ_D, and the roughness factor [22].

Most past works on splashing have found that substrate roughness promote splashing and even a single protrusion in the substrate can trigger a splash [66, 84, 86, 87, 93]. It has also been found that in some situations surface roughness can suppress corona splashing, while promoting prompt splashing by suppressing thin sheet creation [2, 62, 94]. However, Hao et al., showed that the suppression of corona splash by roughness in non-monotonic [84]. This non-monotonic effect decreases with liquid surface tension [84]. Several parameters have been proposed to successfully characterise the roughness effect on splashing. Among these parameters, the most common are the arithmetic amplitude average roughness (R_a) and the root-mean-square roughness (R_{rms}). For the threshold between splashing and no splashing, a critical We number (as a function of the ratio of the droplet radius to the surface roughness, R_a/D_0) was proposed [86]. More recently, the parameter ($Re^{1/2}We^{1/4}$ (in terms of D_0/R_a) was suggested to separate the splashing and no-splashing phenomena [87]. However, it has also been argued that R_a is not enough to characterise the threshold. Roisman et al. in 2015 demonstrated that the characteristic slope of the roughness of the substrate fits the experimental results in terms of impact Weber number [66]. Recent research on splashing on micro-textured substrates have been devoted to identify the influence of geometry and size of the roughness on the droplet splashing. It has been found that the height of pillars and their spacing are the most important parameters for controlling drop splashing [95]. Compared with smooth surfaces, droplet splashing is enhanced for tall sparse pillars and suppressed for dense tall pillars. In the same study, Zhang et al. (2018) noted that same-size roughness might have a disparate effect on droplets of differ-

ent size [95]. For certain critical ratios of droplet diameter and pillar spacing, the effect of the pillars can banish. Further experiments by Tsai et al. (2009) showed that, for impact events at $We < 120$, the roughness at nanoscale plays a minor role on splashing. However, for faster impacting droplets, splashing is more violent on nanoscale roughness substrates than on substrates with microstructured roughness [91].

In this subsection we have reviewed past works on the influence of the substrate roughness on the spreading and splashing of impacting drops. The main conclusion is that roughness can prevent a droplet from spreading while promoting prompt splashing. The next subsection reviews the transition from bouncing to impaled droplets in micropillared substrates and its similarities with the impact on porous media.

1.3.5 Penetrating surface features: The Cassie-Baxter to Wenzel transition and droplet impact on porous media

Porous surfaces such as textiles, sponges and some types of soil interacting with liquids, are examples of porous media found both in industrial process and nature. Besides the wide range of applications, droplet impact on porous media has not been widely researched. In fact, the transition from the Cassie-Baxter to the Wenzel state, has been the object of numerous studies and share common features with droplet impact on porous substrates. The voids between pillars in microtextured surfaces can play the role of pores and penetration is governed by the kinematic and capillary pressures. The main difference, between the impact in micropillared and porous substrates, is that the droplet can not completely penetrate the microtextured surfaces while it can on the porous ones. Preliminary studies by Reyssat et al. (2006), found that the critical impact velocity U^* for impalement scales as $(\sigma h/\rho w^2)^{1/2}$, where L is the pillar height and w is the inter pillar distance [22]. Similarly, Bartolo et al. (2006), found three different regimes, namely sticky droplets (impalement), bouncing droplets (non-impalement) and non-bouncing droplets (non-impalement) [21]. These experiments showed that critical impalement depends not only on the

height of the pillars but also on the solid fraction; the percentage of solid surface respect to the void. Moreover, the pinning force is dependant on the surface contact angle hysteresis [21]. Accordingly, molecular dynamics simulations and Lattice Boltzmann methods have found similar results [96, 97]. In fact, Koishi, et al. (2009) reached to the same conclusions as Reyssat et al. (2006), finding an intermediate state where both the Wenzel and Cassie-Baxter states are favourable [98].

Studies on droplet impacting a sieve have been done by Lorenceau and Quéré in 2003 [99]. This research showed that under certain conditions, a droplet can penetrate a hole and create a filament along the impacting direction [99]. The generated filament can elongate and break up into secondary droplets. In this study, a critical penetration velocity was found to be dependant on the liquid properties and the pore size, and independent on the surface wettability. Delbos et al. (2010) studied the impact of millimetre-sized droplets on superhydrophobic sub-millimetre-sized capillary tubes and found that the liquid either penetrate or not the capillary tube [100]. For an impact at a high speed, most of the droplet volume would penetrate into the capillary tube and form a *liquid slug*. The slug mechanism has also been found on microtextured substrates and is responsible of the Cassie-Baxter to Wenzel transition [101]. In the case of droplets impacting meshes, recent works have identified three impact regimes, namely *no penetration*, *protrusion* and *complete penetration* [102, 103]. Similarly to microtextured substrates, the critical velocity U^* that divides no penetration from complete penetration is obtained by balancing the dynamic impact pressure $P_d \propto \rho U_0^2$ and the capillary pressure $P_c \approx w/A$, where A and w are the opening area and the perimeter of the mesh pore, therefore $U^* \approx (\sigma w/A)^{1/2}$. In fact, U^* was found to increase as the pore depth increases due to viscous dissipation [99]. In the protrusion regime a portion of the droplet extends beyond the mesh pores and some of the liquid is pushed back to the surface by capillary forces. In the complete penetration case, liquid fingers can be created on the back of the surface and these fingers can break into small droplets. A further study demonstrated that superhydrophobic meshes could effectively resist incoming droplets and eliminate protrusion [104]. However, Ryu et al. found that despite a

drop not penetrating a superhydrophobic mesh upon impact, the droplet could penetrate it while receding and bouncing off the substrate [103]. Additionally, *pancake bouncing* was reported on superhydrophobic meshes [103, 104]. In another work, Bordoloi et al. (2014) studied the penetration of millimetre-sized water droplets ($\approx$ 5 mm diameter) through a millimetric pore while the entire system was submerged in oil. A thin oil film was found to separate the wall of the pore and the droplet (for pores with rounded edges) [105] . In this case, the surface wettability of the pore wall was found to have no effect on the impact but surface wettability affected the penetration dynamics. Additionally, Joung and Buie (2014) investigated the impact of droplets on paper and found four impact outcomes ranging from droplet sticking to the impact surface to splashing, all dependent on the We number [106].

This section has focused on droplets impacting various solid substrates but scarce evidence exists on the impact dynamics on textiles. In fact, past studies on the wetting of fabrics have often focused on static wetting [107, 108]. In industrial environments, liquid repellency of textiles has been sought after using hydrophobic coatings but little attention has been paid to the liquid dynamics or the textile pore size. Chapter 5 presents results on the contact line dynamics of droplet impact on textiles.

1.4 Conclusions

This chapter has reviewed some basic concepts on the wettability and contact line dynamics of liquids interacting with solid surfaces with different characteristics, namely, wettable, non-wettable, smooth, rough, porous and non-porous. We have seen that for a droplet on an ideal surface; smooth, homogeneous, rigid and insoluble the contact angle can be described by Young's Eq. (Eq. 1.3). In addition, for drops resting on rough substrates Wenzel and Cassie-Baxter models are used, depending if the droplet rests between the grooves (Eq. 1.6) of the substrate or if it rests on the top of roughness asperities (Eq. 1.7). Commonly, quasi-static contact angles are used to characterise substrate properties. Yet, there are many situations where the contact line is far from equilibrium and quasi-static angles are not enough to

characterise the surface.

Examples of where the contact line is far from equilibrium are found during the spreading or receding of an impacting droplet on a dry solid substrate. The dynamics of drop impact onto solid substrates has received much attention due to their relevance in inkjet printing [109], paint spraying [110], and other aerosol based coatings [111]. At least six different outcomes of drop impact have been identified: deposition, prompt splash, corona splash, receding break up, partial rebound, and complete rebound [2]. At high We and Re numbers, an impacting drop ejects a thin film, which, in turn, breaks up to form secondary droplets; i.e. splashing [5]. Although many studies have aimed at finding scaling arguments to characterise splashing [62, 63, 64, 65, 66, 73], the exact combination of parameters and their influence have remained elusive. Moreover, there is no accepted consensus on the role of surface properties on drop splashing. Consequently in Chapter 4 we study the relevance of surface properties on splashing, in particular, wettability and surface roughness.

Furthermore, we reviewed experiments and theory developed for the impact on microtextured substrates and metallic meshes. In particular, we focused on the Cassie-Baxter to Wenzel transition. The transition is given by the height of the pillars, the solid fraction of the microtextured substrate and the impact velocity [22]. Similarly, for droplet impact on metallic meshes it was found that the critical penetration speed is scaled by the ratio between the area and perimeter of the pore and the surface tension of the liquid [104]. However, research in droplet impact dynamics on textiles, is scarce, despite its importance in industry and for creating protecting clothing. In Chapter 5 we present experimental results on the contact line dynamics of droplet impact on textiles with different wettability.

It is clear that many past works on droplet spreading and splashing rely on the detection of the contact line, and on the measurement of the contact angle. However, a standard measurement method is unavailable and, consequently, the contact angle is often obtained and reported using different techniques. Next chapter (Chapter 2) presents an automated polynomial fitting algorithm that can extract the dynamic

contact angle of an impacting droplet during the spreading and receding phases. In addition, the algorithm can extract the impact velocity of the droplet, as well as its initial and spreading diameters. Furthermore, next chapter presents the general experimental setup used in chapters 3-5.

Chapter 2

Experimental Methods

This chapter describes the general experimental setup used throughout the thesis. Additionally, it presents a Matlab routine to measure the dynamic contact angle and its validation.

2.1 Introduction

The experimental setup used in this thesis is described in this chapter together with a brief description of the data acquisition and analysis; further details and specifics are seen in next chapters. In brief, the experiments consisted off single drops travelling vertically to impact onto dry solid substrates or nylon textiles at a constant speed with the substrate perpendicular to the impact direction. In these experiments drop impact speeds ranged from 1.1 to 4.9 m/s and the drop diameter ranged from 1.1 to 2.5 mm. The substrate position was controlled by servo controlled and an arduino, and allowed different inclinations. In all the impact experiments in this thesis the substrate was set at $\phi = 0$ degrees with respect of the horizon. The experiments are recorded with a high speed camera and the image analysis is done through MATLAB. A picture of the experimental set-up is shown in Figs. 2.1 and 2.2 shows a diagram of the rotating platform system.

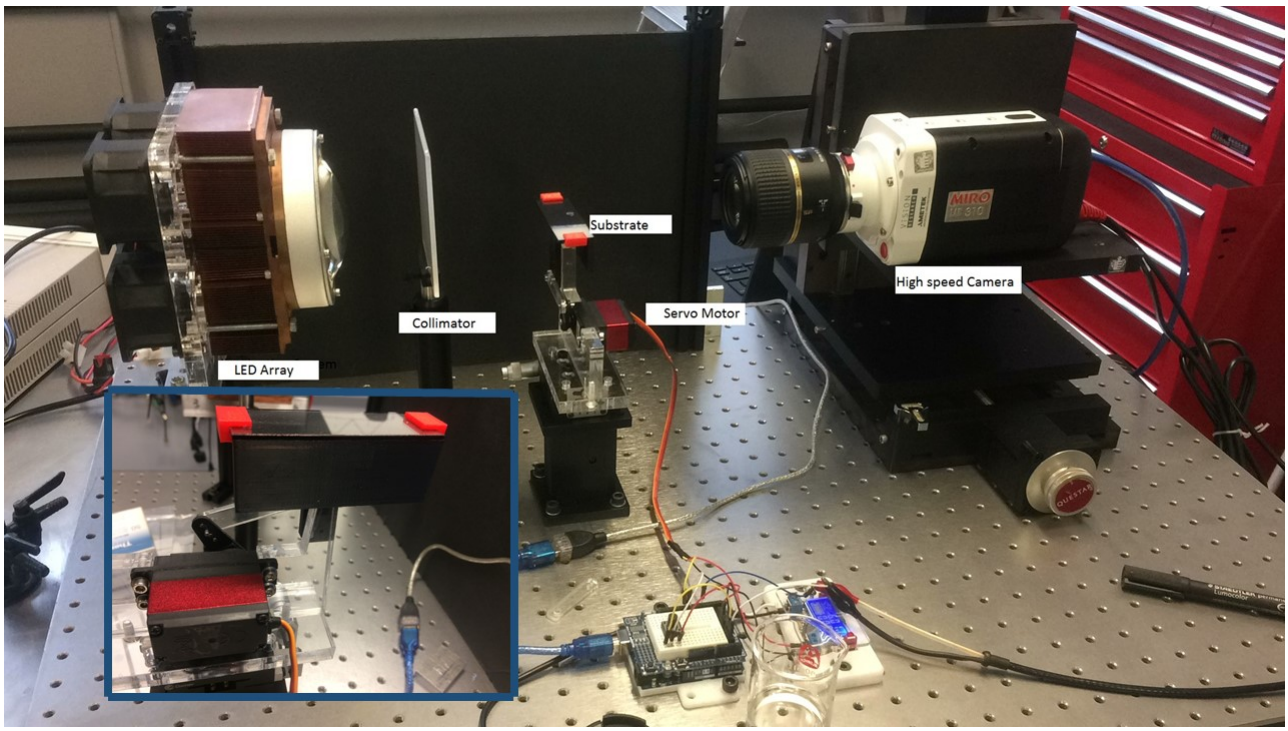

Figure 2.1: Picture of the experimental setup. A lateral view of the experiment is presented. The picture shows a high-speed camera, a tilting substrate, a diffuser and a LED array.

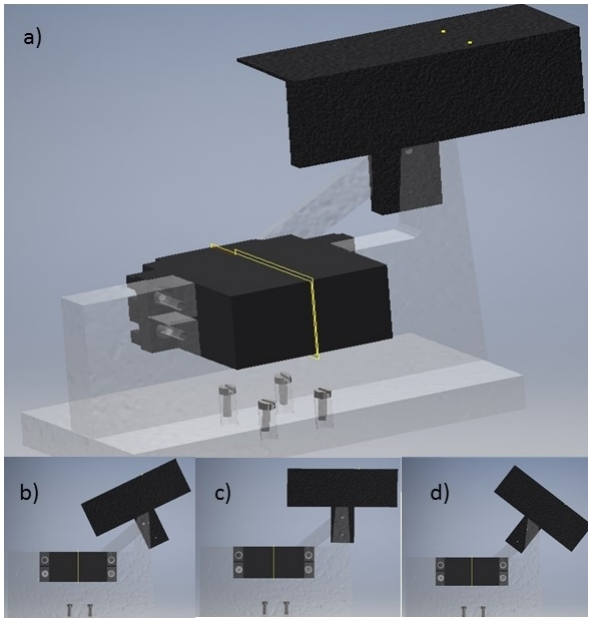

Figure 2.2: Diagram of the tilting platform; a) lateral view at the starting position, b) platform set at an angle $\phi > 0$, c)platform starting position ($\phi = 0$) and d) platform set at an angle $\phi < 0$.

2.2 Measurement of liquid properties

The viscosity, surface tension and density of the liquids used throughout this thesis where measured at room temperature. Viscosity was measured with a Viscolite 700. The viscometer, calculates the viscosity from the damping that occurs when its steel sensor vibrates inside the liquid. The accuracy of the viscometer is 0.0001 Pa s. Additionally, surface tension was measured with a SITA pro line t15, which uses the bubble pressure method. This method consists of introducing a capillary that pumps air inside a liquid, thus creating a bubble. This bubble is exposed to the liquid pressure, then the gas pumped in the capillary tube until the pressure inside the bubble reaches a maximum. Soon after the bubble detaches from the capillary tube and a new bubble forms. The resolution of the SITA pro line t15 is 0.1 mN/m with a repeatability error of 0.5 mN/m. Correspondingly, the density of the liquids was measured with a Densiti-meter, DMA 35, PAAR. The density meter benefits from the pulsed excitation method. In the later, a U-shaped tube made from borosilicate glass or metal is excited to oscillate at its characteristic frequency, which is directly related to the density of the sample. The resolution of the density meter is of 1 kg/m^3.

2.3 Droplet generation

Liquid drops were generated by two methods; dripping and by drop on demand. In the dripping method, drops were produced by a 1.0 mm diameter metallic syringe tip attached to a syringe pump (Razel, model R99-E) that pushes the liquid at a rate of 1.94 mm^3/s until the drop falls. Droplet growth and detachment is governed by surface tension of the liquid as it tries to minimise surface energy by minimising the surface area of the liquid [112]. During this process, the geometry of the liquid droplet is transformed from spherical to a pearl shaped due to the addition of liquid through the pump. Soon after the detachment, the droplet starts to oscillate. Oscillations are viscosity dependent and are dampened with time until the drop becomes spherical [113]. In this experiments the in flight time of the droplet was enough to not observe droplet oscillations. Droplet volume is controlled by the needle radius (R), flow rate (Q), gravity (g) and the liquid's surface tension and viscosity. To determine the size of each droplet detaching from a needle, we have to balance the weight with the capillary forces. Considering that the droplet is fed quasistatically, we have that, $\rho\Omega g = 2\pi R\sigma$, where Ω is the droplet volume. On the other hand, Ω can be written in terms of the drop radius (R_0) and the capillary length λ_c as, $\Omega = 2\pi R\lambda_c^2 = \frac{4}{3}\pi R_0^3$, therefore,

$$R_g = (\frac{3}{2}Rlambda_c^2)^{1/3} \tag{2.1}$$

Taking into account the flow rate, Schele and Meister (1968) found the following equation [114],

$$\Omega \propto \left[\frac{2\pi\sigma R}{g\rho} - \frac{4Q^2}{3\pi R^2 g} + 7.14\left(\frac{Q^2R^2\sigma}{g^2\rho}\right)^{1/3}\right] \tag{2.2}$$

The advantage of the dripping system is its simplicity and reliability. The droplets generated with this systems had a standard error of ± 0.01 mm per experiment. The drop impact velocity (U_0) was adjusted by varying the distance from the needle to the substrate.

In the drop on demand method system (Fig. 2.3), a loudspeaker functions as

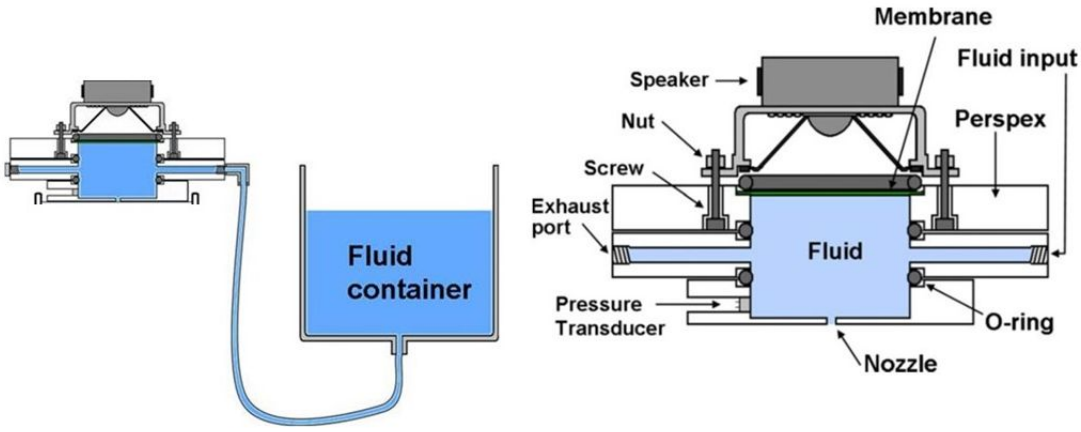

Figure 2.3: Schematic diagram of the droplet generator. Figure taken from (J. R. Castrejón-Pita, et. al. on Review of Scientific Instruments 2008).

the actuator, pushing the liquid through a nozzle to create a droplet. The system is prepared to produce droplets in the following manner. First the actuator is filled with liquid, taking care that the actuator has no air bubbles - as air bubbles would compress and cause dissipation of the pressure, preventing the system from ejecting the droplets. This is achieved by connecting an external container to control the filling by rising it until some liquid comes out from the exhaust port. The exhaust port is then closed and the height of the external container is adjusted to balance the pressure in the system and no liquid comes out of the nozzle. Finally, droplets are generated by sending a pressure pulse to the actuator. In this system, the droplet velocity and volume is determined by the pulse duration, pulse amplitude and the number of pulses. Pressure pulses can be delivered in two ways. In single pulse mode, a function generator activates a relay that switches a dc voltage to the loudspeaker, to create a single pressure pulse that drives the liquid out of the nozzle. In the second mode, an audio power amplifier is used to amplify the amplitude of a pulse from a pulse generator (TTi). In these experiments, a 1 mm outer diameter conical nozzle was used. The driving signal is produced by a pulse generator and an amplifier. The waveform is kept to a single square pulse, with control of the pulse amplitude and width, to adjust droplet impact speed and size. The impact speed can also be controlled by adjusting the print-head height. The advantage of this system is that the impact speed as well as the droplet size can be adjusted for a single nozzle. Moreover, changing the nozzle size permits a wider droplet

diameter variability. This system has been proven to successfully create droplets of ethanol, viscous aqueous mixtures of glycerol and with viscosities up to 20 cP, liquid latex (Chapter 6) and hydrogels containing skin cells [115]. However, the system is very sensible to the meniscus position and perfectly spherical droplets are difficult to produce reliably. Moreover, water droplets generated with this method tend to oscillate more than with the dripping method. One solution to prevent drop oscillation is by the use of viscous fluids.

Is noted that evaporation is not expected to play a role in these experiments. A recent work by Niimura and Hasegawaka in 2019 demonstrated that similarly sized (D_0 = 1.4 mm) ethanol droplets, levitated in air at ambient temperature, initially evaporate at a rate of 2.5 % in 5 seconds [116]. Assuming this evaporation rate, our 1.9 mm diameter droplet would reduce its diameter by 0.3 μm in the 3.0 ms duration of our experiments. This is below the resolution of our optical system and its effect negligible in the experimental error.

In conclusion, both drop generating systems allows the control over a wide range of the impact velocities, liquid properties and size of the droplets. Furthermore, in both systems the error in the droplet diameter does not exceed the 0.12 mm.

2.4 Image analysis

The recording of drop impacts was carried out with a Phantom V710 coupled with a Narvitar microscope lens. For a typical experiment performed in this thesis the camera resolution was set to 1280×256 pixels^2 at a sample rate of 23000 frames per second and an exposure time of 10 μs. The spatial calibration was made with a graduated glass disk with a minimum resolution of 0.1 mm. The size of the graduation lines is ≈ 2 pixels. The effective resolution of these experiments measured by counting the number of pixels in 5mm was of 6.47 ± 0.13 μm per pixel. The camera was inclined $\approx$ 2 degrees, to obtain a clear image of the contact line and was illuminated with a 300 W LED through a diffuser. We expect little influence of this inclination on the measured angle; we discuss this in subsection 2.3.2. The depth of focus was set so that it includes all the drop volume. Special attention was

given to the alignment between the focal plane of the camera and the plane where the droplet rested - misalignment *hides* the true contact point and therefore results in an incorrect contact angle measurement. After each experiment the substrates were cleaned, first with a dry piece of fabric and then with a piece of fabric with ethanol and then rinsed with distilled water. To ensure the dryness of the substrate, compressed air was blown over its surface for 30 seconds and five minutes were waited before performing the next experiment.

Image analysis to extract the (dynamic) contact angle at each frame was performed by using a custom-made MATLAB code. In brief, the code works as follows: it takes an image and converts it to grey-scale and then into a binary image using Otsu's method [117]. It then detects the boundary of the droplet, the substrate, and the contact point between the droplet and the substrate. The MATLAB code works by fitting a polynomial of order n to a portion of the droplet profile near the contact line. The droplet and substrate profiles are then extracted as arrays of pixels. The left-hand and the right-hand sides of the droplet boundary are independently analysed. The pinning points are identified and recorded in all images to track the spreading diameter and thus the contact line velocity. For the left-hand side, the code selects a set region of the droplet boundary array from the first entry (pinning point) to the set length of n pixels, this forms a perimeter of length δ_n as seen in Fig. 2.4. The right hand side region follows the same method but from the right pinning point. The code then fits an m-order polynomial with the least squares method (OLS) to these n pixels of the boundary (δ_n in each side). It then computes its derivative and evaluates it at the pinning point: the contact angle is then computed from this value. We varied δ_n (the number of pixels n along the droplet profile used to fit the polynomial), and the order of the polynomial to find the optimal setup to measure the contact angle.

Droplet impact velocity and droplet diameter before impact were also extracted from this code by tracking the centroid of the droplet for each frame before the first contact with the solid or by taking the difference from the leftmost and rightmost points in the droplet boundary and the uppermost and lowermost points of the

droplet boundary prior impact.

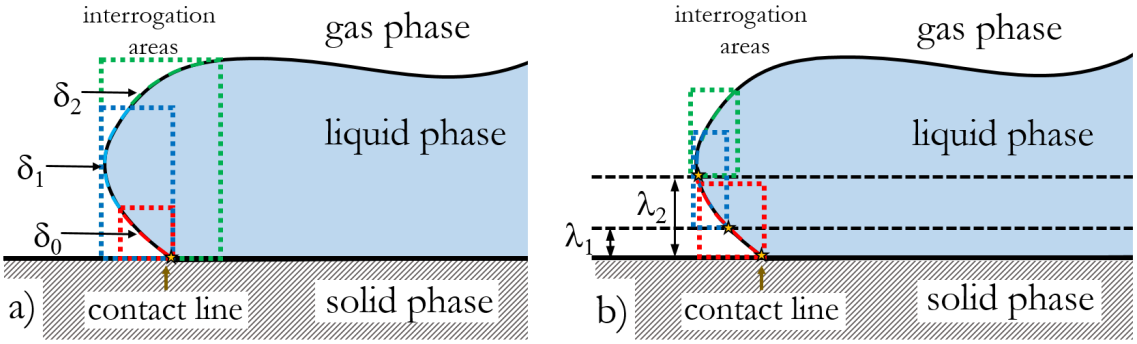

Figure 2.4: Sketch showing the variables studied in this work. The contact line (or the triple point) is shown as a star and indicates the place where all the three phases meet. In a) the interrogation areas define a perimeter along the droplet's profile of size δ (in pixels). In b) the flat *horizon* given by the substrate is seen as a black thick line; image analysis might misplace its position by a height λ due to the interface being out of focus or fuzzy.

Figure 2.5 shows a sequence of images of a typical spreading experiment after the impact of a water drop on a hydrophilic substrate as analysed by our algorithm. The figure presents the first spreading and receding cycles of the impacting liquid droplet, where for most of the hydrophilic substrates the receding is negligible. As described in previous papers, at early times after the liquid droplet touches the substrate the contact angle is near 180 degrees. However due to the limited resolution of the camera, the maximum contact angle that can be measured is ≈ 160 degrees. This is seen in the first row of Fig. 2.5a); on the second row of the figure we observe the time instant where $d(t) = d_{max}/2$; on the third panel we have $d(t) = d_{max}$ (and $u_{cl} = 0m/s$); and on the bottom panel we observe the receding process.

2.4.1 Parameter optimisation and validation

This section focuses on the analysis of a static droplet on an acrylic surface and on 4 different instants during droplet spreading, i.e. i) the time of the first contact, ii) the point where $d(t) = d_m/2$, iii) the time where $d(t) = d_m$, and iv) the first point of receding. Accordingly, at these times, the droplet contact angle is measured, using different droplet profile lengths (δ) while varying the order m of the fitting polynomials. As noted by [25], the order of the polynomial used to adjust the droplet shape at the pinning point is crucial to the value of the contact angle on sessile droplets. An analysis of 100 pictures of a standing droplet was performed

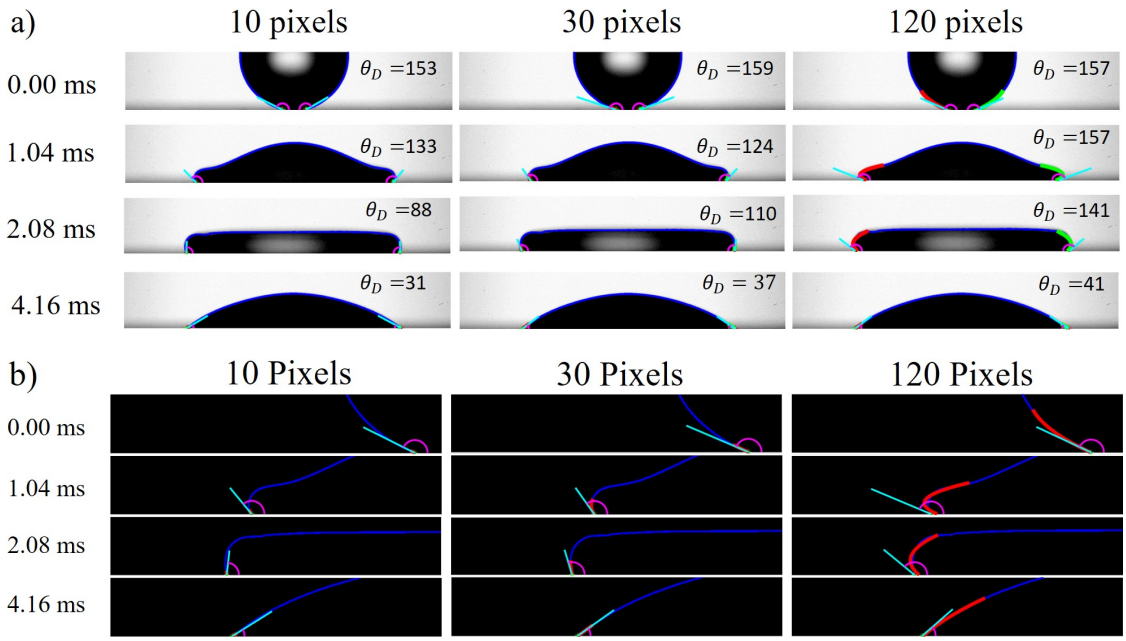

Figure 2.5: a) Example snapshots of the experimental and analysed images. The three sets correspond to the MATLAB processed images of a drop in the spreading phase. The images are arranged according to the number of pixels used to fit a second-order polynomial to calculate the contact angle, i.e., 10 pixels $\rightarrow \delta_1/D_0 = 0.0301$, 30 pixels $\rightarrow \delta_2/D_0 = 0.092$, and 120 pixels $\rightarrow \delta_3/D_0 = 0.369$. The navy blue contour corresponds to the droplet boundary, the red (left) and green (right) stars show the pinning points, the light blue lines correspond to the tangent evaluated at the pinning point and the pink arcs correspond to the contact angle; b) shows a close-up of the droplet contour detected by the MATLAB algorithm.

to test the stability of the algorithm at static conditions. The measurement was done with a second order polynomial and profile lengths corresponding from 5 to 50 pixels. Table 2.1 shows the average value of the given contact angle, the standard deviation and the net error; the net error is the difference between the minimum and maximum value of the measured contact angle. Table 2.1 indicates that the best operation condition is to take 50 pixels, however, as discussed later, this might not be the case for droplet spreading. In addition we performed an analysis of the same 100 pictures for a direct differentiation method. This method consists of taking to pixels of the droplet profile and performing the derivative without adjusting a polynomial. With this method the average contact angle is 56 degrees, with a standard deviation of 19 degrees and a maximum error of 45 degrees. With a standard deviation of ~ 34 degrees for the static condition. Thus, we conclude that this method is unsuitable for determining the contact angle of a droplet. In this work, we have extended this study to other conditions where the droplet is far from equilibrium and, thus its

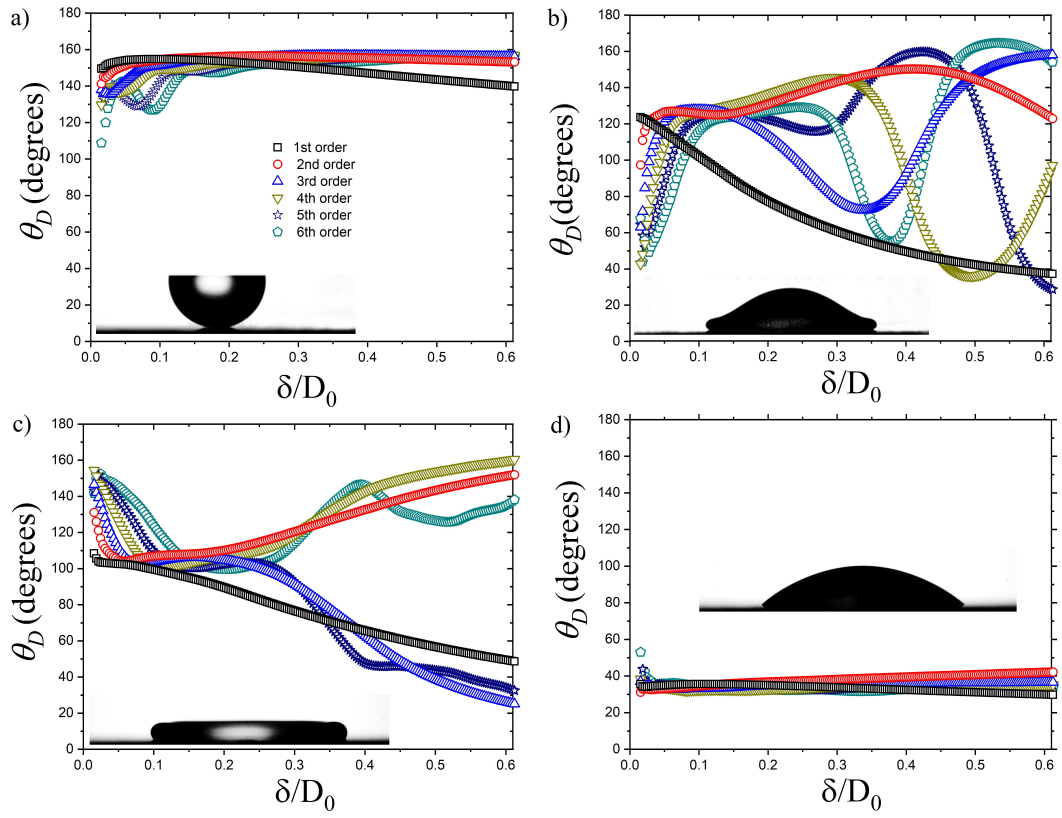

Figure 2.6: Contact angle in terms of the number of pixels used to fit the droplet profile. The image shows as well different polynomial orders. The experiment used for this analysis was experiment number 5.

shape differs from a spherical cap. Our first set of results is seen in Fig. 2.6 where the contact angle is obtained for various polynomial orders at the four relevant times previously discussed. Additionally, Fig. 2.6 shows the contact angle obtained in terms of the ratio between the number of pixels used to fit a m-degree polynomial and the diameter of the impacting droplet (δ/D_0). These results show that the measurement of the contact angle is sensitive not only to the polynomial order but also to the instantaneous shape of the droplet. In fact, for highly deformed droplets, differences of up to 100 degrees in the measured contact angle are seen between the different-order polynomials. In these conditions, the polynomial order showing the largest differences is that corresponding to a linear fit. As seen, for the linear fit ($m = 1$), the dynamic contact angle decreases monotonically for increasing profile lengths for the four droplet shapes studied here. In fact, even at instants where the droplet resembles spherical shapes, i.e. first contact (Fig. 2.6a) and first receding instants (Fig. 2.6d), differences on the contact angle of up to 30 degrees are found for $m = 1$. In contrast, higher order polynomials reach a stable contact angle value

as the size ratio domain is increased.

Table 2.1: Contact angle average and standard deviation for different number of pixels. The contact angle of a water droplet on acrylic is calculated from 100 images, an average and its standard deviation are calculated for each number of pixels of the second order polynomial adjusted to the droplet profile.

Number of pixels	Average contact angle (degrees)	Standard deviation (degrees)	Net Error (degrees)
5	58	2.4	7
10	59	1.8	9
15	58	1.8	7
20	58	0.8	4
25	58	0.7	2
30	59	0.6	2
35	60	0.4	2
40	60	0.4	2
50	60	0.3	2

Largely deformed droplets also offer intricate variations (Figs. 2.6b and 2.6c). Here, large differences in the contact angle value are observed for the various polynomial fittings and fitting domains. As seen in our results, variations of up to 80 degrees can be obtained for droplets shapes in the early spreading phases (Fig. 2.6b) or up to 30 degrees at the maximum spreading diameter where droplets acquire the characteristic pancake shape (Fig. 2.6c). In practical terms, the contact angle should be measured at the proximity of the contact line; consequently, any measuring method should include an upper limit for the length domain. Moreover, as seen in Fig. 2.7, for a time at $d(t) = d_m/2$ a large number of fitting pixels, translates in an inadequate fitting of the droplet profile. This is due to the high droplet deformation far from the contact line. Additionally, a lower domain limit should also exist for the fitting to correctly represent the droplet shape.

As expected, the standard deviation obtained from all the polynomials is consistently low for the receding case where the shape resembles a spherical cap. A similar behaviour is found at the point of first contact where a low deviation is seen for domains larger than 30% of the droplet diameter. As discussed, in these two cases, the droplets are not largely deformed, resemble spherical bodies, and, therefore, good fittings are obtained over a large fitting domain. The standard deviation for largely deformed cases is rich but shows limited variations at short profile domains. Impor-

tantly, the standard deviations present local minima around the domain range of $\delta/D_0 = 0.04$ to 0.10, where the various polynomial fittings seem to agree within a standard deviation of 15 degrees. Moreover, the standard deviation in this region is particularly low (≈5 degrees) for the highly deformed shapes and the receding case. As a result, we conclude that a robust domain for a polynomial fitting is within the range corresponding to profile lengths of 4 to 10% of the droplet diameter. This fitting range is consistent with previous research asserting that larger domains might not trace the drop profile accurately [118]. This upper limit has also been discussed by [29], where their domain is determined by the need of their mask to follow the droplet curvature, which requires a small mask, and "accuracy in their area measurement, which requires a bigger mask". Technically speaking, our upper domain limit can extend to the contact line found at the other end of the droplet contour. However, as noted by other authors, we argue that the contact angle should be measured locally. Our optimum region of measurement is found where the standard deviation of the data is at its minimum value, across the various shapes.

Our next analysis focuses on the standard deviation in terms of the polynomial order; this is shown in Fig. 2.8. Interestingly, for the four shapes, the second order polynomial fitting consistently produces the lowest standard deviation. In fact, this polynomial order has been used by other authors [118]; here we confirm that this fitting is the most robust for dynamic contact angle measurements.

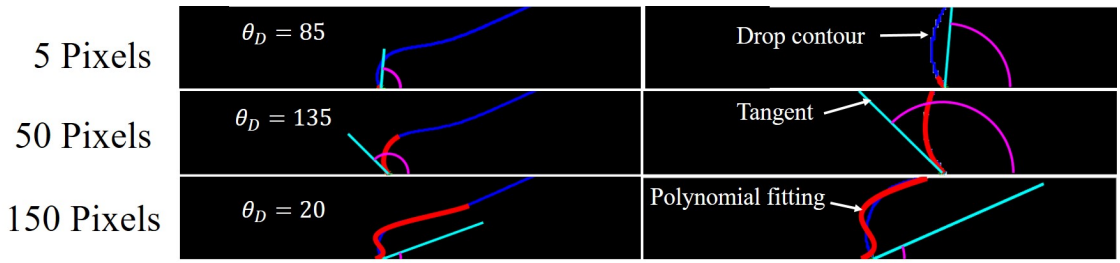

Figure 2.7: Image analysis results of a fourth-order polynomial fit for various number of adjusted pixels δ/D_0, at a time when $d(t) = d_m/2$. This example shows that the polynomial no longer faithfully represents the profile of the droplet when the number of adjusted pixels is 150. This is due to the high droplet deformation far from the contact line.

Based on our results, we conclude that the fitting that produces the most accurate results across conditions is a second order polynomial fitting with a droplet

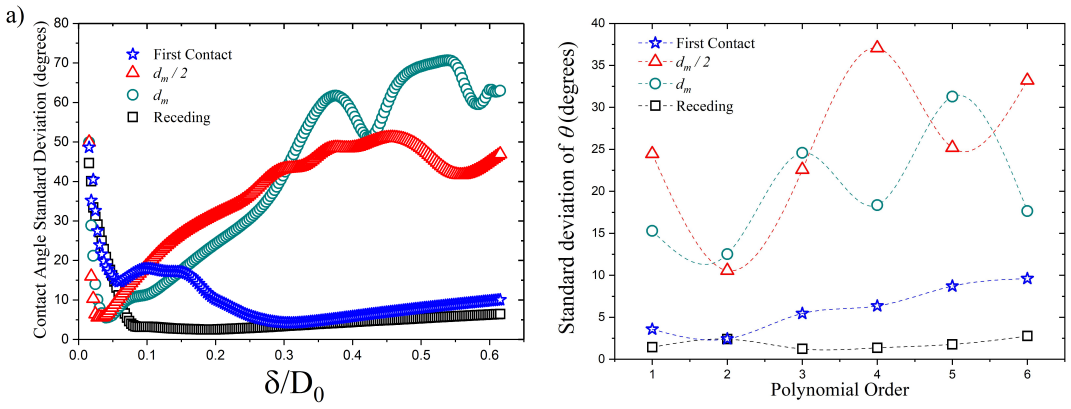

Figure 2.8: a) Standard deviation in terms of the dimensionless adjusted number of pixels (δ/D_0). The standard deviation is calculated based on all the polynomials used in the analysis, for each δ/D_0. b)Standard deviation of the contact angle calculated in terms of the polynomial order. The standard deviation is the associated to all the δ/D_0 considered in this paper for each polynomial. As seen, the quadratic polynomial shows the smallest deviation for all cases.

profile length corresponding to 5% of that of the initial droplet diameter. Therefore, in the following sections, we strictly use these conditions for the contact angle measurements.

2.4.2 Contact Line and Pinning Points

Results indicate that another important variable affecting the correct measurement of the contact angle is the identification and location of the pinning points. This issue is often encountered for fuzzy or out of focus images. The effect of offsetting the position of the substrate plane (horizon) on the measurement of the contact angle, this is illustrated in Fig. 2.4b. Here, a distance λ in pixels is added to the true substrate position. Figure 2.9 shows the variation of the contact angle measurement for a second order polynomial fit with 30 pixels profile, varying λ from -10 pixels to 10 pixels for the four different stages of the impact (first touch, $d_m/2$, d_m and receding). Our results are conclusive; an offset from the true pinning point can result in important differences in the measurement of the contact angle. In fact, an offset of only five pixels ($\lambda/D_0 = 0.02$) is enough to produce differences of up to 19 degrees in the measurement. This miscalculation might be evident and easy to fix on a single picture, but dynamic systems require the automatic measurement of the contact angle for thousands of pictures where a plethora of shapes are found. The

effect, during the spreading phase (Fig. 2.9b), leads to a difference of 24 degrees in the measured contact angle for a pinning point that is placed 10 pixels above its true position. As explained before, as done by other authors, the camera is inclined into a small angle ≈ 2 degrees to achieve a clear view of the contact line. Inclining the angle of the camera Φ affects the measurement of θ_D, but allows to fully capture the surface. This inclining angle changes the projected height (h') captured by the camera and is related to the true height h by $h' = hcos(\Phi)$. Consequently, in our experiments the angle of the camera affects the measurement of the contact angle by 0.6%.

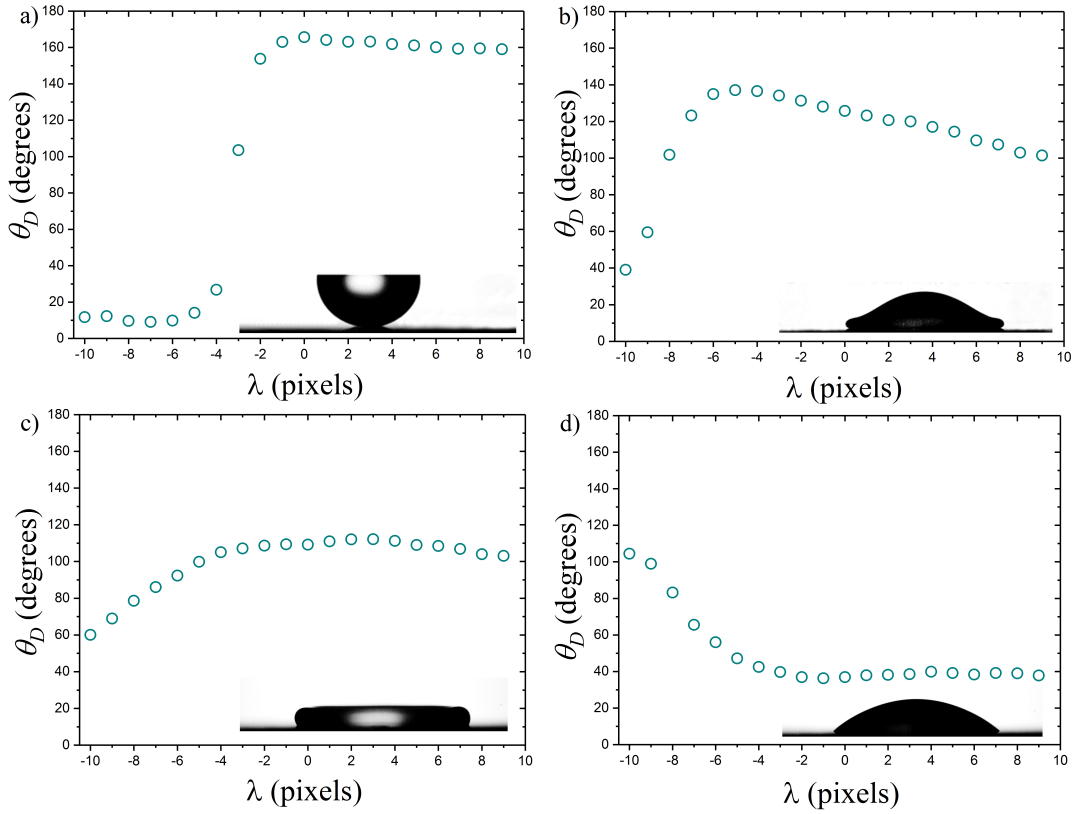

Figure 2.9: Influence of a vertical offset applied to the contact line (of height λ) on the contact angle measurement. The offset is set manually within the MATLAB code, from 10 pixels below to 10 pixels above the contact line. As seen, the measurement of the contact angle is critically dependent on the correct detection of the contact line.

2.4.3 Comparison of the experimental method with simulations

A comparison with the existing literature was conducted by replicating the conditions of Yokoi et al. (2009) and compared with the numerical simulations [41].

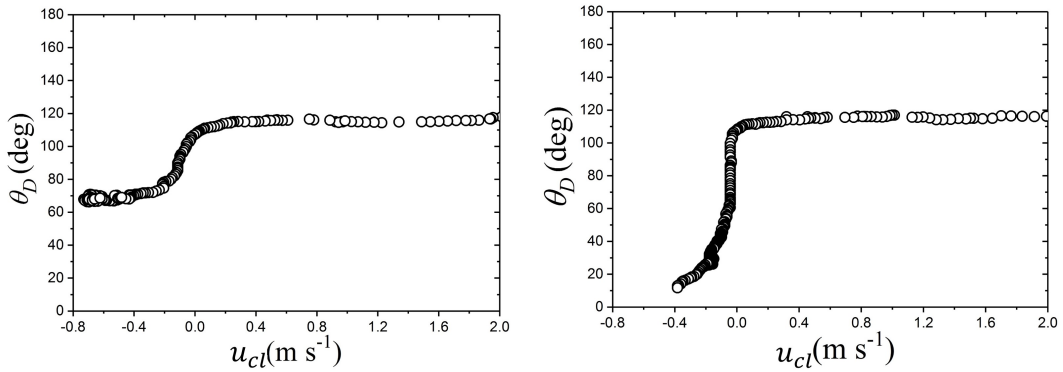

Figure 2.10: Dynamic contact angle in terms of the contact line velocity of a water droplet impacting at 1 m/s on a Parafilm (left) and a Teflon substrate(right).

Table 2.2: Asymptotic advancing and receding contact angles for the Parafilm and Teflon surfaces.

Surface	Advancing contact angle ±3 degrees	Receding contact angle ±3 degrees
Parafilm	115	69
Teflon	115	13

These numerical simulations required the asymptotic advancing and receding contact angles as inputs to model the spreading diameter dynamics. Experiments were performed on two different substrates, namely Parafilm and Teflon. Droplets were generated by dripping and the impact speed was set to 1 m/s. The contact angle measurements are shown in Fig. 2.10, and the asymptotic contact angles are given in the table 2.2. Fig. 2.11 shows results comparing the spreading diameter of the numerical simulation with the experimental results. As shown, the simulation of the water drop impacting the Parafilm match almost exactly. For the impact on the Teflon surface, the spreading phase is matched reasonably well by the simulation, however for the receding phase the spreading radius is underestimated. We note that the numerical simulations of Yokoi et al. (2009) were validated with a surface with similar wetting properties as the Parafilm [41]. Moreover, the hysteresis of the Parafilm is less than the hysteresis on the Teflon. Therefore we attribute the mismatch of the simulations and experiment on the Teflon to the inability of the code to correctly take into account the larger hysteresis of the Teflon substrate.

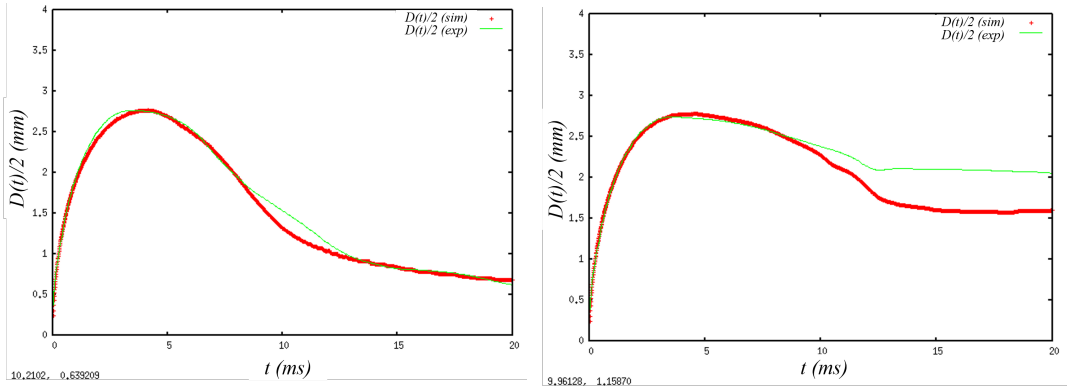

Figure 2.11: Comparison between experiments and numerical simulations of the spreading diameter of a water impact droplet impacting at 1 m/s on a Parafilm (left) and Teflon (right) surfaces.

2.5 Conclusions

In conclusion, this section has presented a robust MATLAB algorithm that can detect the contact line and determine the dynamic contact angle of a spreading and receding droplets. We found that the polynomial fitting method is dependent of the polynomial order and the number of pixels used to fit the droplet profile. With these considerations, we found that a second order polynomial and 30 pixels are the optimal parameters, for an experimental resolution of 6.47μm and a droplet size ranging from 1.98 to 2.63 mm. In addition, we showed the importance of measuring the contact angle at the proximity of the contact line. Furthermore, we have included a comparison with simulations from Yokoi et al. (2009). These simulations take the experimental dynamic advancing and receding contact angles as an input to predict $d(t)$. The experimental results are well captured by the numerical simulations, except for the equilibrium diameter for the impact experiments on Teflon. We argue that this discrepancy is due to limitations in the simulation where the large hysteresis seen in the Teflon substrate cannot be implemented in the code. Having validated our methodology with previous results, the next chapter is focused on the study of the contact angle dynamics of a droplet spreading on hydrophilic substrates. In addition, the next chapter (Chapter 3), presents results on the droplet contact dynamics in two scenarios; of a droplet in a tilting plate and upon impact on a solid substrate.

Chapter 3

Contact Angle Dynamics on Hydrophilic Substrates

This chapter experimentally studies the contact angle dynamics of a liquid droplet resting on a hydrophilic tilting plate. It also presents results on the droplet impact contact line dynamics on a hydrophilic solid surface.

3.1 Introduction

The sliding of a droplet on a tilted substrate and droplet spreading during impact are used for surface characterisation. The most relevant parameters measured from this experiments are the advancing and the receding contact angles, θ_a and θ_r respectively. The difference between θ_a and θ_r is named contact angle hysteresis. Contact angle hysteresis is relevant for inkjet printing [109], paint spraying [110], and other aerosol based coatings [111], as it measures the shear and tensile adhesion forces [119]. However, contact angle measurements have proved challenging for both of the methods. It has been argued that determining the contact angle from the tilting plate method is sensitive to the drop placement [23]. In contrast, a standard method for measuring the dynamic contact angle is not available.

This chapter studies the contact angle dynamics in a tilting plate and upon droplet impact on solid substrates. The contact angle measurements are performed with the MATLAB algorithm and the setup described in Chapter 2. For the tilting plate, we study the contact angle dynamics at different tilting speeds. For the impact experiments we explore a combination of different We and Re numbers. In these experiments we limit the analysis to liquid droplets of diameter less than the capillary length ($\lambda_c = \sqrt{\frac{\sigma}{\rho g}}$) and to Weber and Reynolds numbers leading to smooth spreading and deposition. We compare the results from the two approaches and conclude that the underlying physics in the two cases is different.

3.2 Experimental details

3.2.1 Tilted plate experiments

These experiments consisted of a liquid droplet placed on a tilting substrate (2.2). The droplet was placed by hand using a micro-pipette with a hydrophobic tip. A servo controlled by an Arduino controllably inclined the substrate. The system permitted different step rates and inclinations. The liquid used in the experiment was a glycerol-water mixture with a dynamic viscosity of 12 mPa s, and the substrates used were glass and acrylic. Droplets of glycerol-water mixture of 20.0 $\pm$ 0.2 μL

were generated with a pipette and placed by contact-deposition on the centroid of the substrate. The droplet volume was constant in these experiments. The angular motion of the substrate was normally started 2 minutes after deposition to achieve hydrodynamic equilibrium. The substrate was placed on the top of the tilting platform moved by the servo motor (Ripmax Quartz QZ502). The servo, controlled by the Arduino Uno, inclined the substrate 0.55 degrees per step. The control is flexible but in these experiments delays of 10 ms, 15 s and 30s between steps (being the 10 ms delay the fastest step rate and 30 s the slowest) were used, corresponding to step rates of $\omega_1 = 58.74$ rad/s, $\omega_2 = 0.04$ rad/s and $\omega_3 = 0.02$ rad/s respectively. The inclination range was set between a maximum tilting angle (measured in the anticlockwise direction) and a minimum tilting angle (measured in the clockwise direction) at which the droplet did not slide. The tilting angles are referred as ϕ_{max} and ϕ_{min} respectively. The schematic diagram of these variables is shown in Fig. 3.1. During setting up, the substrate was slowly rotated in the anticlockwise direction until it attains the angle at which the droplet started to slide; ϕ_{max} was defined as this angle. The substrate was kept at ϕ_{max} for one minute, to prove that ϕ_{max} was in fact the no slip angle. A similar procedure was carried out to find ϕ_{min}, with the difference that the substrate was rotated in the clockwise direction. The depth of focus of the visualisation setup was set to include all the drop volume. Special attention is given to the alignment between the focal plane of the camera and the plane where the droplet rested, as misalignment "hides" the true contact point and results in an incorrect contact angle measurement. For the glass substrate, ϕ_{max} = 4 degrees, and ϕ_{min} = -4 degrees and for acrylic ϕ_{max} = 15 degrees and ϕ_{min} = -15 degrees.

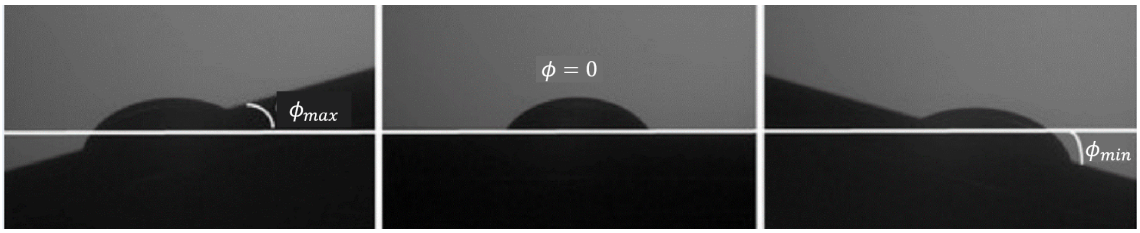

Figure 3.1: Experimental pictures showing how the different inclinations of the substrate were measured: a) ϕ_{max}, b) $\phi = 0$ and c)ϕ_{min} of a water-glycerol droplet deposited on acrylic.

Table 3.1: Fluid properties used throughout the experiments of this chapter

Fluid	Viscosity (mPa s)	Surface tension (mN/m)	Density (kg/m^3)
Distilled Water	1	70.8	998
Mix 1	2	70.3	1065
Mix 2	60	66.0	1126

The rotation of the substrate was executed in a cycle as follows: first the inclination of the substrate was set to 0 degrees and then tilted at a given speed in the anticlockwise direction until it reached ϕ_{max}. Then, the substrate was tilted in the clockwise direction to reach ϕ_{min}. Finally, the substrate was returned to its initial position (0 degrees). The cycle was performed at a constant tilting velocity. Videos were recorded using a monochrome Phantom Miro Lab310 high speed camera with a Tamron SP AF60 macro lens. The resolution of the video was set to 640×480 pixels^2 with a sample rate of 24 frames per second and an exposure time of 10 μs, for ω_1. For the droplet on acrylic moving at ω_2 and ω_3 a picture was taken every 15 s and 30 s respectively with a resolution of the pictures of 1280 × 800 pixels^2. The effective resolution of all the experiments was of 35.4 pixels/mm.

3.2.2 Impact experiments

The impact experiments consisted of creating single drops, which travelled vertically to impact onto dry solid substrates. The droplets impacted at a constant speed and the substrate was placed at $\phi = 0$. The substrates used here were, glass and acrylic. Water-glycerol solutions and pure water (see table 3.1 for fluid characteristics) drops were generated by dripping and drop on demand, which are described in Chapter 2. In these experiments drop impact speeds ranged from 1.1 to 1.7 m/s and the drop diameter ranged from 1.1 to 2.5 mm. Table 3.2 shows the experimental conditions. Technical details on the imaging processing method and analysis are provided in Chapter 2.

Table 3.2: Experimental conditions

Experiment Number	Drop Generation Method	Substrate	Liquid	$D_0(mm)$	We	Re
1	Dripping	Acrylic	Water	2.41	43	2736
2	DoD System	Acrylic	Water	2.47	49	2964
3	DoD System	Acrylic	Water	1.12	45	1904
4	DoD System	Acrylic	Mix 1	2.4	166	2717
5	DoD System	Acrylic	Mix 2	2.1	169	87
6	Dripping	Glass	Water	2.53	46	2884
7	DoD System	Glass	Water	2.63	46	2959
8	DoD System	Glass	Water	1.1	44	1887
9	DoD System	Glass	Mix 1	2.42	162	2662
10	DoD System	Glass	Mix 2	1.98	164	83

3.3 Results and discussion

3.3.1 Tilted plate experiments

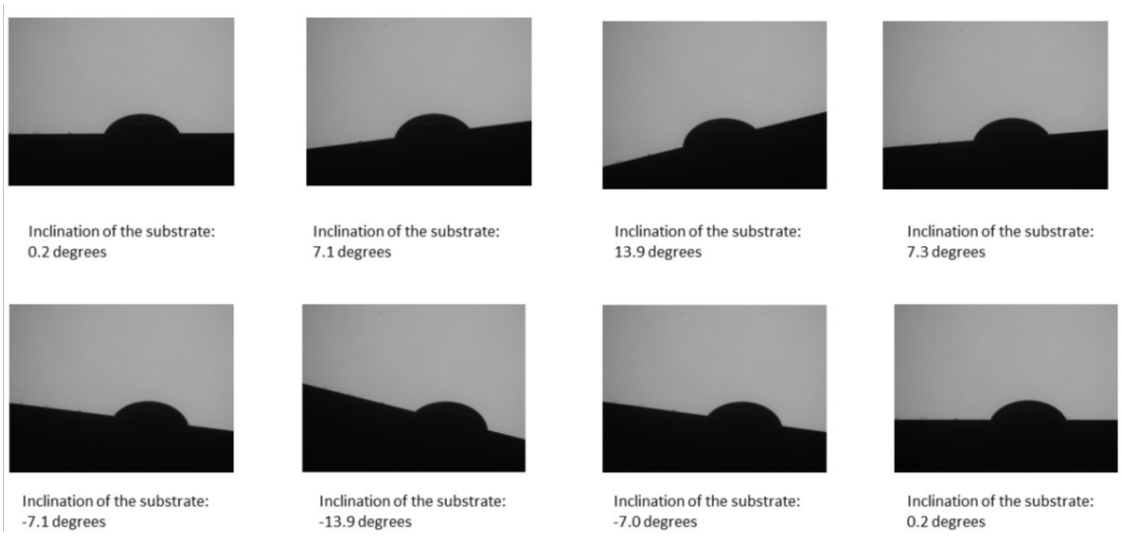

Figure 3.2: High speed imaging of a water-glycerol droplet sitting on the acrylic substrate. The substrate was rotating at an step rate is of 58.74 rad/s.

This section presents the measurements of the contact angle in terms of the inclination angle of the substrate ϕ, and time t. Fig. 3.2 shows examples of experimental images of a droplet on an acrylic substrate, rotated at an step rate of $\omega_1 = 58.74$ rad/s. In this case the right hand equilibrium contact angle is of 56 degrees and its left hand equilibrium contact angle is 58 degrees. This discrepancy is well within the current error on the measurement method, $\pm$ 3 degrees. Under this condition, at the maximum step rate ω_1, the contact angle shows a linear relationship with the

inclination of the substrate (Fig. 3.3 top left corner). Other tilting speeds show a similar behaviour, the results for the other two tilting speeds, 0.04 rad/s and 0.02 rad/s, are shown in Fig. 3.3. A very important difference is seen in the codomain in which the results live. Finally, the data at slow tilting speeds shows less dispersion, probably because the droplets vibrate less as they move. Image analysis allows to analyse the contact angle in terms of time as the substrate rotates. The rotation of the substrate starts in the anticlockwise direction so the left contact angle increases until it reaches a maximum value, then starts to decrease as the rotation changes its direction, increasing again as the substrate returns to its initial position. However, the contact angle does not return to its initial value regardless of the speed of rotation. This can be explained given that a droplet can be in meta-stable states that change when the droplet vibrates [13]. Moreover, in the case of the step rate of 0.02 rad/s, the difference in initial and final angles can be due to droplet evaporation. Indeed, it has been found that the contact angle of an evaporating droplet decreases with time [120].

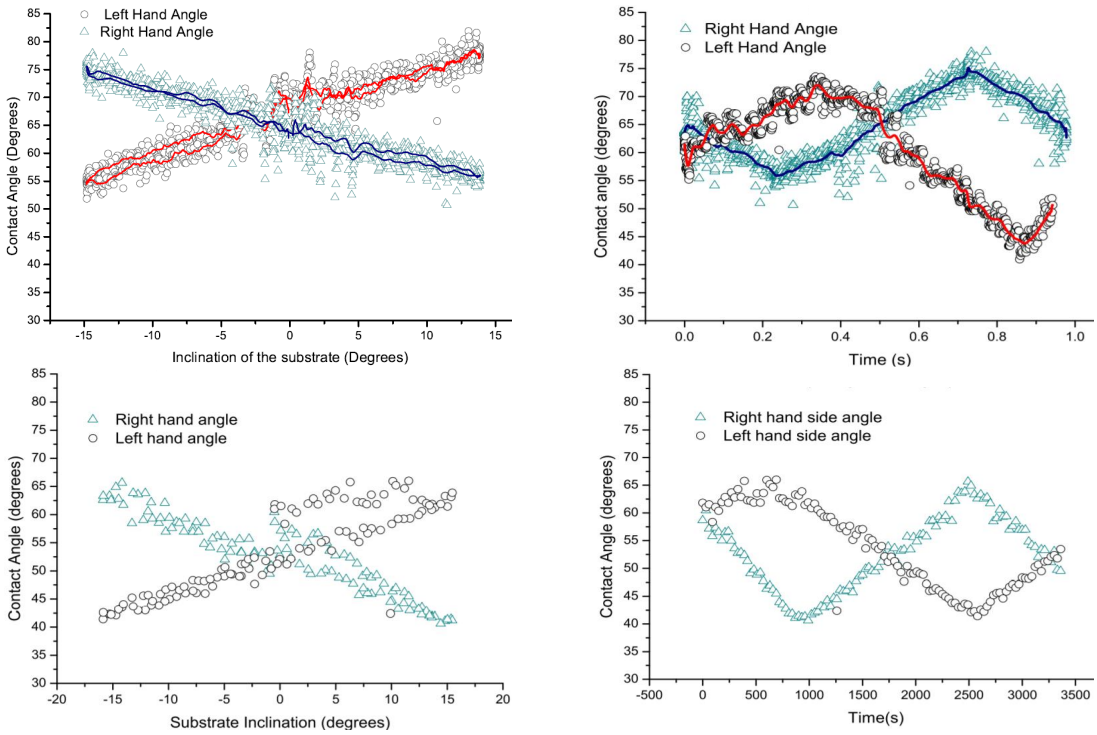

Figure 3.3: Contact angle in terms of substrate inclination (left) and time (right) for a droplet resting on acrylic. The step rates are 58.74 rad/s (top) and 0.02 rad/s (bottom). The triangles and circles are the experimental data for the right hand and left hand angles respectively. The navy blue line is the average of 10 the points for the right hand angle and the red line is the average of 10 the points for the left hand angle.

The glass substrate presents smaller contact angles than the acrylic. For glass, ϕ_{max} = 4 degrees and ϕ_{min} = -4 degrees. Both, the right-hand and the left-hand equilibrium contact angles were found to be of 11 degrees. For the step rate ω_1, the maximum variation of the contact angle was of 10 degrees; demonstrating that drop vibrations during movement affect the contact angle measurement. The data at other step rates is consistent with this hypothesis; slower tilting speeds show less data scattering. At fast tilting rates, the droplet cannot reach a state of equilibrium so hysteresis is observed at all inclination angles. This result is also observed on Fig. 3.4 where the contact angle is in terms of time.

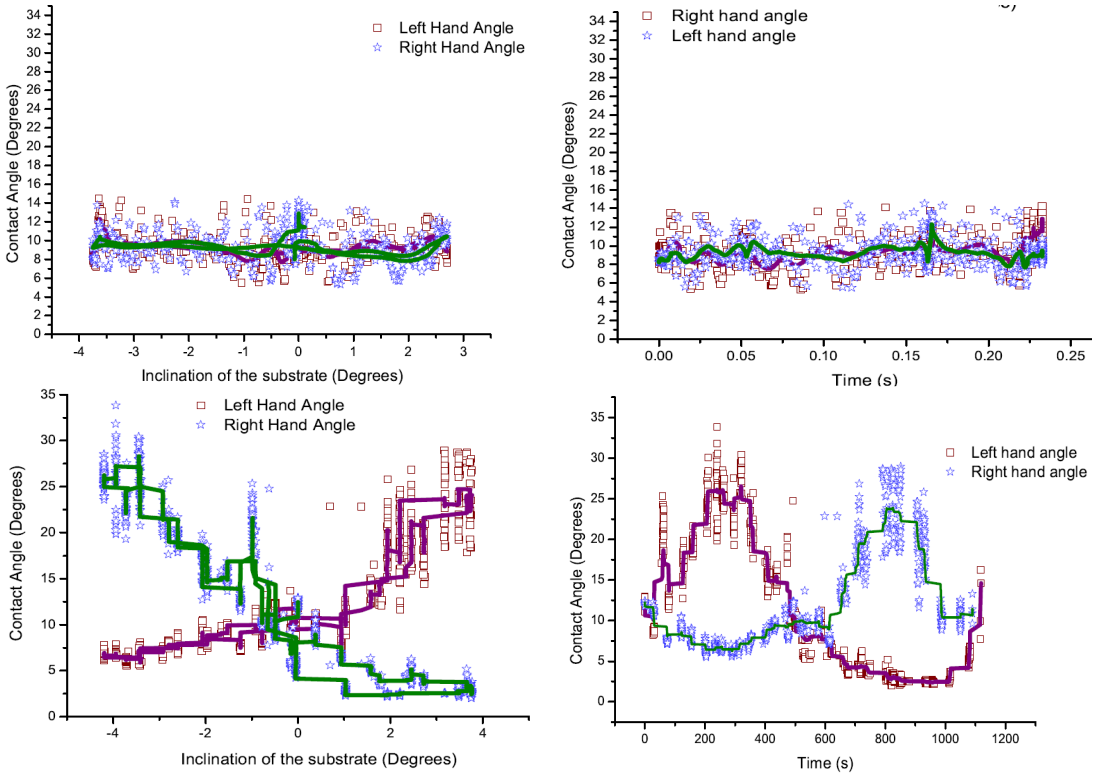

Figure 3.4: Contact angle in terms of substrate inclination (left) and time (right) for a water droplet on glass at an step rate of 58.74 rad/s (top) and 0.02 rad/s (bottom). The triangles and circles are the experimental data for the right hand and left hand angles respectively. The navy blue line is the average of 10 the points for the left hand angle and the red line is the average of 10 the points for the right hand angle.

In conclusion, we show that the contact angle varies with the substrate inclination, with the advancing (receding) contact angle increasing (decreasing) with the inclination. for pinned droplets on hydrophilic substrates. Furthermore, after moving the substrate one cycle the contact angle of the droplet differs from its original one due to the substrate hysteresis. The next section studies the dynamic contact

angle of spreading droplets upon impact onto hydrophilic substrates.

3.3.2 Impact experiments

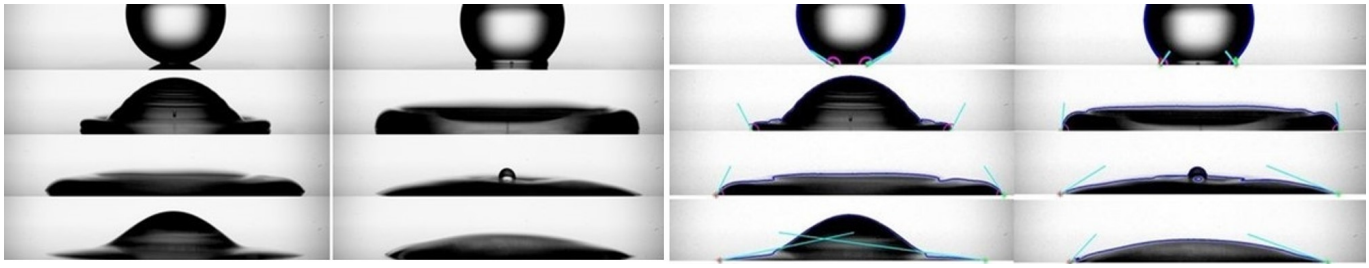

Figure 3.5: Left, experimental images of a water droplet spreading on a glass substrate. Right, MATLAB processed images. The impact speed of this experiments is of 1.01 m/s

Figure 3.5 shows a sequence of images of a water drop impacting on an acrylic substrate and the first spreading and receding phases. In the hydrophilic surfaces studied here, i.e. glass and acrylic, the receding is negligible. Figure 3.6 shows the contact angle dynamics in terms of contact line velocity u_{cl}. As described in previous papers, at the first instants after impact, the contact angle is near 180 degrees. At these early times, $t < 0.56$ ms, the drop is greatly deformed near the contact line while its top part remains spherical. Here, the contact line velocity can move at up to 15 m/s, decreasing rapidly as the contact angle goes from 180 degrees to a local minimum. Afterwards, the contact angle increases and reaches an asymptotic contact angle at a contact line velocity of approximately $u_{cl} \approx 3$ m/s. Eventually the contact angle reaches its minimum at $u_{cl} = 0$ m/s. It has been found that for impact speeds of ~ 1.25 m/s the air layer ruptures at 14 μs and our time resolution is ~ 40 μs [121]. Consequently, we expect the contact angle measurement to be unaffected by the air layer between the droplet and the substrate.

Figure 3.7 shows the spreading diameter $d(t)$ for all the experiments performed for this work in terms of the dimensionless time $t^* = tU_0/D_0$ (inertial time) from impact. For the substrates and liquids used in these experiments, the substrate wettability does not significantly affect spreading until the maximum spreading diameter d_m is reached. As expected, wettability only comes into play at later times [48]. We note that this contrasts with the results of de Goede et al. 2019 [122], where at low impact speeds wettability affects the maximum spreading diameter.

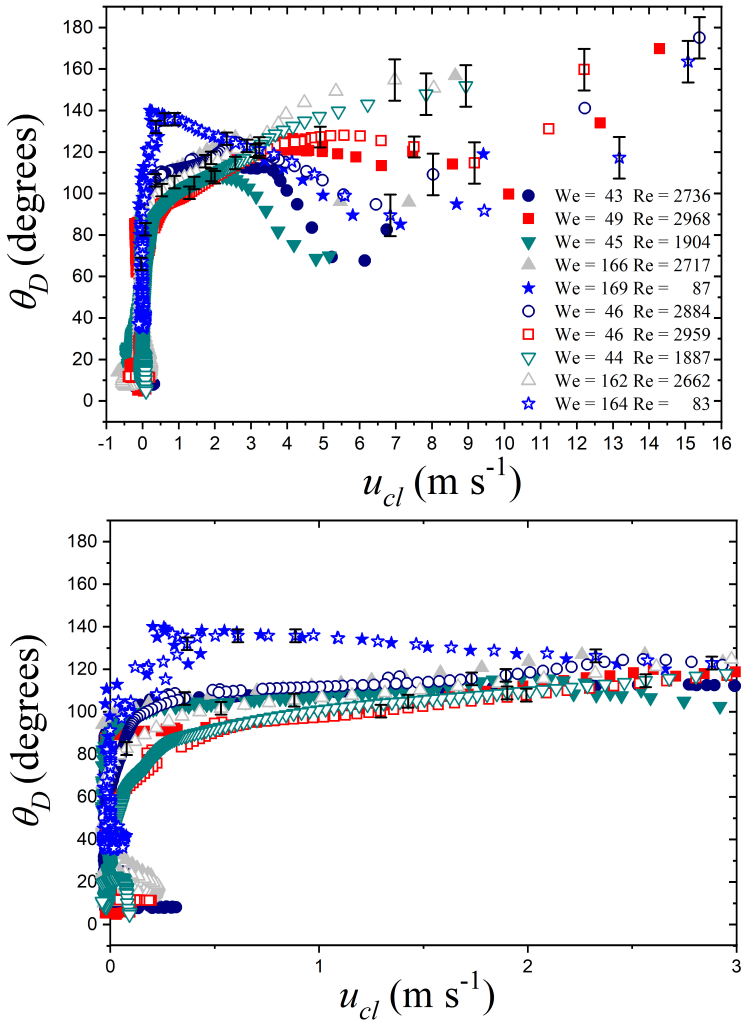

Figure 3.6: Contact angle of a water drop impacting onto acrylic and glass substrates at different We and Re numbers. Here, the contact angle is shown in terms of the contact line velocity. Hollow symbols represent experiments done in glass and solid symbols represent experiments done in acrylic. On the bottom there is a zoom to the the dynamic contact angle for the contact line velocity range from 0 to 3 m/s

This seemingly discrepancy is solved by the fact that the difference in the contact angles between the acrylic and glass are smaller ($\sim$ 45 degrees), than the glass and steel used in de Goede et al. (2019) ($\sim$ 70 degrees). Moreover, as impact velocity increases, influence of the wettability on d_m decreases [28, 123].

Experiments show that both the We and Re numbers affect d_m. Indeed, experiments 5 and 10 have the same We number as experiments 4 and 9, but their Re number is approximately a quarter. The maximum spreading diameter is almost 50% smaller for the former experiments. This difference can be also observed in the contact angle dynamics. The dynamic contact angle in experiments 5 and 10, reaches a local maximum near $u_{cl} = 0$ m/s, while for the rest of the experiments

the contact angle acquires an "asymptotic" contact angle at a contact line velocity of ≈ 3 m/s (Fig. 3.6). As highlighted in previous works, the dynamic contact angle quantifies the interplay between inertia, capillary and viscous forces and the greater the capillary and viscous forces the greater the contact angle [41, 42]. Consequently, for hydrophilic substrates, at a given We number, the larger the maximum dynamic contact angle at $u_{cl} = 0$ the smaller d_m. This is in accordance with previous works where d_m could be predicted through the dynamic contact angle at d_m [27, 28].

The influence of D_0 on d_m is not evident when comparing experiments 2 with 3, and 7 with 8 (table 3.2), where the We number is the same in all the experiments but D_0 is different. In experiments 3 and 8, $D_0 = 1.1$ mm, in contrast, in experiments 2 and 7, $D_0 = 2.47$ mm and $D_0 = 2.63$ mm respectively. As seen, D_0 does not seem to affect the d_m, even when the Re number is 35 % smaller for experiments 3 and 8. Using micrometric drops Visser et al. in 2000, showed that the droplet size has no influence on d_m as long as the same We and Re are used [54]. In contrast, another study on the impact of drops with diameters ranging from 10^{-3}mm to 5 mm studies found that d_m is influenced by D_0 [58]. Here it is noted that for the same liquid, there is a unique radius for a given Weber and Reynolds number combination, therefore the droplet radius could play a role on d_m. However, our results on the influence of D_0 on d_m are not conclusive and a parametric study is required.

Disagreement exists in the way the spreading diameter is defined, with two competing definitions: *i*) the distance between pinning points (the contact line diameter) and *ii*) that corresponding to the maximum distance between any two points on the droplet profile. These different definitions arise from the physical modelling of spreading. Lee et al. in 2016 argued that a scaling of the form $d \propto We^{\alpha}$ is not physically correct as it incorrectly leads to $U_0 = 0$ at the point of impact ($d_m = 0$) [27]. Lee et al. pointed out that this is physically inconsistent because $d_m \geq 1$ even for a near-rest deposition [27]. However, for a *perfect* superhydrophobic surface, if d_m is taken as the contact line diameter, then $d_m = 0$ at the contact point. Moreover, for all the hydrophobic substrates $d_m < 1$ for $U_0 = 0$. As argued by de Goede, et al., d_m depends on the wettability of the substrate at zero impact velocity [122].

However if d_m is not defined at the contact line but defined as the largest distance between two liquid points, then $d_m \geq 1$ always. We note that for impact velocities explored in this paper the difference between taking the two definitions is within the experimental error.

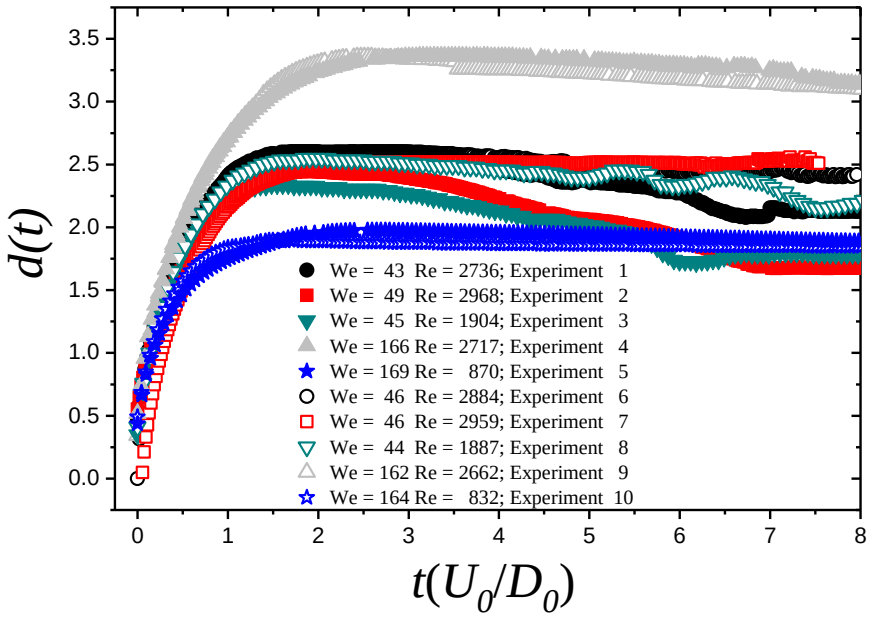

Figure 3.7: Spreading factor $d(t)$ in terms of the dimensionless time. Hollow symbols represent experiments done in glass and filled symbols represent experiments done in acrylic.

Based on these observations and those by Laan et al. (2014) using the Padé approximant $d_m Re^{-1/5} = \frac{P^{1/2}}{1.24+P^{1/2}}$, where $P = WeRe^{-2/5}$ [52]. In figure 3.8, we show the agreement between the data and this scaling. Regarding the influence of the droplet size D_0 on the spreading factor d_m, we see this effect in experiments 2 and 3, and 7 and 8, where the droplet size does not affect d_m. We clarify, that our results are limited to droplet sizes in the millimetre size range so our observation is in agreement with [54].

3.3.3 Contact Line velocity

The contact line velocity, calculated by differentiating the spreading diameter in terms of time, is a source of error. This is, both the contact line position and the time are given as discrete steps and consequently the associated error can be substantial. In particular, as seen in most past papers, the contact line can move less than a pixel per frame. In this thesis, we used a typical resolution of 6.47 μm

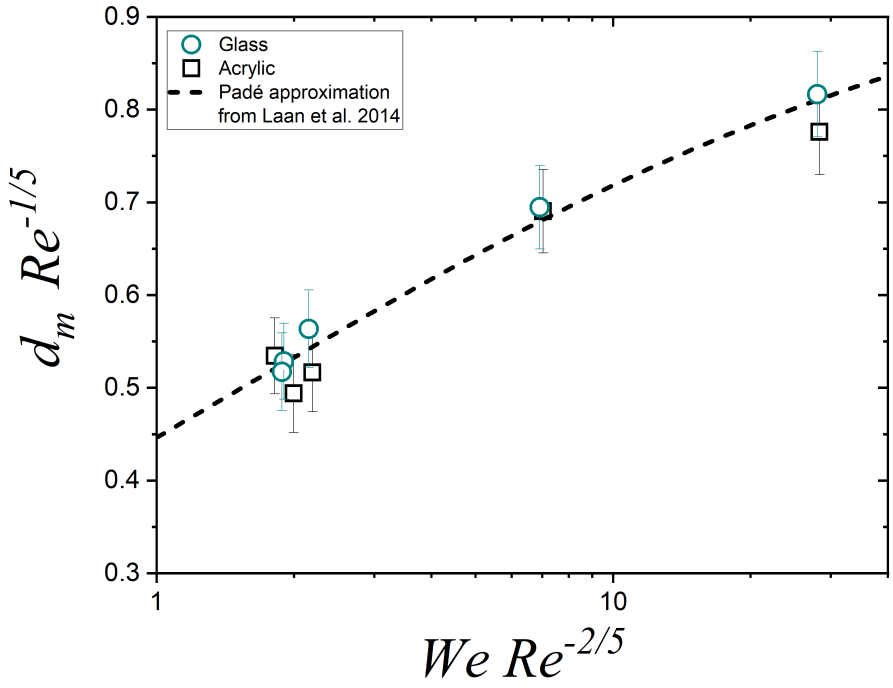

Figure 3.8: Maximum spreading factor in terms of $WeRe^{-2/5}$. The black squares and cyan circles correspond to the impact experiments on acrylic and glass, respectively. In addition, the dashed line shows the Padé approximant $d_m Re^{-1/5} = \frac{P^{1/2}}{1.24+P^{1/2}}$ [52].

per pixel, recording at 23000 fps. Considering an error of $\pm$ 1 pixel in the contact line position, the error in u_{cl} is $\pm$ 0.25 m/s. This associate error is appreciable near maximum spreading, where the hysteresis is expected to be found at 0 m/s. We note that the contact angle in terms of the contact line speed varies rapidly in the range 18 m/s $> u_{cl} >$ 3 m/s. This is the result of large local deformations near the contact, often impossible to resolve within experiments. Moreover, for this range of contact line velocities only a few pictures can be captured as the deceleration occurs in tenths of milliseconds. In the same way the OLS method has an optimal number of points to fit a polynomial, therefore the contact angle measurement depends on both, the spatial resolution of the system and on D_0 [25]. Accordingly, if the resolution is kept constant but D_0 is reduced, then the number of pixels available to fit the droplet profile are reduced and the optimal number of points might not be reached.

3.4 Comparison between the two phenomena

The contact angle obtained from the tilting plate and the impact methods are qualitatively and quantitatively different. The contact angle variation for the impact

experiments is considerably larger than that of the tilting plate experiments. In the former method the contact angle varies from 180 to 0 degrees for all the substrates, in the latter the differences are of only ≈ 30 degrees for all cases. In the impacting case, even at rest in the impacting case, the contact angle varies at least 60 degrees. Moreover, the maximum value of the contact angle obtained in the tilting plate method is always smaller than the asymptotic contact angle. For the receding contact angle, the minimum angle obtained for the tilting plate method is larger than in the impact experiments. We argue that the difference between the two phenomena is due to air and dynamic effects. At impact, there air is entrapped between the droplet and the substrate; this is absent on the tilting plate experiments. The effect of air on droplet impact has been widely discussed in the literature. de Goede et al. (2019), suggest that the droplet skates on air, generating high contact angles seen in experiments [122]. At later times the air layer breaks down and the wetting process begin, leading to a reduction of the dynamic contact angle. In the tilting plate method the contact line is static, and dynamic viscosity effects, e.g. the boundary layer at the spreading lamella and the droplet, are not seen. In contrast, the impact contact line dynamics are influenced the liquid viscosity.

The conclusion is that the underlying physics of the dynamic contact angle differ in both cases. The tilting plate method is a good experiment to characterise the substrate for applications where inertia is negligible. In contrast, for moving contact lines the substrate, should be characterised by studying the dynamic contact angle at impacting conditions.

3.5 Conclusions

This chapter presented dynamic contact angle in two different situations, namely, droplet impact and a moving tilting plate. For the tilting plate experiments the contact angle varied linearly with the angle of the tilting plate ϕ. Moreover, after one cycle the contact angle did not return its initial value due to the surface hysteresis. The impact experiments showed that at a velocity ≈ 3 m/s the dynamic contact angle reaches an *asymptotic* value. No significant difference was found in

d_m between the experiments on Glass and Acrylic, which static contact angles differ in approximately 45 degrees. We attribute this to the experimental error and the "high" velocities used in these experiments. In the next chapter we show that for larger differences in the contact angle d_m is influenced by the wettability.

For the studied conditions, the maximum value of the contact angle for the impact experiments was larger than the one of the tilted plate experiments. In contrast, the minimum receding angle is larger for the tilting plane experiments than for the impact experiments. We argue that the difference between the two phenomena is caused by the entrapped air between the droplet and the substrate (absent in the tilted plane experiments). Therefore, the contact angle dynamics for the tilted plate experiments and the impact experiments are not equivalent.

Additionally, in this chapter, we studied low Weber number droplet impacts on smooth hydrophilic substrates. We concluded that the contact angle dynamics are mostly dependent on the liquid properties. In addition, we found that no receding is observed within this conditions. However, in nature and industry, substrates range from wettable to non-wettable and can have a certain degree of roughness. Next chapter (Chapter 4), focuses on the contact angle dynamics of impacting liquid droplets on substrates with different wettabilities and roughness. Furthermore, it explores a broad range of Weber and Reynolds numbers as to include all the possible outcomes of droplets impacting a solid substrate, i.e. spreading, deposition and splashing.

Chapter 4

Splashing on smooth and rough surfaces with different wettability

This chapter presents a systematic study of liquid droplets impacting on smooth and rough solid substrates. Here, substrate properties range from completely wetting to superhydrophobic. Our results show that the splashing ratio β, the maximum dynamic advancing contact angle, and the mean width of the protruding peaks appropriately parametrises the splashing and no-splashing behaviour.

4.1 Introduction

Chapter 3 focused on the spreading of a droplet on a hydrophilic substrate. In general, substrates used in industrial processes or the ones found in nature are neither hydrophilic nor smooth, but have different wettabilities and surface roughness. This chapter extends the experiments of Chapter 3 by studying the contact angle dynamics on smooth and rough substrates with varying wettabilities. In particular, this chapter presents experiments on the effects of the wettability on the impact dynamics and splashing on smooth and rough surfaces.

To date, there is no accepted consensus on the role of surface wettability on drop splashing. Surface wettability is often characterised by the static apparent contact angle θ_s formed by the intersection of the liquid-solid and the liquid vapour interfaces of a sessile droplet resting on a flat substrate. Past studies have analysed the influence of θ_s on splashing and determined that wettability has no effect on the splashing threshold for high capillary numbers [66, 124]. This is expected as the drop spreads over a thin air film and not along the substrate. Contrasting studies have shown that drop splashing effectively depends on the surface wettability and that hydrophobic substrates exhibit a low-velocity splashing threshold [72, 80, 81]. The influence of the dynamic contact angle (θ_D) on the splashing threshold has also been observed on simulations and found that splashing does not occur for $\theta_{DA} < 90$ degrees [83].

Surface roughness effects on splashing have been studied in terms of various parameters, including the arithmetic amplitude average roughness (R_a), the root-mean-square roughness (R_{rms}), the average peak to peak feature size (R_{pk}) and the surface feature mean width (R_{sm}), defined as the width average of the profile features [62, 66, 86, 84, 87]. In 1998, Range and Feuillebois proposed that splashing was determined by the We number and the ratio between the average surface roughness ratio and the droplet size, i.e. R_a/D_0, [86]. However, Roisman et al. in 2015 argued that the mean average roughness alone does not provide sufficient information of the substrate surface to effectively characterise the splashing threshold [66]. They found that the characteristic slope of the protruding peaks, R_{pk}/R_{sm}, can characterise the

splashing behaviour on rough and porous substrates.

In this chapter, we use high speed imaging to visualise the impact of droplets on smooth substrates and substrates with different roughness and wetting properties to determine the role of the substrate roughness on the impact dynamics. Specially, wettability, described through the dynamic contact angle, is studied in terms of the spreading speed. Our results indicate that the splashing threshold depends on the dynamic contact angle and, therefore, is influenced by the wettability. We conclude by establishing that the splashing behaviour is effectively characterised by three parameters, i.e. the splashing ratio, the feature roughness size ratio, and the maximum dynamic contact angle.

4.2 Experimental Details

The experiments consist of the visualisation by high speed imaging of liquid drops impacting at different speeds on substrates with varying properties. As described in Chapter 2 the system allows the measurement of the dynamic contact angle and the contact line speed. Liquid drops were generated by dripping, and travelled vertically downwards to impact dry solid substrates of different wetting properties. The distance from the needle to the substrate was varied from 0.4 m to 2.0 m to adjust the drop impact velocity (U_0). The speed of impact was varied for all the liquid/substrate sets to obtain conditions that include both simple spreading and splashing. In these experiments U_0 ranges from 1.1 to 4.9 m/s, and the drop diameter (D_0) ranges from 1.8 to 2.5 mm (depending of the liquid). Liquid properties are presented in Table 4.1.

Table 4.1: Fluid properties used throughout the experiments in this section

Fluid	μ (mPa s)	σ (mN/m)	ρ (kg/m^3)
Ethanol	1.04	22.3	789
Water	0.98	70.8	998
Water & Glycerol	4.77	68.5	1,126

The onset of splashing occurred in the range of $U_0 \approx 1.5$ to 1.8 m/s for ethanol and water. Consequently, the dynamic contact angle was measured at $U_0 = 1.01$ m/s

as, at this condition, impacting events result on simple spreading and the contact line is free from instabilities for all the substrates. The dynamic contact angle (θ_D) at each frame was measured with the MATLAB code described in Chapter 2, with the exception of the 120 grit diffuser. As mentioned in Chapter 2, the droplet and substrate profiles are obtained by using a defined intensity threshold for the conversion of a greyscale image to a binary format, using Otsu's method [117]. This method automatically chooses the threshold value that minimises the intraclass variance of the thresholded black and white pixels. However, for the rough substrates, since the surface is not reflecting, the threshold had to be selected manually to avoid any disruption in the detection of the surface. In addition, due to the substrate roughness affecting the contrast in the picture, the contact angles for the 120 grit substrates had to be measured manually with Image J. Splashing events were directly identified from the images, where splashing refers to a droplet breaking and creating at least one secondary droplet. Each experiment was conducted three times in clean surfaces, as any impurity in the surfaces could alter the results.

4.2.1 Smooth Surfaces

The experiments include three liquids, i.e. water, a 4.7 mPa s aqueous glycerol and ethanol, and seven flat solid substrates, i.e. glass, mica, cast acrylic and polytetrafluoroethylene (PTFE, teflon), Glaco and Perfluorodecyl acrylates ($PFAC_6$ and $PFAC_8$) applied to glass. Substrate properties are found in Table 4.2. The roughness of the Perfluorodecyl acrylates, has been found to be in the submicrometer scale (see figure 5.2), therefore we expect that it does affect the splashing behaviour. In addition, surface roughness from Glaco sprayed surfaces was measured with and its average roughness and peak to peak roughness are shown in table 4.4. The details of the roughness measurement are given in the next section. Moreover, to account for the Glaco nanometric roughness and its effects on splashing, the Glaco coated substrates were oxygen plasma treated to make them hydrophilic. It has been found that the roughness of silicon, silicon dioxide, glass and fibers after an oxygen plasma treatment increases in the range of tenths of nanometers [125, 126]. Therefore, we

do not expect a significant effect from the change of roughness coming from the oxygen plasma treatment on splashing (apart from the change on wettablity). The experiments covered the range of $131 < We < 512$ and $0.027 < Ca < 0.217$.

Table 4.2: Equilibrium and dynamic contact angles for the smooth substrates used throughout the experiments. Unless shown, the error on the contact angle measurements is of 2 degrees.

Substrate	θ_s Water	θ_{max} Water	θ_s Ethanol	θ_{max} Ethanol	θ_s Aqueous Glycerol	θ_{max} Aqueous Glycerol
Glass	11±3	109±3	5 ± 4	87 ± 4	11±3	119±3
Mica	31±2	107±3	5 ± 4	87 ± 4	31±2	118±3
Acrylic	56±2	105±3	5 ± 4	87 ± 4	56±2	123±3
Teflon	93±2	113±3	5 ± 4	87 ± 4	93±2	127±3
$PFAC_6$	111±2	122±3	31±4	96±4	111±2	120±3
$PFAC_8$	120±2	131±3	56±4	100±4	120±2	126±3
Glaco	145±2	147±3	5 ± 4	98±4	145±4	147±2

4.2.2 Rough Surfaces

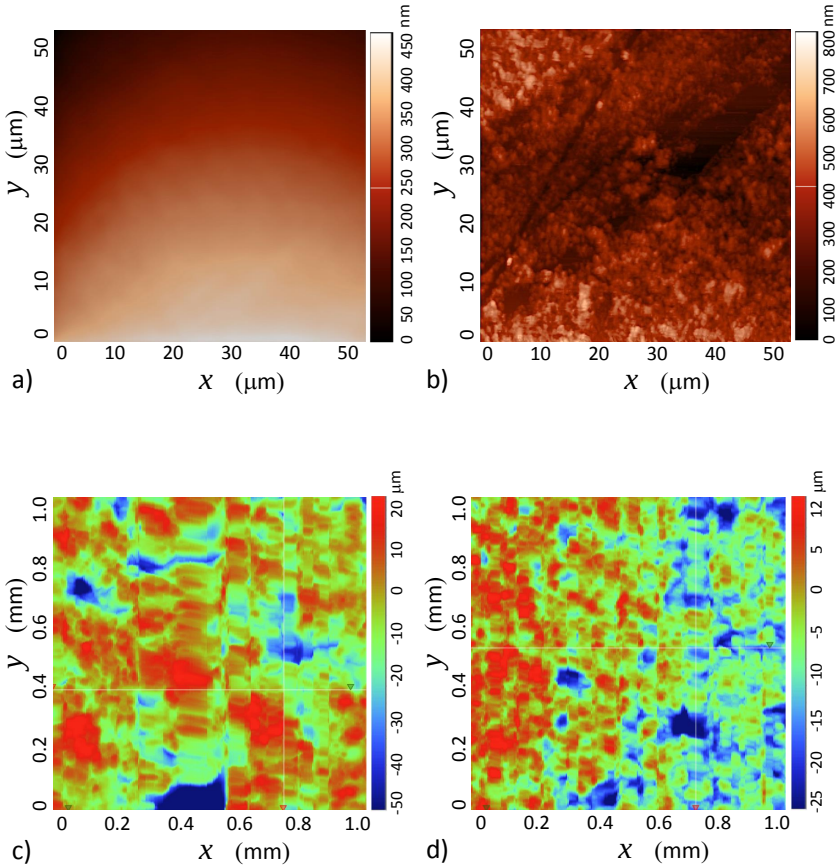

Figure 4.1: Atomic force microscopy of a) smooth glass, and b) Glaco-sprayed on smooth glass. Surface roughness as seen by profilometry for c) 120 grit, and d) 220 grit substrates.

Ethanol and water liquid droplets were impacted on substrates of well-defined roughness. The impacted surfaces were glass diffusers of the same material (NBK-7) with different roughness. The diffussers were acquired from Thorlabs and their substrate wettability was changed by a superhydrophobic spray (Glaco). The roughness of the samples remained unchanged after the Glaco coating, except for the smooth surface. For the smooth and the Glaco covered smooth surfaces, roughness was measured with an Atomic Force Microscope (NT-MDT NTEGRA) used in semi contact mode topography. The scans were conducted at a frequency of 1.01 Hz on 3 different zones of 50 by 50 μm for each sample. Imaging examples are shown in Fig. 4.1. For the rest of the surfaces, surface roughness was measured with a tactile surface profilometer (DektakXT Stylus Profiler) in 3 areas of 1 mm^2 for each sample, taking 5000 data points per scan. Examples of the profiles are shown in Fig.

4.1. Measurements taken from the surface profilometer correspond to the average roughness (R_a), the peak to peak roughness (R_{pk}) and the characteristic width of the surface profile R_{sm}. Substrate properties are presented in Table 4.4. The mean width of the roughness feature of the smooth glass is reported as $R_{sm} > 50$ μm, as this value corresponds to the size of the AFM sample size (no features were found within). The measurements of the static advancing and receding contact angles were done following the method developed by Kwok et. al. in 1996 [127]. This is, through a syringe tip, an infuse/withdraw syringe pump (Harvard Apparatus PHD 4400) expands or contracts a droplet over a substrate at a rate of 12 μl/min. The process was recorded at 200 fps with the same spatial resolution as the impacting experiments (see Chapter 2). Results are shown in Table 4.3.

Table 4.3: Dynamic contact angles for the substrates used throughout the experiments

Substrate	θ_{max} Water	θ_a Water	θ_r Water	θ_{max} Ethanol	θ_a Ethanol	θ_r Ethanol
Smooth Glass	101 ± 3	92 ± 3	70± 3	97 ± 5	20 ± 3	0 ± 3
1500 Grit	112 ± 3	89 ± 3	26 ± 3	97 ± 5	11 ± 3	0 ± 3
600 Grit	113 ± 3	-	-	97 ± 5	-	-
220 Grit	120 ± 5	95 ± 3	22 ± 3	101 ± 5	9 ± 3	0 ± 3
120 Grit	129 ± 5	98 ± 3	27 ± 3	107 ± 5	8 ± 3	0 ± 3
Glaco Glass	149 ± 3	161 ± 3	158 ± 3	-	-	-
Glaco 1500 Grit	149 ± 3	161 ± 3	159 ± 3	-	-	-
Glaco 220 Grit	150 ± 5	160 ± 3	156 ± 3	-	-	
Glaco 120 Grit	150 ± 5	158 ± 3	156 ± 3	-	-	-

Table 4.4: Surface roughness for the substrates used throughout the experiments

Substrate	R_a (μm)	R_{pk} (μm)	R_{sm} (μm)
Smooth Glass	0.017	0.04	> 50
1500 Grit	1.021	2.39	40.32
600 Grit	1.028	2.48	41.99
220 Grit	3.507	11.65	152.03
120 Grit	5.743	20.02	168.49
Glaco Glass	0.422	0.82	25.58
Glaco 1500 Grit	1.064	2.41	40.47
Glaco 220 Grit	3.618	11.43	151.95
Glaco 120 Grit	5.807	20.08	168.27

4.3 Results and discussion

4.3.1 Contact Angle Dynamics on smooth surfaces

Figure 4.2 shows the dynamic contact angle θ_D of water drops impacting on glass and Glaco at various times. Figure 4.3 presents the value of the contact angle in terms of the contact line speed for three liquid/substrate systems, and Fig. 4.4 shows the dynamic contact angle for various liquids impacting a *wettable* substrate. In particular, Fig. 4.3 shows the three contrasting *different* contact line dynamics, i.e. hydrophilic (ethanol on glass), hydrophobic (water on $PFAC_8$), and superhydrophobic (aqueous glycerol on Glaco) dynamics. As expected, no receding is observed under hydrophilic conditions, the contact line remains pinned at the maximum spreading diameter, and the maximum dynamic contact angle remains ≤ 87 degrees. For hydrophobic substrates a clear hysteresis is observed where advancing (θ_{DA}) and receding (θ_{DR}) angles rapidly achieve their asymptotic values. This characteristic curve has been observed and validated by numerical modelling [41]. In addition, our results demonstrate that superhydrophobic substrates do not show a large angle variation, remaining at $\theta_D \geq 140$ degrees during the advancing and most of the receding phases (Fig. 4.3), only to vary just when the droplet is about to bounce ($u_{cl} \approx -0.25$ m/s). According to past works, a low variation of the contact angle on superhydrophobic substrates is a characteristic that a surface needs to achieve to be considered superhydrophobic [49, 56]. Here, for future analysis, we define θ_{max} as the advancing asymptotic value of θ_{DA}. At these timescales, there are no large surface deformations, and the contact angle can be measured precisely. Previous research has found that θ_D at maximum spreading is independent in the range of $0.2 < U_0 < 2.1$ m/s [28]. Here we argue that θ_{max} is dependent on the contact line velocity u_{cl}, but independent of U_0 for U_0 leading to smooth spreading. In addition, U_0 has to be large enough so the air film ruptures at an early time and the wetting is effectively measured by θ_{max}. Previous research has found that the air film ruptures at a time $t = 14$ μs at an impact velocity of ~ 1.25 m/s. As the temporal resolution of our system is 40 μs and $U_0 = 1.01$ m/s, the air layer does not influ-

ence θ_{max} measurement. *Dynamic* hydrophobicity is observed on all the conditions studied here, i.e. all the systems advance with a contact angle $\theta_{max} \geq 87$ degrees during the instants following impact. In fact, as observed in Fig. 4.5 and Table 4.2, all our liquid/substrate configurations presented a dynamic advancing contact angle greater than 87 degrees regardless of the value of the equilibrium/static contact angle. The extreme case is ethanol on glass where the contact angle is 5 degrees at rest (equilibrium) but advances at 87 degrees. This advancing hydrophobicity on hydrophilic substrates is in agreement with previous reports[28, 42], and it has been argued that is characterised by the droplet liquid surface tension and viscosity, and the air between the droplet and the substrate. Moreover, Figs. 4.4 and 4.5 demonstrate that two liquids/substrate systems with the same equilibrium contact angle (θ_s) can have two different dynamic contact angle history. Ethanol on Glaco and ethanol on glass show the same equilibrium (static) contact angle, $\theta_s \approx 5$ degrees, yet their asymptotic dynamic values differs significantly, i.e. 98 and 87 degrees respectively. Fig. 4.5 shows no direct relation between θ_s and θ_{max}, i.e. the dynamic angles are not correlated for each liquid/solid combination. However it is seen is that for hydrophilic substrates, θ_{max} of the aqueous glycerol is significantly larger than θ_{max} on for water, even when the two systems have the same θ_s. This can be attributed to the viscous dissipation on the contact line. In the case of hydrophobic substrates, we see that θ_{max} is similar when $\theta_s \geq 110$, this is because liquids on hydrophobic substrates liquids tend to be more mobile and they are in less contact with the solid. Therefore viscous dissipation is negligible and surface tension forces and inertia dominate the behaviour.

4.3.2 Splashing on smooth substrates

Figures 4.6 and 4.7 show the impact behaviour of water and ethanol drops on different substrates at various We numbers. The effect of wettability is clearly observed here, and our results are consistent with previous observations [72, 80, 124], splashing is favoured by increasing impact speed and increasing maximum advancing contact angles θ_{max}. Ethanol droplets at an impact velocity of $We = 258$ ($\theta_{max} = 86$) show

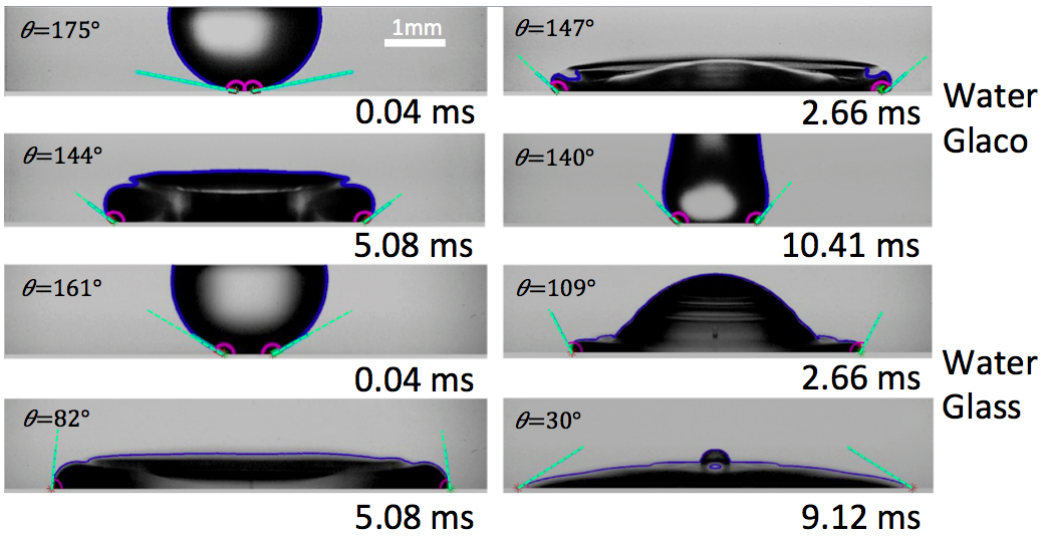

Figure 4.2: Image analysis for spreading water droplets after impact on glass and glaco at 0.98 m/s. The water spreads with a greater contact angle for glaco as compared to the spreading on glass.

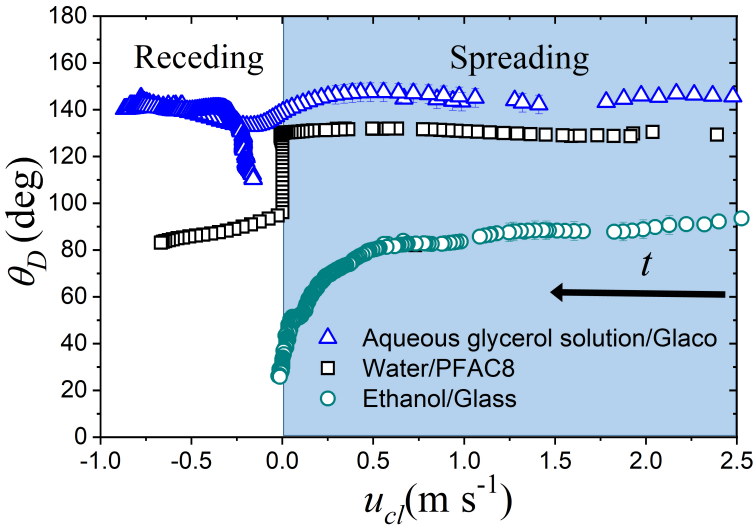

Figure 4.3: The dynamic contact angle θ_D in terms of the contact line velocity. Here, we show the three major wetting behaviours, i.e. superhydrophobic (glycerol & water on Glaco), hydrophobic (water on $PFAC_8$) and wetting (ethanol on glass).

no splashing on the glass substrate but prompt splashing on Glaco ($\theta_{max} = 98$) (Fig. 4.6). In contrast, water droplets impacting on Glaco show (prompt) splashing at a slower speed, $U_0 = 2.19$ m/s ($We = 156$, $\theta_{max} = 147$) at a point where the droplet has reached its maximum spreading diameter (Fig. 4.6). For water impacting on PFAC8 at 2.34 m/s (We=189, $\theta_{max} = 131$), fingering of the lamella is observed but no splashing (Fig. 4.6). We explain these observations by contrasting the dynamic contact angle history of these systems, i.e. it is easier to splash droplets on sur-

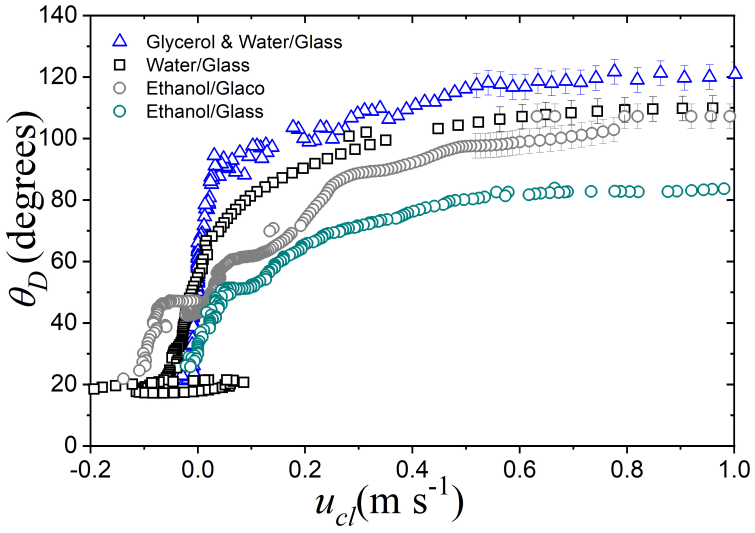

Figure 4.4: The dynamic contact angle θ_D in terms of the contact line velocity for different liquids impacting "wettable" solids, here $\theta_s \approx 10$.

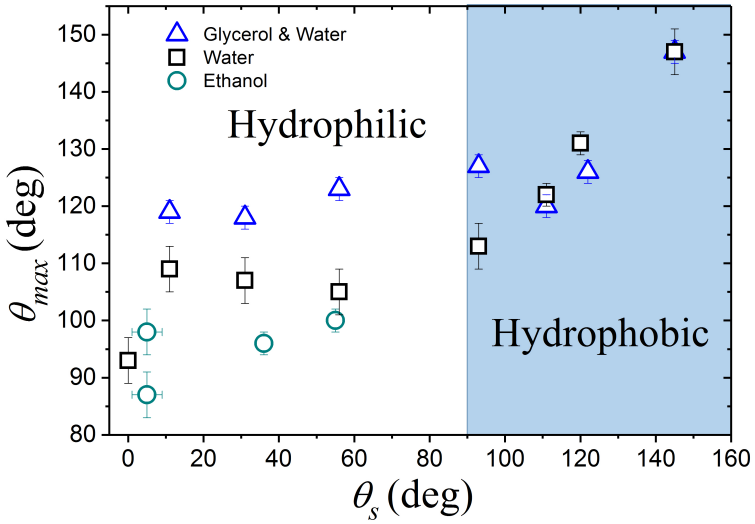

Figure 4.5: The dynamic contact angle θ_{max} in terms of the static contact angle θ_s. For all of the liquids and substrates $\theta_{max} \geq 85$ degrees regardless θ_s.

faces with a higher maximum advancing contact angle. In addition, the transition between corona to prompt splash is observed for increasing impact velocities. Fig. 4.6 shows impact prompt splashing of water on Glaco at $U_0 = 2.19$ m/s and Fig. 4.7 shows corona splashing at $U_0 = 4.4$ m/s. The transition from prompt to corona splashing is studied in more detail in section 4.3.3.

An interesting phenomenon seen during these experiments is that the lifted lamella breaks at a longer time on the water impact on superhydrophobic substrates than on the ethanol impacting on glass substrates. Our theory is that the lamella

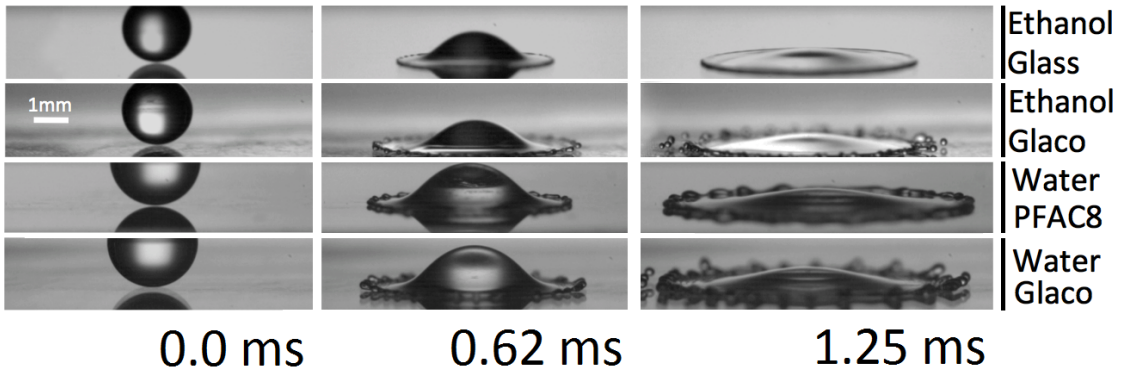

Figure 4.6: Impact behaviour for ethanol and water droplets. Here, We = 258 for ethanol on glass and We = 250 on Glaco, We = 167 for water impacting on Glaco, and We = 189 for water on $PFAC_8$. Splashing is observed on Glaco, but no splashing is observed for ethanol on glass and for water on PFAC8.

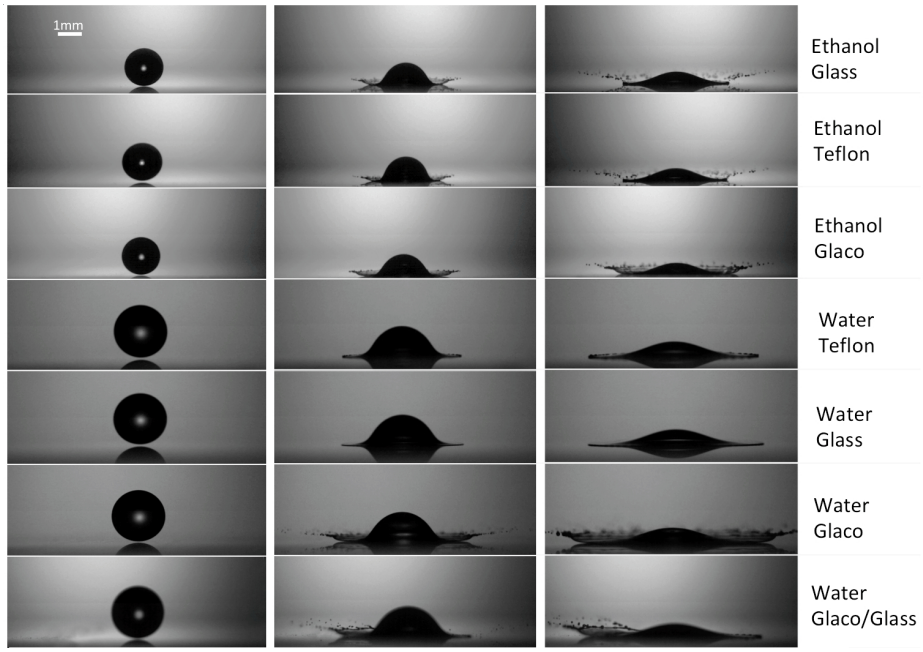

Figure 4.7: Impact behavior for ethanol (We = 571) and water (We = 462) droplets on different substrates. Splashing is observed for ethanol on all substrates. In contrast, water presents splashing on Glaco, microsplashing for Teflon [128], and no splashing for glass. The bottom set of images shows the impact of a droplet on a glass substrate whose left side has been coated with Glaco; the left side of the droplet rapidly splashes while the right side spreads.

glides over the superhydrophobic substrates, but *sticks* on wettable substrates causing its breakup. For water impacting at 4.4 m/s on the Glaco-coated surface, the lamella touches the substrate 7.78 ms after impact. For an ethanol droplet impacting the Glaco coated surface at the same speed, the lamella touches again the substrate after 1.17 ms. In fact, for the water impacting the superhydrophobic substrate, the lamella can be seen gliding above the surface without breaking up. The lamella

then spreads and recedes over the substrate, following a conventional receding process. A further study in this regime with omniphobic substrates to characterise the substrate wettability and the role of the liquid surface tension, would be of interest.

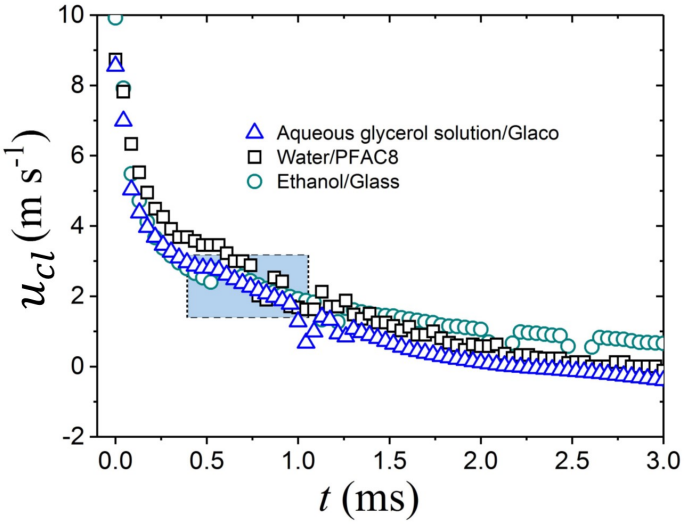

Figure 4.8: Contact line speed for spreading droplets in terms of the time from impact. Here, the impact velocity for water and the aqueous solution droplets is of 1.34 m/s, while for the ethanol drop is of 0.98 m/s. The highlighted area shows the time domain where the lifting of the lamella occurs for splashing cases.

Our experimental observations indicate that the lifting of the lamella and splashing occur in the time range between 0.4 to 1.2 ms after impact. In the same time scale, for spreading droplets, contact line velocities are found in the range of 1.0 to 2.5 m/s, results are shown in Fig. 4.8. Consequently, we expect wettability to be important in the timescale of hundreds of microseconds and at contact lines in the range of 1.0 to 2.5 m/s.

However, the two dimensionless groups traditionally used to describe splashing do not contain wettability effects; these are the capillary number, Ca, and the splashing parameter, $K = We^{1/2}Re^{1/4}$, [69, 68]. Accordingly, Fig. 4.9 presents the splashing behaviour in terms of these groups and both the static contact angle (θ_s), and the maximum advancing contact angle (θ_{max}). Previous experiments with ethanol drops impacting aluminium (wettable) placed the splashing threshold at $K = 127$. As seen, our results are consistent with this finding as ethanol droplets splash on hydrophilic substrates at $K > 120$ [129]. However, both groups (Ca and K) fail to separate the overall splashing behaviour for all the other liquids; the data is clustered by liquid,

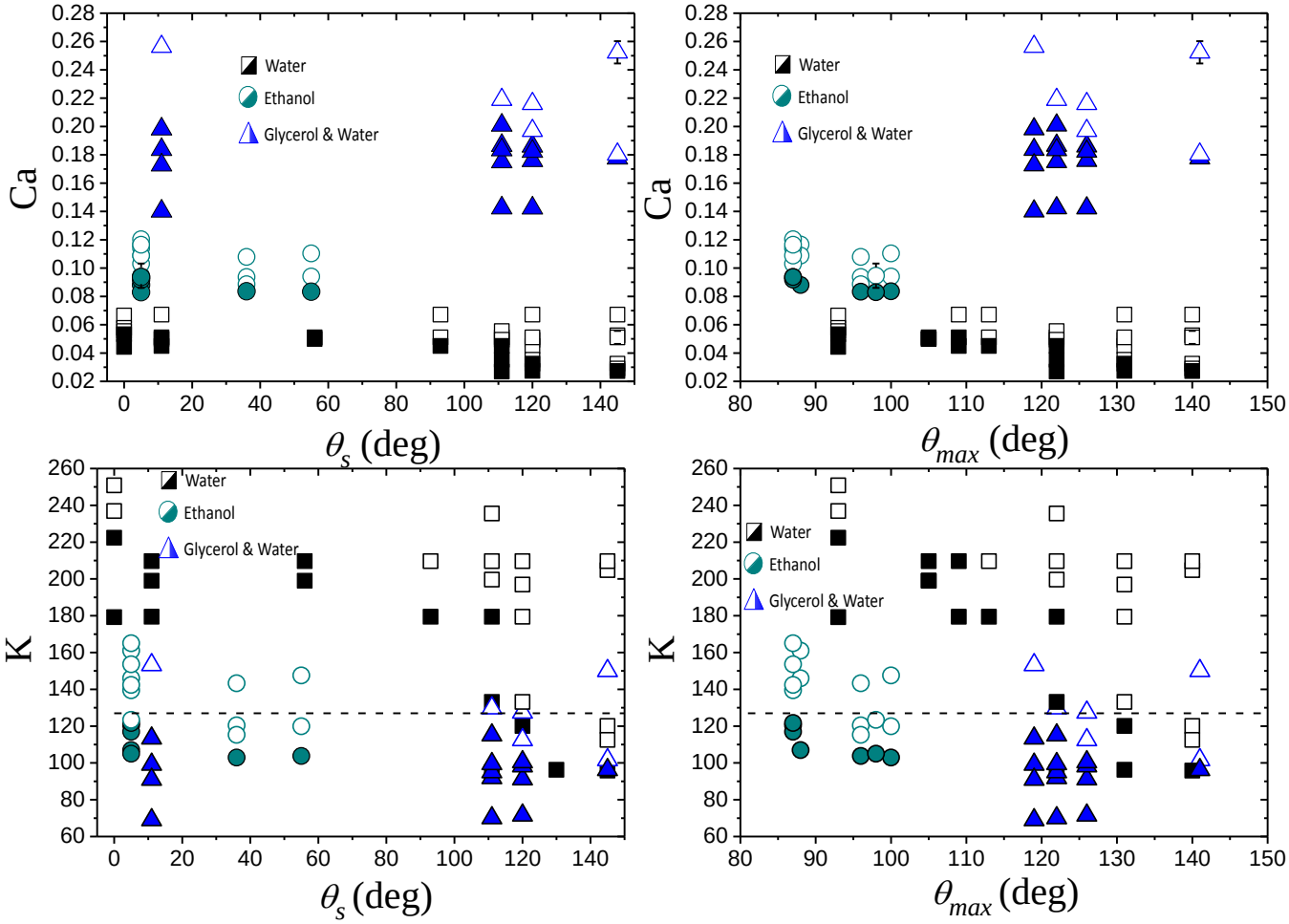

Figure 4.9: Impact behaviour in terms of the capillary Ca and the splashing K parameter as a function of both the static θ_s and the maximum dynamic contact angles θ_{max}. Open symbols represent splashing and solid symbols no splashing. A good behaviour divide "by liquid" is seen but is not consistent across all the fluids. The dotted line indicates the splashing threshold for ethanol drops, K > 127, found by Bird et al. in 2009 [129].

and within these clusters the results show that large contact angles and high Ca numbers promote splashing. Within clusters, the effect of wettability on splashing is progressively visible as the contact angle (static or dynamic) increases. An overall conclusion is that any dependence of splashing on wettability is only visible for Ca < 0.22 and this evidence places our results in agreement with past works suggesting splashing is independent of wettability at high capillary numbers (Ca > 0.26), or on hydrophilic substrates, i.e. $\theta_s < 90$ or $\theta_{max} < 113$ degrees [124].

Recent works have described the splashing velocity of drops impacting smooth mostly *hydrophilic* surfaces at low Ohnesorge numbers ($Oh = Ca/We^{1/2}$), by numerically solving the momentum balance equation and estimating the aerodynamics lifting forces [65, 130]. This model parts from the potential flow theory, where an inviscid and incompressible flow is considered. Gordillo and Riboux in 2014, found

that the liquid must separate from the solid and avoid further wetting to produce a splash. Therefore, splashing is attributed to a lift force in the lamella. This lift force has two components, the gas lubrication force ($\approx k_l \mu_g V_t$) exerted beneath the lamella and the suction force ($\approx k_u \rho_g V_t^2 H_t$) induced at the top of it, here k_l and k_u are constants to be determined, μ_g and ρ_g are the gas viscosity and density and V_t and H_t are the velocity and height of the lamella. This way, splashing can be described using the momentum balance Eq. [65]

$$\frac{\sqrt{3}}{2} Re^{-1} t_e^{-1/2} + Re^{-2} Oh^{-2} = 1.21 t_e^{3/2} \tag{4.1}$$

where t_e is the ejection time of the lamella. The momentum equation is then solved numerically to find t_e. Using the numerically calculated ejection time, $V_t = \frac{\sqrt{3}}{2} U_0 t_e^{1/2}$ and $H_t = \frac{\sqrt{12}}{2\pi} D_0 t_e^{3/2}$, and k_l can be calculated from the lamella thickness, the mean free path of the gas molecules λ_g and the wedge angle α (angle between the substrate and the lifted liquid sheet), this is,

$$k_l = -\frac{6}{tan^2\alpha} \left[ln\left(19.2 \frac{\lambda_g}{H_t}\right) - ln\left(1 + 19.2 \frac{\lambda_g}{H_t}\right) \right]. \tag{4.2}$$

Numerical results show that $k_u \approx 0.3$, as calculated by Riboux & Gordillo in 2014 [65]. Finally, one can define a parameter, the splashing ratio, that compares the aerodynamic forces with the surface tension forces as,

$$\beta = \left(\frac{k_l \mu_g V_t + k_u \rho_g V_t^2 H_t}{2\sigma} \right)^{1/2}. \tag{4.3}$$

For low viscosity liquids and at atmospheric pressure the lubrication force dominates and $t_e = 0.88 We^{-2/3}$, $V_t = 1.07 \frac{\sqrt{3}}{2} U_{sp} We^{1/3}$ and $H_t = 0.83 \frac{\sqrt{3}}{\pi} D_0 We^{-1}$, where U_{sp} is the splashing impact velocity. A simple approximation using experimental values of the diameter of the droplet and a typical splashing velocity [131], $H_t \approx 10^{-6}$, then $k_l \approx -\frac{6}{tan^2\alpha} ln\left(19.2 \frac{\lambda}{H_t}\right) \approx \frac{10.69}{tan^2\alpha}$. Therefore, the approximation of the splashing ratio for low viscosity liquids impacting at atmospheric pressure is,

$$\beta \approx 2.22 \frac{1}{\tan(\alpha)} \frac{\mu_g^{1/2} (\rho D U_{sp}^5)^{1/6}}{\sigma^{2/3}}. \tag{4.4}$$

Equation 4.4 is independent from viscosity but we expect viscosity to play a significant role in splashing [62, 71]. Our premise is that viscosity influences the dynamic contact angle as seen in Fig. 4.5. In fact, the maximum dynamic contact angle is larger for the aqueous glycerol mixture than for pure water. Given that the surface tension of these to liquids is very similar (smaller for the aqueous glycerol mixture), we attribute this difference to the viscosity.

Past works have found that α remains constant at ≈ 60 degrees, obtaining a value of $\beta \approx 0.11 - 0.14$, [130]. Our hypothesis is that splashing over hydrophobic and superhydrophobic smooth substrates can be described as a function of β and the maximum advancing angle θ_{max}. Figure 4.10 shows our results when parametrised by β in terms of θ_{max}, here α has been taken as 60 degrees, and the impact speed U_0 has replaced U_{sp}. As seen in Fig. 4.10, the splashing behaviour is effectively divided for all the different liquids impacting on to all the different solids. Moreover, for wettable substrates ($\theta_{max} < 103$), the data is in agreement with past experiments and simulations (dashed line in Fig. 4.10) [65, 130]. The deviation from the current model (dashed line) only occurs when $\theta_{max} > 105$, where the splashing dependency on wettability becomes apparent for hydrophobic substrates. These results confirm that splashing is dependent on the dynamic wettability of the system. Furthermore, by just measuring $theta_{max}$, and knowing the liquid and gas properties the splashing threshold can be calculated.

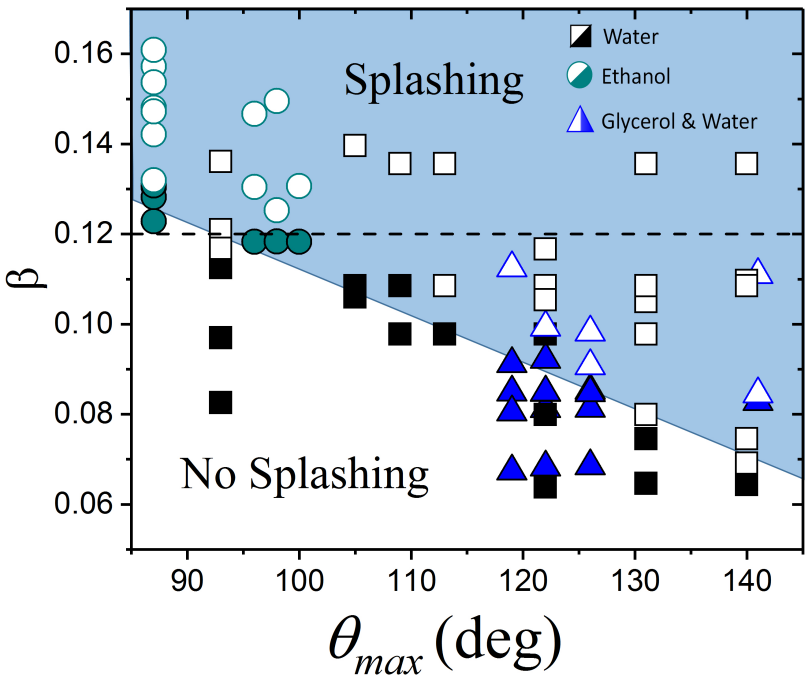

Figure 4.10: Splashing in terms of θ_{max} and β. Open symbols represent splashing while solid ones stand for no splashing. The dashed line is from de Goede et. al (2017) [130].

4.3.3 Contact Line Dynamics on rough substrates

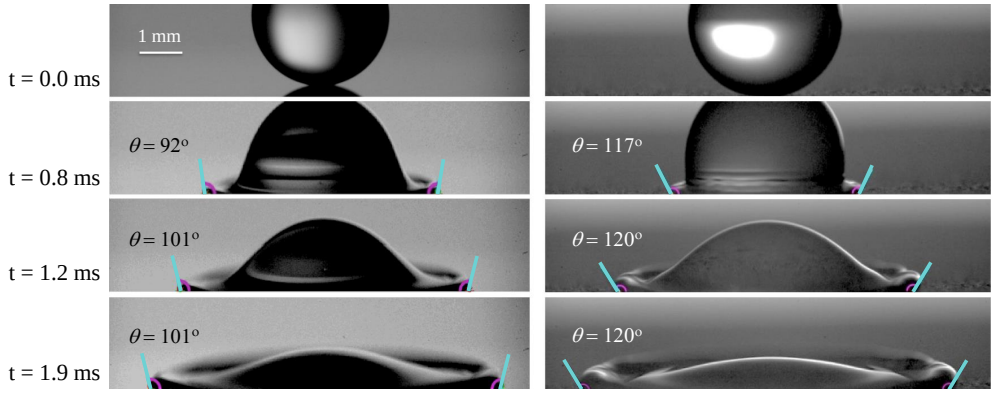

Figure 4.11: Illustration of the image analysis of a water droplet spreading on smooth (left) and 220 grit (right) diffusers. The blue lines show the tangent to the droplet at the pinning point (contact angle).

Past studies have focused on the influence of the surface roughness on the static contact angle [10, 16, 17] and splashing [66, 62, 86, 87, 84], however few attention has been given on the relation between surface roughness and the dynamic contact angle. Results in the previous section show that θ_{max} determines the splashing threshold in smooth surface. In the next two sections we study the influence of the roughness on the dynamic contact angle and its role on splashing.

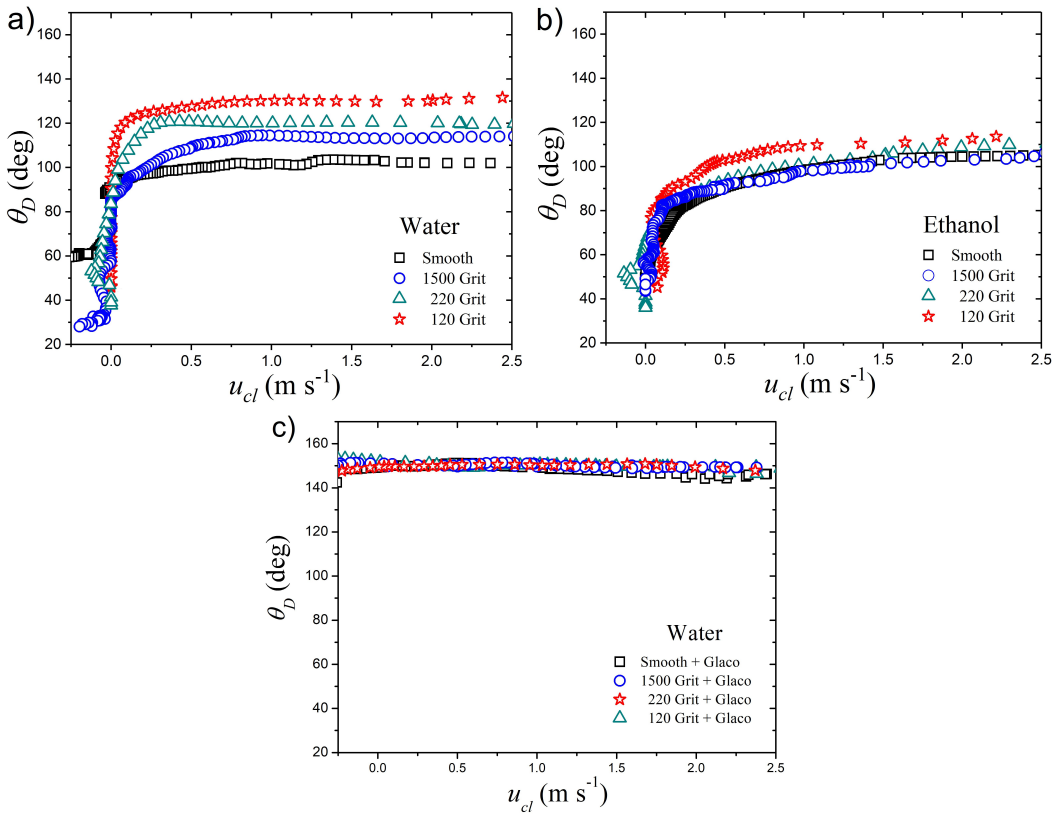

Figure 4.12: The dynamic contact angle θ_D in terms of the contact line speed u_{cl} for ethanol and water spreading on substrates of different roughness.

In this thesis we have found that the dynamic contact angle is influenced not just by its wettability (as described in the previous sections) but also by its surface roughness, as noted in Figs. 4.11 and 4.12. We can observe the most the influence of the substrate roughness, for water impacting the untreated surfaces where the angle varies from 101 degrees for the smooth surface to 131 degrees for the roughest surface used in this experiments. Figure 4.12 provides the complete behaviour of the dynamic contact angle for water impacting the different substrates. For ethanol, the influence of substrate roughness on the dynamic contact angle is not as clear as for water. The dynamic contact angle is greater for the 220 grit and 120 grit surfaces than for the smooth surface, in contrast for the 1500 grit surface the dynamic contact angle is lower; Fig. 4.12. Moreover, the difference between the dynamic contact angle of ethanol on the smoothest and the roughest surfaces is of 9 degrees, which is a third of the difference observed for water impacting the same two surfaces. These can be explained by the low surface tension of the ethanol as compared to the water's. The low ethanol surface tension facilitates its spreading over the solid

surface and has less viscous dissipation than water. This is consistent with previous works, where, a small effect of roughness during splashing and spreading conditions for wettable or low surface tension liquids was observed [27, 84, 130]. For substrates sprayed with Glaco all the substrates have the same θ_{max}, indicating that capillary forces dominate over the roughness effects and the viscous dissipation at the front of the drop below splashing conditions. This as well could mean that the spreading contact angle has a maximum.

According to the empirical relationship of Kistler [14], the dynamic contact angle is determined by the liquid properties and the equilibrium contact angle. We found that the Kistler model consistently underestimates the maximum advancing contact angle for rough substrates. In contrast, as seen in Fig. 4.13, the model fits reasonably well the experiments with water on smooth substrates if the static advancing contact angle is used instead of the equilibrium contact angle. The discrepancies seen on the dynamics of ethanol (Fig. 4.13) can be attributed to the large difference found between the static advancing contact angle and the maximum dynamic contact angle. In fact, one of the model's assumptions is that static and dynamic contact angles are similar at low speeds, but from the data in Table 4.3, we see this condition is not satisfied.

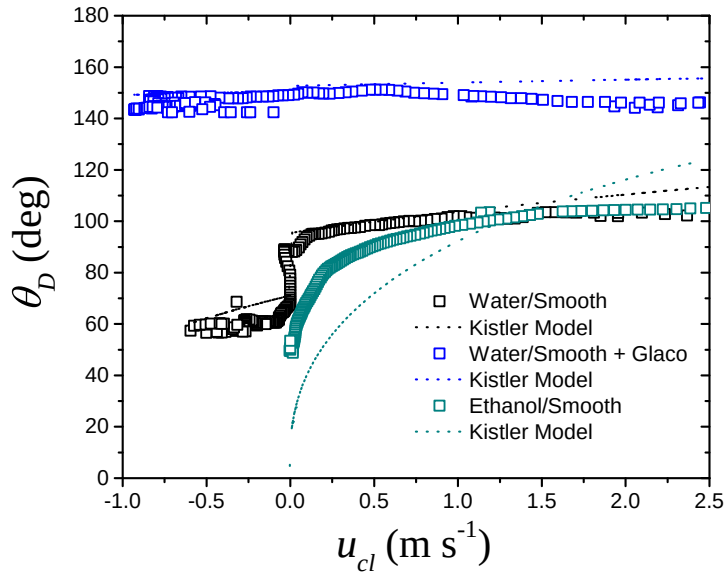

Figure 4.13: Comparison between the dynamic contact angle obtained experimentally and with the Kistler Model.

In our experiments, we found that the maximum spreading diameter of a droplet

impacting at 1.01 m/s is 6% smaller on the 120-grit surface than that on the smooth substrate. In contrast, for the Glaco covered substrates, the maximum spreading diameter difference between the 120 grit and the smooth surfaces is of only 1%. This observation is consistent with previous works that found that roughness hinders the spreading of impacting drops [87]. This is also in agreement with other works that have demonstrated spreading is more affected by roughness on hydrophilic substrates than on hydrophobic ones [88, 132, 133]. Moreover, at $U_0 = 2.05$ m/s (Fig. 4.14) the smallest spreading diameter was found on the Glaco covered smooth glass ($D_m = 2.87$), while the (uncoated) smooth glass showed the largest spreading diameter ($D_m = 3.59$) as expected [56].

4.3.4 Splashing on rough substrates

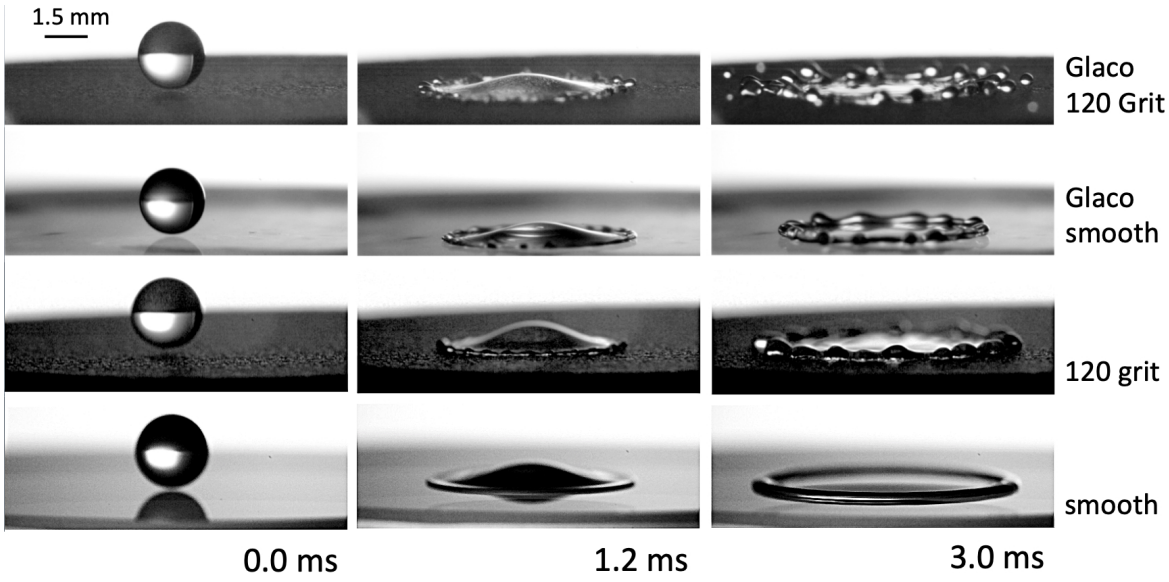

Figure 4.14: Snapshot sequences of water droplets impacting on smooth, Glaco-sprayed, and 120-grit rough glass at $U = 2.05$ m/s. Splashing is only observed on the Glaco-covered 120-grit rough glass.

We have shown that surface roughness affects the contact angle dynamics for hydrophilic surfaces, but not affecting the superhydrophobic ones. Following the work done on smooth surfaces we investigate the relation of splashing with surface roughness and wettability. Figure 4.15 shows experimental data of splashing and no splashing events for ethanol and water on all the substrates. In line with previous results [84, 86, 87], Fig. 4.15b, shows that roughness (R_a) affects the critical splash-

ing speed for all the substrate/liquid combinations. For water, the surface roughness effect on splashing is visible for all substrates used in this thesis. The same is true for water impacting Glaco sprayed surfaces. In comparison, for ethanol, the critical splashing velocity seems to be affected just by the roughness of the 120 grit surface (the roughest used in the experiments). Another interesting feature from Fig. 4.15 is that for the Glaco covered substrates the splashing threshold is considerably lower than for the uncoated surfaces. According experiments on smooth surfaces, we found that the splashing threshold is affected by surface wettability. Next, we investigated whether θ_{max} is able to characterise both the surface roughness and substrate wettability (Fig. 4.15). It has been noted that the wedge angle α is constant for smooth surfaces, however in this setup we have used surfaces of different roughness so α was not assumed as constant. We qualitatively observed that the value of α increases for increasing R_a, however due to the fingering of the lamella and the large deformation of the droplet, α is difficult to measure. Moreover, in some cases there is not possible to define a wedge angle because surface roughness prevents the thin sheet creation [62]. Therefore we decided to drop the dependence of $1/tan(\alpha)$ in the splashing parameter β. From Figs.4.10 and 4.15 we conclude that θ_{max} predicts splashing behaviour of water droplets impacting smooth and untreated surfaces, but fails for the rough Glaco coated substrates.

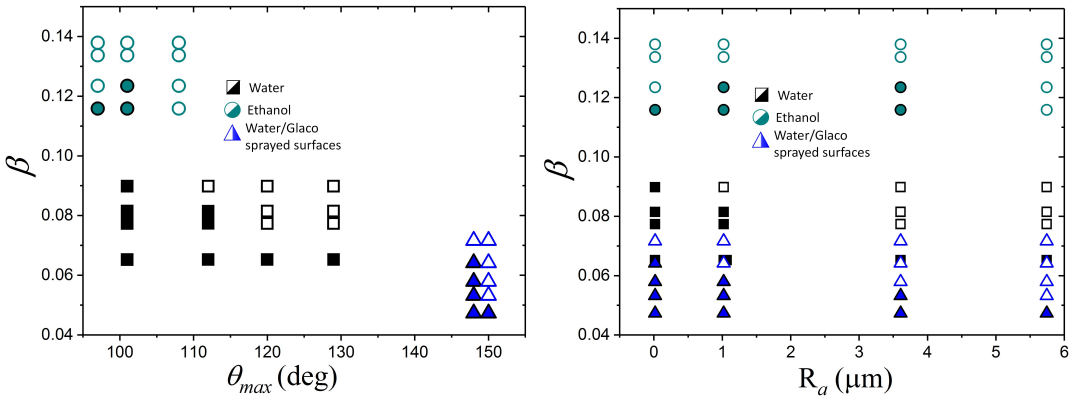

Figure 4.15: Left; Splashing behaviour in terms of splashing parameter β and the maximum dynamic contact angle θ_{max}. Right; Splashing behaviour in terms of splashing parameter β and the arithmetic amplitude average roughness (R_a). Open symbols represent splashing while solid ones stand for no splashing.

Our hypotesis is that, because θ_{max} presents a maximum for the Glaco covered surfaces, is not enough to characterise the system. For ethanol, as Figs. 4.12, 4.15

show, roughness plays a small role on the value of θ_{max} as well as in splashing. In both figures it can be seen that both are affected only by the roughest surface used in this study. Therefore, we can conclude that although the effect is small, θ_{max} can be used to model splashing for ethanol. Moreover in Fig. 4.14, we observe a water droplet impacting at 2.05 m/s onto substrates of different roughness (smooth and 120 grit) and different wettabilities (uncoated and Glaco coated). In this figure we only observe splashing for the 120 grit Glaco sprayed substrate, thus we can conclude that splashing is influenced by both surface roughness and surface wettability. Therefore, we propose the parameter β to be in terms of $(1+R_{pk}/R_{sm})(1-cos(\theta_{max}))$. We argue that θ_{max} is not able to characterise the splashing behaviour because at low impact speeds, on the superhydrophobic surfaces, the droplet spreads staying on a Cassie-Baxter state, i.e. it just touches the nanometric of the surface roughness and most of the droplet is sustained in the air not *interacting* with the micrometric roughness, or influencing θ_{max}. However, when the impact speed is near splashing, the droplet penetrates the air cushion into the micrometric roughness and then it spreads in a Cassie-Baxter-Wenzel state (Fig. 4.16); here the dynamics are corrected by a roughness factor. According to Reyssat et al. (2006), all our spreading experiments are in the Cassie-Baxter state as the impact velocities are below the transitional critical impact speed to the Wenzel state ($u_c = 3$ m/s) [22]. In contrast, we claim that Wenzel-Cassie-Baxter states are not found in our Glaco-coated surfaces because the micro-sized structure is wettable and yet bouncing is observed. This is also reflected on the dynamic contact angle. The Glaco-coated smooth glass is in a Cassie-Baxter state as there is no micro-sized structure. Furthermore, all the Glaco-coated substrates have the same dynamic contact angle indicating that all share the same state, i.e. Cassie-Baxter. The combination of Wenzel and Cassie-Baxter states have been reported for substrates with different roughness scales [18].

Following the approach of Wenzel [16], we have used the cosine of the maximum advancing contact angle to obtain a dimensionless parameter for the wettability factor. Additionally, to resemble the trend observed on smooth substrates, we have introduced the factor (1-cos θ_{max}). Furthermore, following the approach of Wen-

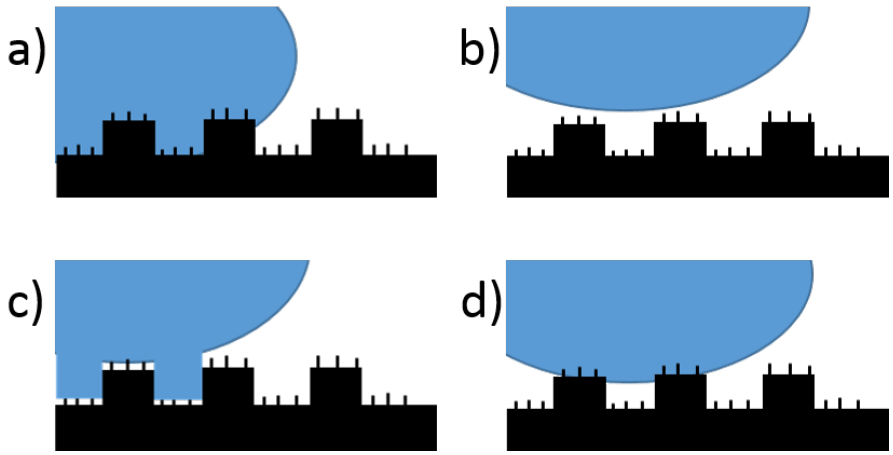

Figure 4.16: Schematic diagram of the possible states of a droplet on a multi-scale roughness surface; a) Wenzel state, the droplet wets both the nanometric and the micrometric structures; b)Cassie-Baxter state, the water droplet does not wet either of the multiscale roughnesses; c) Cassie-Baxter-Wenzel state, the drop sits in the micrometric state, while being in a Cassie-Baxter state for the nanometric roughness; d) Wenzel-Cassie-Baxter, the droplet wets the nanometric roughness while being in a Cassie-Baxter state for the micrometric roughness.

zel [16], the surface roughness factor was multiplied by the wettability parameter. Finally, the additive factor $(1+\mathrm{R}_{pk}/\mathrm{R}_{sm})$ is introduced to avoid zeroing the contribution of smooth substrates ($\mathrm{R}_{pk}/\mathrm{R}_{sm}$ is zero for smooth substrates). In Fig. 4.17 we show the parameter β in terms of $(1 + R_{pk}/R_{sm})(1 - cos(\theta_{max}))$. As observed, these parameters successfully divide splashing and no splashing events for all rough and smooth substrates and liquids. Moreover, these parameters also separate the splashing behaviour of the experiments on smooth surfaces.

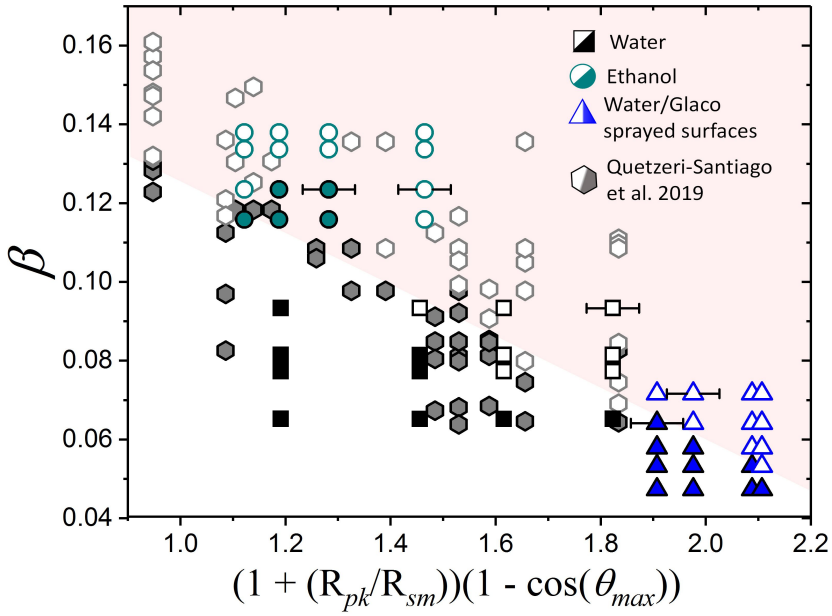

Figure 4.17: Splashing behaviour of water and ethanol drops in terms of the parameter (1 + (R_{pk}/R_{sm}))(1 -cos(θ_{max})).The splashing behaviour is well characterised for the different roughness and wettabilities. Open symbols represent splashing while solid ones stand for no splashing. Example error bars are shown at selected points. The shadowed region is a guide for the eye to separate splashing from spreading.

4.3.5 Corona & Prompt Splashing

As discussed previously, splashing is defined as the process in which a sheet of liquid ejected upon impact breaks up into droplets, and is often classified into two main categories, corona and prompt splashing. In the former, the liquid sheet that emerges at the front of the advancing contact line is lifted above the substrate and breaks up creating secondary droplets. In the latter, secondary droplets are rapidly ejected parallel to the substrate from the advancing lamella soon after impact. There is no formal definition of corona and prompt splashing apart from that based on the observable shape and timing of splashing, i.e. prompt splashing occurs quickly after impact and often at an angle parallel to the substrate, and corona splashing results from the fragmentation of the formed lamella [47]. However, as observed by Latka et al. in 2012, both types of splashing can occur within the same We and Re numbers [62]. In contrast, in 2015, Roisman, Lembach and Tropea demonstrated prompt splashing on smooth substrates occurs at $Re > 4,000$ and $We > 400$ [66]. In this thesis we visually classify our experiments, consequently corona splashing is defined as the splashing that comes after the creation and lifting of a thin sheet of liquid. In

contrast, prompt splashing is defined, as the splashing where there is no observable thin sheet.

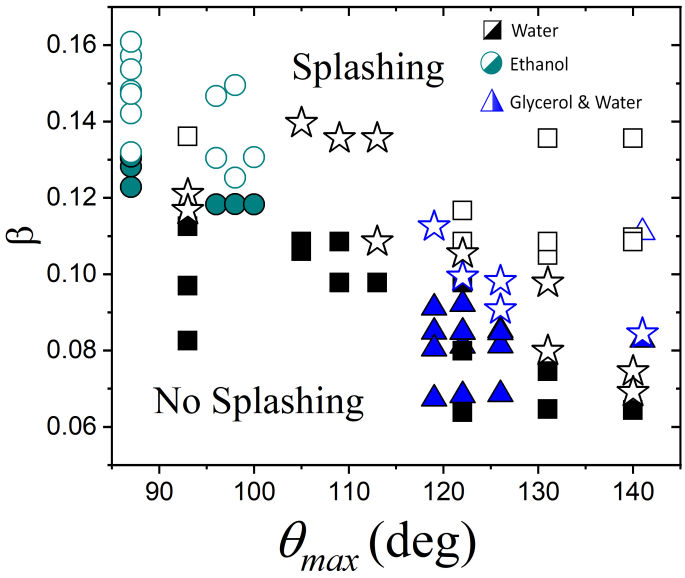

Figure 4.18: Splashing map for the impact of liquid droplets on smooth substrates. Close symbols denote spreading and open symbols denote splashing. Prompt splashing is denoted with stars.

For smooth substrates, results indicate that the transition between prompt to corona splashing occurs at increasing impact speed for the same liquid/substrate (Fig. 4.18). Interestingly, no prompt splash was observed for ethanol droplets. For the same impact speed, corona splashing is observed on non-wettable substrates but nearly no splashing is seen on wettable substrates. We attribute this effect on the difference of the contact line speed between a hydrophilic and a (super)hydrophobic substrates. This can be explained by the free slip of the contact line on superhydrophobic substrates. In contrast, in hydrophilic substrates the contact line pins and slows down. This is in line with past results that concluded that fast-enough contact line speeds promote prompt splashing [75, 83]. Moreover, during prompt splashing, the fast-moving contact line encounters the effect of capillary forces (greater for superhydrophobic substrates than for hydrophilic), generating a lifting force that develops into splashing [83]. The splashing map in Fig. 4.18 seems to work for dividing corona splashing for water and aqueous glycerol droplets, however failing for the ethanol.

Figure 4.18 shows the points where prompt splash occurred. For water droplets

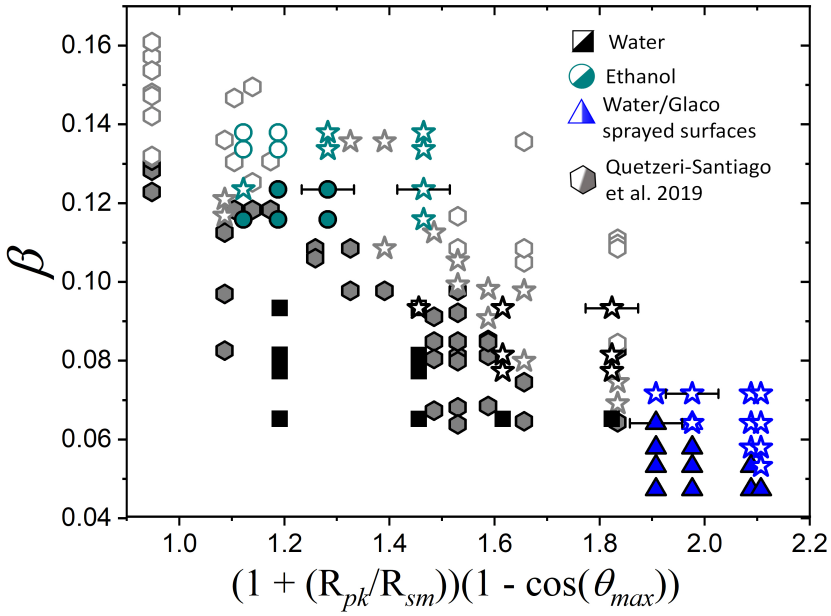

Figure 4.19: Splashing map for the impact of liquid droplets on rough substrates. Close symbols denote spreading and open symbols denote splashing. Prompt splashing is distinguished with the red colour.

a transition from prompt splash to corona splash can be seen on all the substrates. In contrast, prompt splashing is not observed for ethanol droplets impacting the smooth and the 1,500 grit substrates. In agreement with past works, we observed that surface roughness can suppress corona splashing and promote prompt splashing [2, 62, 94]. At the same impacting speeds, e.g. $U_0 = 2.24$ m/s , ethanol droplets present corona splashing on the 1,500 grit substrate but prompt splashing on the 120 grit surface.

Summarising, for smooth substrates we did not observed prompt splashing for ethanol droplets. In contrast, for water and aqueous glycerol droplets, we observed that with increased wettability and impact velocity corona splash was more probable. Our results also confirm that surface roughness suppress corona splashing but promotes prompt splashing. However, a more in depth study is needed to found a clear physical criterion to differentiate corona and prompt splashing.

4.4 Conclusions

We have characterised the effect of substrate wettability and roughness on the splashing behaviour of liquid droplets. Our results indicate that wettability and roughness

affects the contact line movement and so the spreading behaviour during impact. We have also found that the dynamic contact angle depends not only on the substrate wettability but also on the liquid properties. We have also found that spreading hydrophobicity on all the liquid/substrates studied here, i.e. liquids spread at a contact angle greater than $\theta_{max} \geq 87$ degrees. Our experiments demonstrate that an increase of surface roughness at the micrometer scale results in an increase of the maximum dynamic contact angle θ_{max}. In addition, this effect depends on the liquid surface tension, as roughness affects the dynamic contact angle of water more than it affects ethanol. In contrast, we have observed that micrometer scale roughness does not affect the spreading dynamics on (nanometer induced) superhydrophobic surfaces at low Weber numbers ($We \sim 35$). This observation is consistent with spreading occurring under a Cassie-Baxter state, where droplets do not wet the micrometer structures. These effects are included in our parametrisation by introducing the surface characteristics as the roughness ratio (peak to peak feature size over the surface feature mean width, R_{pk}/R_{sm}). We show that the splashing ratio β, combined with the maximum dynamic contact angle θ_{max}, and the roughness ratio successfully characterises the splashing behaviour on both, smooth and rough substrates used in this work. With this parameterisation (if liquid parameters and substrate roughness are known), the splashing threshold can be obtained by measuring the dynamic contact angle, instead of doing several experiments varying U_0.

Finally, we studied the difference between corona and prompt splashing finding that increasing θ_{max} and increasing impact speeds lead to corona splashing of water on smooth surfaces. Corona splashing was only observed in ethanol impacting smooth substrates. Furthermore, we found that roughness promotes prompt splashing while suppressing corona splashing. Despite these results, our work is not conclusive to make a clear distinction between corona and prompt splashing. A more detailed study, with a wider range of impact speeds and substrates is necessary to elucidate this question.

As most previous works, we have so far focused on the droplet impact dynamics on solid non-porous substrates. We have described the contact angle dynamics and

its relevance to the spreading and splashing of liquid droplets. These findings are of extreme importance for industrial processes like liquid dispensing, liquid coating, sprays, drug delivery, and any other application where splashing can affect coating performance or compromise surface finish or quality. Nevertheless, there are some practical applications, such as, the creation of protective and waterproof clothing, where understanding the droplet impact dynamics on textiles is critical. However, as mentioned before, this subject of study has often been overlooked. In the next chapter (Chapter 5) we study the droplet impact dynamics on textiles, i.e. porous solid substrates. We study the contact angle dynamics and the spreading diameter on textiles and compare them with the results obtained in this chapter. Furthermore, we highlight the relevance of the porosity and solid fraction of the textiles on the impact dynamics, which lead to unobserved phenomena on non-porous substrates.

Chapter 5

Contact line dynamics of droplet impact on textiles

This chapter contains experimental results and discussions on the droplet impact dynamics on nylon textiles. Textiles, unlike smooth solid substrates, are porous and this results in a *penetration* phase not observed in solid substrates. Here we find that the droplet penetration is governed by the Weber number and the textile pore size.

5.1 Introduction

Past chapters have looked into the droplet impact phenomena on solid impermeable substrates. In fact, most previous works have focused on solid, impenetrable substrates too but a minority of past works have studied droplet impacting on solid substrates with microtextures. For example, other forms of impact dynamics have been observed, through changes of the micro-posts height, separation and wettability, i.e. these changes induce the symmetric droplet splitting and pancake bouncing of droplets [90, 134]. In contrast, droplet impact on textiles has not been widely studied, although its understanding is necessary for the manufacturing of smart and protective clothing or in forensics studies [135, 136]. In this chapter we study the contact line dynamics and the penetration of droplets impacting textile nylon meshes.

The closest similar structures to textiles found in the droplet impact literature are impacts on micropillared substrates and rigid metallic meshes [21, 104, 106]. These works have been focused on the impact speed threshold for the droplet capture and penetration of a hole in a solid substrate, on the droplet penetration speed in terms of the pore size of porous films, and on the droplet contact time on metallic meshes [99, 104, 137]. Additionally, previous studies on droplet impact on textiles have been confined to the comparison of blood stain patterns after the impact of blood drops on different textiles and to the wetting on single fibre arrays [138, 139]. Here we focus on the droplet spreading, receding and penetration after impacting nylon textile meshes. In addition, we highlight the differences between the droplet impact dynamics on a textile mesh, micropillared and solid substrates. Finally, by using scaling arguments, we show that the critical penetration conditions depend on the pore size and the impact Weber number.

5.2 Experimental Method

The experimental setup is similar to those described in previous chapters, the only modification is on the replacement of the rotating platform by a system to hold, flat

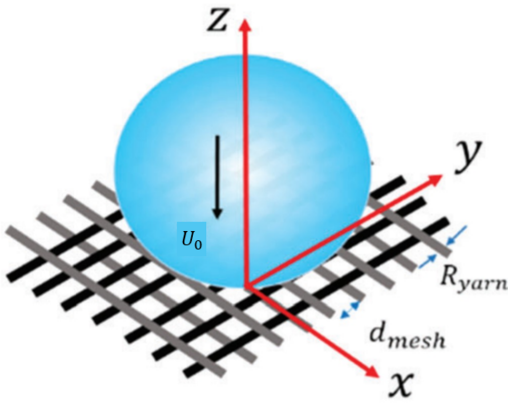

Figure 5.1: Schematic diagram of the experiment. A water droplet impacts with speed U_0 on a textile mesh of a given pore size (d_{mesh}) and yarn size R_{yarn}

and horizontal, the nylon textiles. The diagram of the experimental setup is shown in Fig. 5.1. Here, our nylon textiles are coated with Perflourinates PFAC8 and PFAC6 by plasma treatment to provide hydrophobicity. The static contact angle of both coatings was measured to be 123 degrees, and the contact angle hysteresis has been reported to be 55 degrees for PFAC6 and 37 degrees for PFAC8 [108]. The nylon textiles samples, were cut into squared meshes and were formed by intertwined monofilaments. Pore sizes (d_{mesh}) of the nylon textiles ranged from 100 μm to 300 μm. Here, the pores are defined as the square openings between the the textile yarns. Moreover, the yarn thickness varied from textile samples and is referred as R_{yarn}. Figure 5.2 shows an SEM image of a typical nylon textile. Insets on Fig. 5.2 show the micrometer structure of the hydrophobic coating. The scale of the coating is of a few micrometers, therefore it did not affect the *macroscopic* textile structure.

For the experiments, the nylon mesh textile was held with a Deβen micro-test device so that the tensile stress could be measured and controlled. To avoid complications from textile deformations and motion, the nylon mesh was held with a tensile force of 2.5 ± 0.1 N for all the experiments. This force did not affect the geometry of the textiles while keeping them *rigid*. Liquid droplets were created from a droplet generator (see Chapter 2) and impacted on the textile meshes. Droplets were made from a solution of aqueous glycerol with surface tension at room temperature of $\sigma = 68.5 \pm 1.5$ mN/m. In the experiments presented in this chapter, droplet size was kept constant at $D_0 = 1.56 \pm 0.12$ mm. The range of impact velocities used in this experiments ranged from 0.88 to 1.90 m/s. The imaging and processing systems

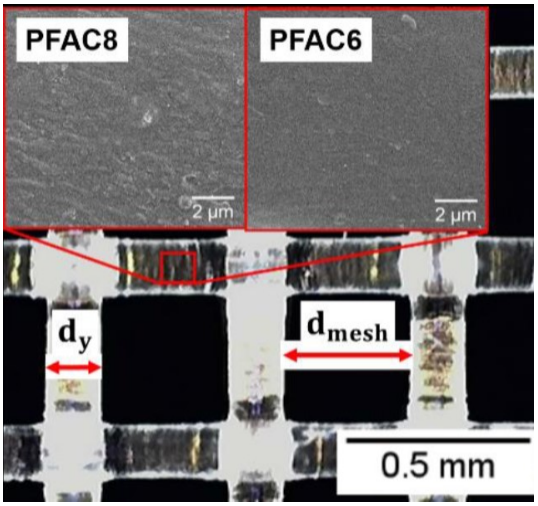

Figure 5.2: SEM image of a nylon textile. The image reveals the mesh type structure of the textile. The insets show the micrometric structure of the PFAC8 and PFAC6 coatings.

are described in Chapter 2.

5.3 Results and Discussion

In this section we present the obtained results on the droplet impact dynamics on textiles. First we present an analysis of the spreading diameter in terms of time, and show its similarities to droplet spreading on smooth impermeable substrates. In addition, we describe an impact stage just observed for porous substrates, namely, the penetration stage. This stage is characterised by the penetration of the droplet to the textile and the absence of a liquid rim around the droplet. Moreover, we analyse the dynamic contact angle and maximum spreading of the droplets impacting at different Weber numbers. Our results show, that for textiles with high solid fraction ($\Gamma > 66\%$) the maximum spreading diameter follows the value predicted for solid substrates, but deviates for leaking substrates. Finally, by using scaling arguments, we show that the critical penetration conditions depend on the pore size and the Weber number.

5.3.1 Contact diameter evolution on the textile surface

Figure 5.3 shows the dimensionless spreading diameter $d(t) = D(t)/D_{max}$ of the droplet in terms of the adimensional time $t^* = t(U_0/D_0)$). The inset in Fig. 5.3 shows that for early times $0.25 < t^* < 0.9$ the spreading diameter follows a potential

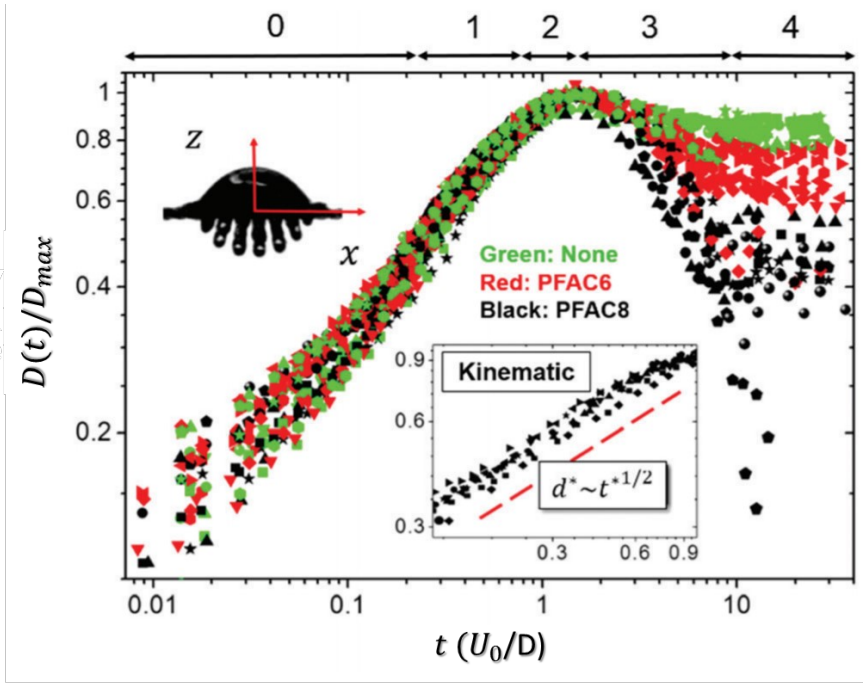

Figure 5.3: Droplet spreading and receding diameters as a function of $t^* = t(U_0/D_0)$, for different We numbers and various textiles with pores ranging from 100–300 mm. The colours indicate different textile coatings: green for non-coated, red for PFAC6 coated, and black for PFAC8 coated textiles. The inset shows the scaling $d(t) \sim t^{*1/2}$ characteristic of the kinematic stage. All data included. Measurement error ±2 pixels.

law, i.e. $d(t) \approx t^{*1/2}$. This is consistent with previous works studying the spreading diameter of droplet impact on impermeable solids [48]. This stage is often named as the kinematic stage, since the dominant force during this stage is inertia. This stage is characterised by the late formation of a radial liquid lamella at the base of the droplet. The lamella expands on the textile surface, and the droplet volume above the lamella flattens. Here, the capillary time is defined as $t^*_{capillary} = \left(\frac{\rho d^3_{mesh}}{\sigma}\right)\frac{U_0}{D_0}$, which is the time at which the capillary forces start acting. Within the experimental conditions $t^*_{capillary}$ is in the range from 0.1 to 0.7, which coincides with the kinematic stage.

At the end of the Kinematic stage capillary and viscous forces dominate, therefore the relation $d(t) \approx t^{*1/2}$, is no longer valid. This stage is known as the spreading stage and the droplet adopts a pancake shape in the textile surface, while, at the textile's back, liquid fingers elongate and break if the kinetic energy is enough. The contact line dynamics on the textile surface is similar for all the various textiles characteristics, regardless of the We number, as seen in Fig. 5.3. Our data shows that if penetration is observed d_m is lower than for a droplet impacting a solid

impenetrable substrate.

At the end of the spreading stage comes relaxation stage, where receding is typically observed. In this stage surface characteristics such as wettability and contact angle hysteresis play a major role on the final outcome [56]. Finally, in the equilibrium stage the droplet finds its equilibrium contact diameter. In Fig. 5.3 we see the importance of the surface wettability and contact angle hysteresis. The hydrophobic coated surfaces have a smaller equilibrium contact diameter than the uncoated ones. Moreover, due to the larger contact angle hysteresis of the PFAC6 compared to the PFAC8, the equilibrium contact diameter in the textiles treated with PFAC6 is larger than for the ones treated with PFAC8.

5.3.2 Penetration stage

Despite the similarities between droplet impact and spreading on impermeable and porous solids, we found a unique characteristic stage for porous solids. We have named this stage the penetration stage, as the droplet can pass through the textile mesh forming fingers below the impacting plane. This stage occurs at times before the kinematic stage, $t^* < 0.25$. The penetration stage is characterised by the penetration of the liquid droplet through the textile pores. The textile pores allow the air to escape, therefore not trapping an air bubble inside the droplet as opposed to impact on non-porous solids. Moreover, pores reduce the normal pressure exerted on the substrate and the flow redirection in the horizontal direction is reduced. Only when the droplet has penetrated sufficiently, the average pressure near the textile is sufficiently large to cause the flow re-direction. As a result, the re-direction process in textiles is retarded in comparison to impermeable solids. Figure 5.5, shows snapshots for times ($t^* < 0.25$) of the impact at the same Weber numbers on a porous (textile) and a non-porous substrate with the same wettability. For the case of textiles, a liquid lamella does not form during the penetration phase. In contrast, on the non-porous substrate the lamella is formed at a time $t^* \approx 0.14$. Moreover, small lateral distortion of the droplet is observed while the droplet impacts and penetrates the textile. In Fig. 5.4, we observe that an impacting droplet can penetrate the tex-

tile while maintaining its spherical shape. We observed this condition for textiles with pore sizes between 100 and 300 μm and We 20. In Fig. 5.4, we overlap a circle with red dashed lines on the droplet. Our assumption is that the droplet moves through the mesh without changing shape, i.e. we consider a circle with diameter D_0, moving in the negative direction of the z-axis with speed U_0. Here $z = 0$ is the substrate position. As our experimental setup just captures a 2D image of the droplet, this assumption is justified. At the impacting time $t = 0$ the circle touches the substrate at one point and its centre is at a distance $D(0) = D_0/2$ from the z-axis. Assuming the centre of the circle is at $x = 0$, the equation of the moving circle is:

$$x^2 + (z - \frac{D_0}{2} + U_0\, t)^2 = (\frac{D_0}{2})^2. \tag{5.1}$$

The length of the intersection of the circle at a time $t > 0$ at $z = 0$, should be able to predict the spreading diameter D(t), of the droplet. Therefore,

$$D(t) \approx \sqrt{D_0\, U_0\, t - (U_0\, t)^2} \tag{5.2}$$

and the droplet height with respect to $z = 0$, is,

$$h = D - U_0\, t. \tag{5.3}$$

Equation 5.3, seems to be at odds with the exponential dependency found in [140]. However, when for small values the exponential reduces to a linear function. We emphasise that equation 5.3, is a valid approximation for the first instants of the droplet impact. Additionally, the model used in equation 5.3, does not include the liquid properties and the surface energy. We therefore conclude that the model found in [140] is more accurate and it is preferred over Eq. 5.3 for $t^* > 0.25$.

The experimental data shown in Fig. 5.4, for $0 < t^* < 0.25$ and $We > 20$, shows good agreement with the predictions of Eqs. 5.2 and 5.3.

We conclude this section by highlighting that the penetration stage is just seen in porous systems like textiles or metallic meshes. This penetration stage is driven by

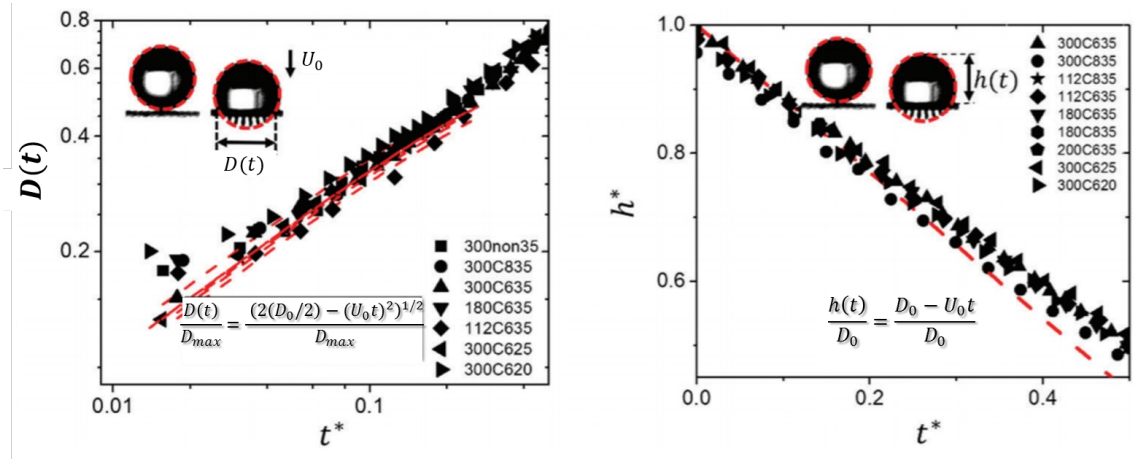

Figure 5.4: Droplet penetration times $0 < t^* < 0.5$. The results show the droplet penetrating the textile with no shape variations. Here, $d = D_0/D_{max}$ and $h^* = h/D_0$. The legend indicates the textile mesh size in micrometres, the type of coating, and the We number, e.g. 300C635 stands for mesh size 300 mm, PFAC6 coating, and $We = 35$. Penetration is not observed for $We < 20$. The dashed lines correspond to Eq. 5.2 (left) and Eq. 5.3 (right). Measurement error 2 pixels.

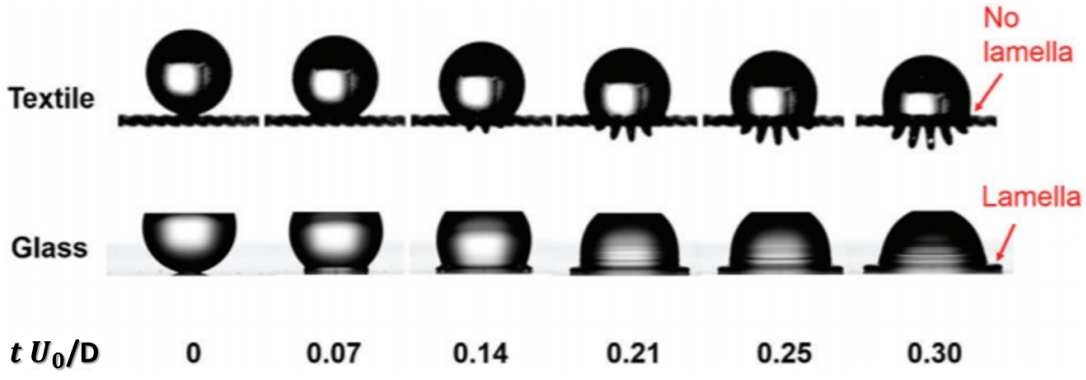

Figure 5.5: Image sequences comparing droplet impact on an N-300 textile and a liquid-repellent glass slide for $We = 36$ and $We = 40$, to illustrate the effect of substrate permeability on the droplet deformation. Both the glass substrate and the textile are coated with PFAC6.

inertia as, in the kinematic stage on non-porous substrates, but there are remarkable differences, like the absence of the lamella at the base of the droplet.

5.3.3 Penetration regimes and critical penetration parameters

Experimental results on the impact of droplets show two types of penetration regimes; partial and complete penetration. In the former, the droplet penetrates through the surface, but is sucked back by the droplet on the side of the impact, and the whole liquid volume is retained by the textile. In the latter, the droplet penetrates the substrate, forming liquid fingers at the back of the substrate that eventually break into secondary droplets. Therefore, part of the liquid is not retained by the textile. Moreover, our results show a direct influence of the contact angle hysteresis on these phenomena. We observed that for the partial penetration case, the liquid that penetrates the textiles treated with PFAC6 stays at the back of the surface. In contrast, for PFAC8 all the liquid get sucked back and remained on top of the surface. We assume this phenomenon is owed to the differences in contact angle hysteresis between PFAC6 and PFAC8.

We performed a balance between inertia and capillary forces to investigate the parameters governing the two penetration regimes. Here, we neglect viscous effects as it has been found that for $Re > 10$, inertia dominates. In a typical experiment conducted in this set of experiments $\rho \approx 10^3$ kg/m^3, $\mu \approx 10^{-2}$ Pa s, $D_0 \approx 10^{-3}$m and $U_0 \approx 1$ m/s, therefore $Re \approx 100$.

Following the work of S. Ryu et al. (2017) [103], the capillary forces scale as $\sigma\, d_{mesh}$. In contrast, the inertial forces scale as $k\,\rho\, U_0^2$, where k is a constant determined by the surface parameters, such as the wettability or geometry of the mesh. Balancing the relevant forces we have,

$$k\,\rho\, U_0^2 \approx \sigma / d_{mesh}, \tag{5.4}$$

or alternatively, in terms of the Weber number this can be written as,

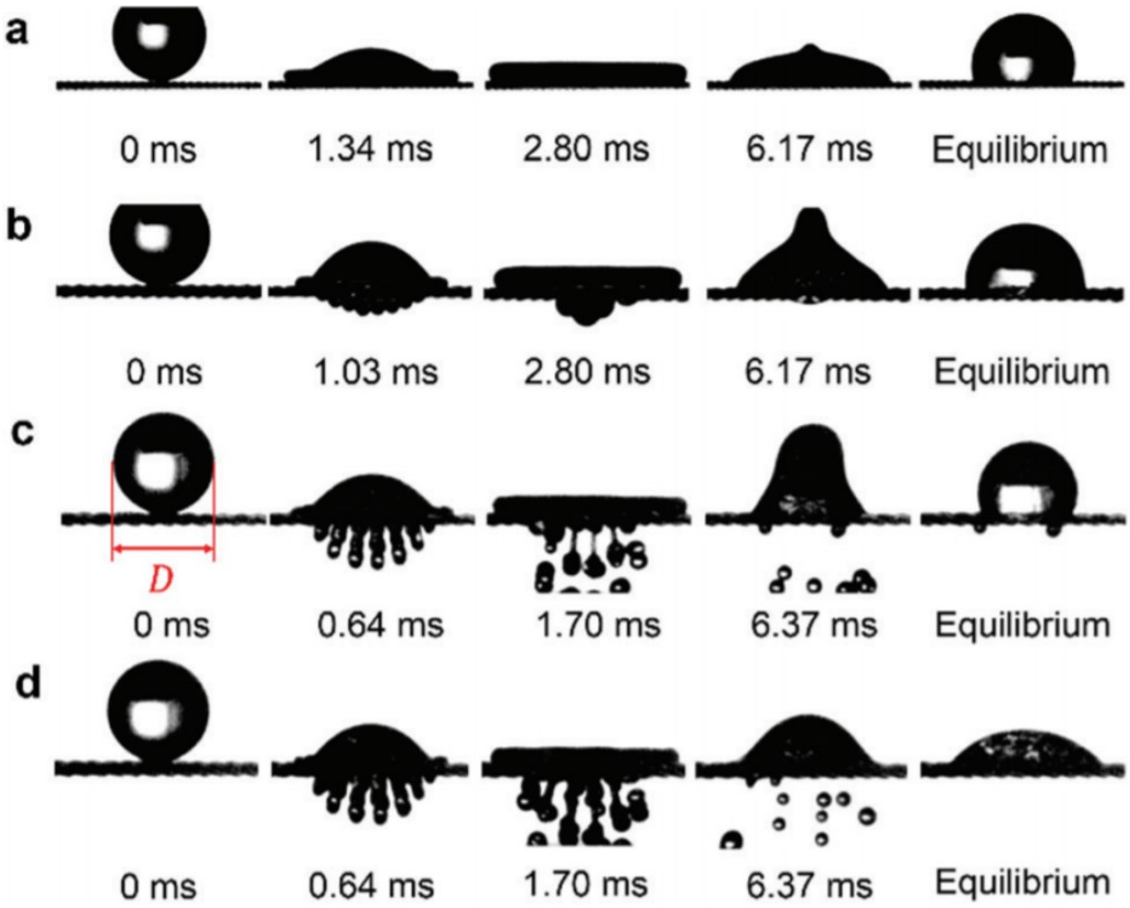

Figure 5.6: Penetration behaviour of droplet ($D_0 \approx 1.56$ mm) for increasing We numbers. The sequence in (a) shows no penetration for $We \approx 8.9$ and $d_{mesh} \approx 101$ μm. In (b), $We \approx 8.3$ and $d_{mesh} \approx 203$ μm, a portion of the droplet penetrates the textile but is driven back to the top surface. In (c), $We \approx 35.0$ and $d_{mesh} \approx 303$ μm, a fraction of the droplet permanently penetrates the textile, forming liquid filaments that break up into secondary droplets. The textiles for (a–c) are all PFAC8 nylon. In (d), $We \approx 25$ and $d_{mesh} \approx 303$ μm and the textile is non-coated nylon. The penetration behaviour of (d) is similar to (c) but the receding phase differs due to the hydrophilicity of the non-coated textile.

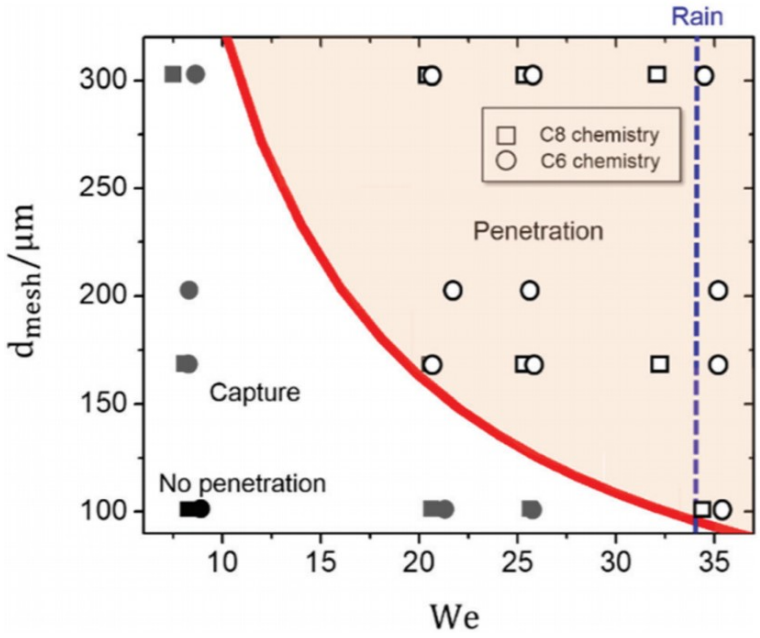

Figure 5.7: Penetration regimes for droplets impacting textiles. The solid line indicates the boundary between the penetration and no penetration regimes. Hollow symbols denote textile penetration. Gray symbols indicate capture, i.e. a portion of the droplet penetrates but is eventually drawn back to the impact surface. Black symbols indicate no penetration where neither temporary liquid penetration nor droplet footprint is observed on the back surface

$$d_{mesh} \approx D_0/2kWe, \tag{5.5}$$

where $k = 0.24$ is the best fit obtained by contrasting the scaling with the experimental data. The results of the experiments for different pore sizes is shown in Fig. 5.7. In this figure, open symbols refer to the complete penetration regime and close symbols to the partial penetration regime. Figure 5.7, shows that Eq. 5.5, adequately separates the partial and complete penetration regimes for the range of Weber numbers $7 < We < 37$. This is in agreement with previous results where it has been found droplet penetration on both hydrophobic and superhydrophobic meshes ($D_0 = 3.5$ mm $d_{mesh} > 140$ μm) occurs at $We = 35$ [103, 104]. Finally, we give an estimation of the pore size required to repel a typical-sized rain droplet. The velocity of a rain droplet of size $d_{rain} \approx 1.6$ mm is $U_0 \approx 1.77$ m/s [141]. Therefore according to Eq. 5.5 and Fig. 5.7, d_{mesh} should be less than 100 μm.

The results in this chapter indicate that the best technique to avoid liquid penetration on a textile is by reducing the mesh size. Moreover, hydrophobic coating with low hysteresis is better for maintaining the liquid away from the surface at later

times, but is not sufficient to prevent a liquid from penetrating the textile. This can be deduced from the penetration stage found at times t^*, since the only parameters that come into play at this stage are the inertial forces. Moreover, capillary forces just come into action at a time given by $t^*_{capillary}$ which, in this work, was found to be in the range between 0.1–0.7.

5.3.4 Impact on (complex) cotton textiles

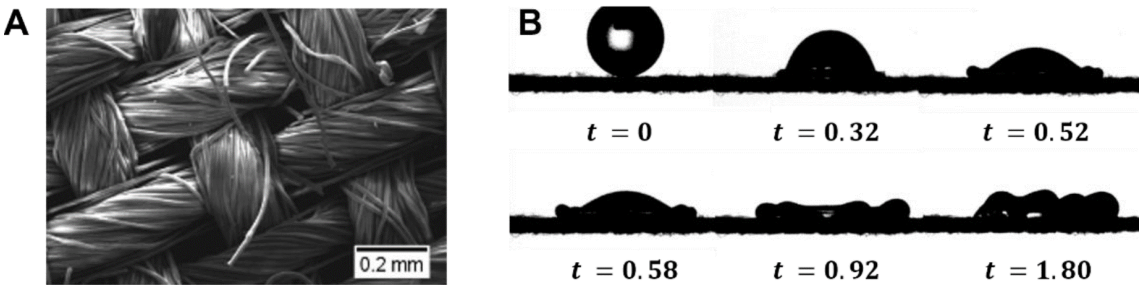

Figure 5.8: A. SEM image of a PFAC8 coated cotton textile. B. Image sequence of a droplet impact on a cotton textile, $We = 11.5$ and $D_0 = 1.56 \pm 0.12$ mm.

This section studies the impact dynamics on cotton textiles. Cotton textiles are more complex than the nylon meshes studied here. As opposed to nylon textiles, cotton textiles consist on multiple intertwined fibres that create a rough non-homogeneous substrate. Cotton textiles have a pore size smaller than the smallest nylon textile used here. Figure 5.8 A, shows an SEM image of a cotton textile. Figure 5.8 B, shows the spreading and receding of an impacting droplet in a PFAC6 coated cotton textile at $We = 11.5$. In this sequence of images we observe that the spreading is not completely symmetric. This is expected as the cotton textile has an non-homogeneous surface.

Figure 5.9 shows the contact angle dynamics of an impact on a PFAC8 coated cotton textile. The data is not consistent with the results for an impact at similar Weber numbers on a smooth surface (see section 4.3.4). This is because fibres are not perfectly aligned with the horizontal axis and could alter the contact angle. Moreover, the detection of the solid boundary was more difficult as the substrate is not uniformly flat. Consequently, we measured the contact angle from a few pixels above the contact line. As discussed in Chapter 2 this affects the measurement because the curvature near the pinning point is not well captured by the code.

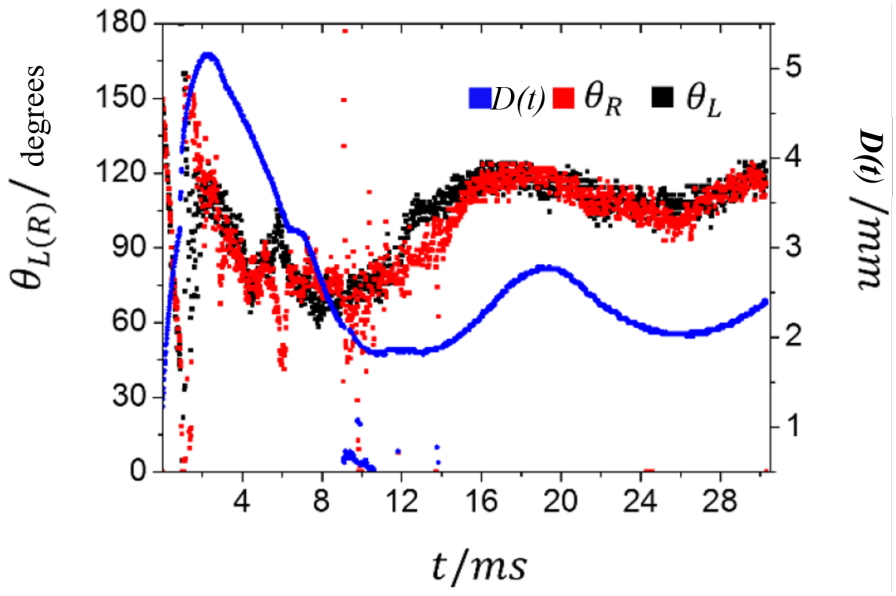

Figure 5.9: Contact angle dynamics and spreading diameter in terms of time of a droplet impact a cotton textile. The Weber number for this experiment is 11.5.

Nevertheless, as the off-set was small, we could capture some similarities with the drop impacts on smooth surfaces. At the maximum spreading diameter we observe a decrease on the contact angle value (hysteresis), then as the receding commence, the contact angle stays constant in the range from 6 to 12 ms. Finally, in the equilibrium stage, the contact angle oscillates as the droplet diameter oscillates until it reaches its equilibrium diameter. As the solid fraction of the cotton textiles used here is large ($\Gamma > 66\%$), we expect the impacting dynamics on cotton textiles, to be equivalent to the impact dynamics on non-porous substrates with heterogeneous roughness. Therefore, if no out of plane fibres are present, we expect the results and conclusions from Chapter 4 subsection 4.3.3 to apply here.

5.4 Conclusions

In this chapter, we have reported and discussed drop impact experiments on textiles with varying pore size and solid volume fraction. Textiles were rendered hydrophobic by two different coatings, PFAC6 and PFAC8, with the same static contact angle but different contact angle hysteresis. Our results are in agreement with previous works on metallic meshes [103, 104]. We highlighted the importance of the contact angle hysteresis during the relaxation and equilibrium phases. Textiles coated with PFAC8 show a smaller equilibrium contact diameter than the ones coated with

PFAC6, despite having the same static contact angle. In addition, we found a characteristic stage for the nylon textile meshes, that we have named penetration stage, characterised by being solely driven by inertia and occurring at times $t^* < 0.25$. At this stage, droplets do not largely deform and can be considered as a falling sphere. Furthermore, no lamella is formed on the base of the droplet, as opposed to non-porous solid substrates at equivalent times. We note however, that for later times the spreading model of a decaying exponential found in [140] should be used. We also were able to predict the transition between two distinctively penetration phenomena, namely, complete and partial penetration. This two-regime threshold is well characterised by the balance between the capillary and inertial forces, as represented in Eq. 5.5 and Fig. 5.7.

In this and previous chapters, we have focused on the contact line dynamics on substrates ranging from wettable to non-wettable, and from porous to non-porous. Our results indicate that the contact angle dynamics and impact outcome depend on the liquid properties (surface tension and viscosity) and the substrate properties (wettability, porosity and roughness). Additionally, we showed that the spreading dynamics are qualitatively similar for porous and non porous substrates. In the next chapter we present an application of the results obtained so far. Based on the droplet generator introduced in Chapter 2, we present a system capable of printing liquid latex with 60 %wt of solid content. We apply our findings on droplet spreading, for a precise control of the droplet deposition. Furthermore, we present the first (to the best of our knowledge) 3D printed latex objects.

Chapter 6

Liquid latex 3D printing with the Droplet on Demand method

This chapter presents a new approach to additive manufacturing with liquid latex, using the drop-on-demand (DoD) system described in chapter 2. The setup allows printing with viscous liquid latex with a solid content of 60 % wt. The process is controllable and reliable, making the printing of patterns possible.

6.1 Introduction

Based on the droplet on demand system described in Chapter 2, in this chapter we present a system that can jet liquid latex. By applying the results obtained in chapters 3-5, we obtained a system capable of producing uniform sized latex droplets and allows precise control for their deposition. The design benefits from an actuator with a higher force compared to conventional 3D printers, allowing us to print viscous fluids as well as liquids with solid particles. The print-head is assembled from three plates containing the actuator, ink chamber and nozzle opening, respectively. Our system jets droplets onto a substrate that subsequently cure. Droplets are placed adjacently to each other to allow them to coalesce and form a uniform straight array (or line). The z-axis definition is created by overlaying layers, with intermittent curing or crosslinking steps to ensure adequate support of subsequent layers. An example of a *complex* pattern printed with our system is shown in Fig. 6.1.

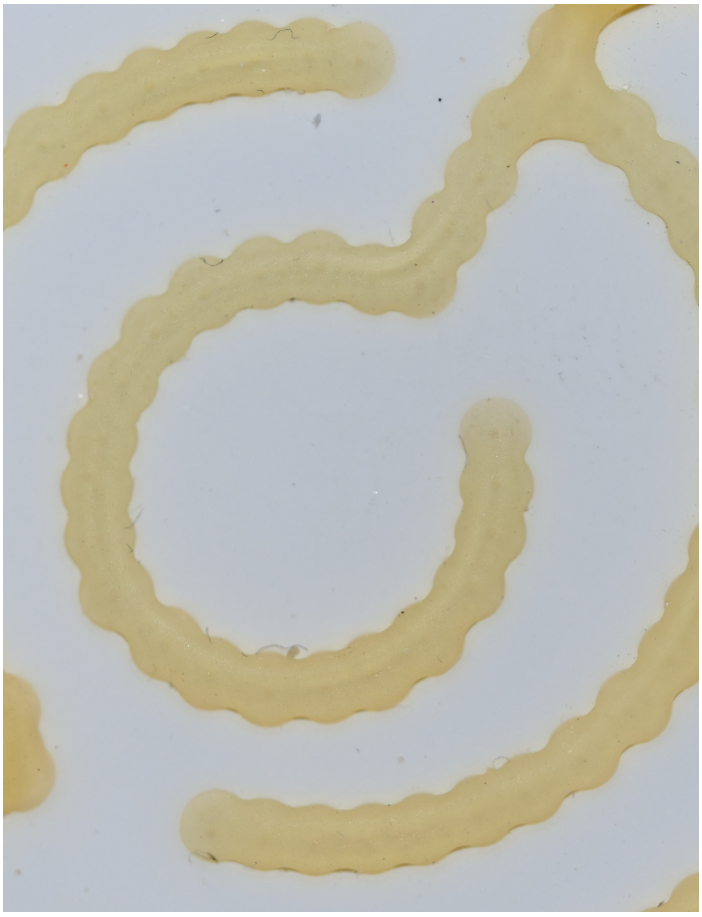

Figure 6.1: Example of a latex complex pattern printed with the system presented in this chapter.

In general, in Droplet on Demand printing (DoD), a pressure pulse induced by thermal, piezoelectric or acoustic actuation causes a liquid droplet to form and jet from the print-head nozzle. DoD has a number of advantages above other additive manufacturing (AM) technologies; firstly, there is no substrate contact, avoiding contamination of the nozzle, and secondly, higher printing speeds can be achieved compared with, for example, fused deposition modelling (FDM) [142]. Moreover DoD methods allow a greater control and variability of the droplet volume and speed [143, 144]. In addition, it is a digital technology with great flexibility that naturally permits personalisation and one-off production. Unfortunately, material compatibility is an issue in commercial inkjet systems as the technology is restricted to operate under a narrow window of liquid viscosities.

Recent advances in the field, includes examples of rubber latex being successfully printed using inkjet; Raza et al. used a commercially available Microfab print-head to print low melting point alloys and elastomers [145], and Lukić et al. printed diluted liquid latex (35 wt. % solid content) with a commercially available piezoelectric inkjet printer [146]. Whilst these examples show that progress has been made, the techniques still suffer from similar limitations in ink viscosity, solid content, nozzle clogging, and agglomeration. In addition, inks used in AM methods have additional requirements to that of deposition resolution, as droplets are required to cure or solidify fast and leave an adequate footprint to build definition in the z-axis. These restrictions still need to be addressed to improve 3D printed objects made from viscous or high solid content materials such as bio-gels, conductive inks, and liquid latex.

From the limitations in DoD printing, solid particle loading is one of the main limitations across all inkjet industries. The industry standard for conventional inkjet indicates that jetting is possible at a maximum viscosity of 20 mPa s, with a solids loading of $< 10\%$ per volume, and a particle diameter no greater than $1/20$ of the nozzle diameter [142, 146, 147, 148]. Whilst being able to inkjet un-diluted liquid latex is an interesting prospect in itself, the ability to add solid particles to form a colloidal ink widens the market applications for this technique. This is because

the addition of particles can be used to reinforce mechanical properties or improve other properties such as thermal and electric conductivity, stiffness or elasticity of a given construct. Moreover, this includes the possibility of reusing discarded rubber materials, such as, micronized rubber powder (MRP), in the manufacturing of new products.

In recent years, there has been a move towards producing MRP from waste materials such as tires. Tires remain a major source of waste, despite an increase in governmental initiatives to promote their recycling. In the USA alone, there are still 67 million tires occupying landfills, and an estimate of 25% (2010) of all end-of-life tires are placed into landfills worldwide [149]. Currently, a mere 10% of end-of-life tires are recycled to create new products [149]. A reason for the low rate is the lack of suitable recycling methods and the limited ability to make new products with discarded material. MRP has proved to be environmental friendly as it can be obtained mechanically with no contaminants released to the environment. The benefits, in terms of costs, have been previously demonstrated in the manufacturing of MRP by creating moulded and extruded products [150, 151, 152].

This chapter describes a method to inkjet print liquid latex and MRP, as a step towards cheaper manufacturing with elastomer/rubber based materials. We introduce a versatile DoD inkjet print-head capable of printing pure liquid latex containing a 60 wt. % solid content and a liquid viscosity of 21.8 $\pm$ 0.2 mPa s. Moreover, we explore the concept of creating hybrid MRP/latex constructs by using colloidal inks of latex and MRP. Our results show that, in this instance, the inclusion of MRP does not affect the stiffness of the cured product but affects its elasticity. Finally, we demonstrate that this ink can be used to manufacture cured latex patterns by DoD deposition and natural curing.

6.2 Experimental Method

6.2.1 Ink preparation

Two types of ink formulations were used in this study; pure liquid latex and liquid latex with a suspension of rubber tire waste or fine rubber powder (parlon powder). Pure liquid latex was acquired from Liquid Latex Direct, UK. The liquid latex contains 60% natural rubber, 40% water and $< 0.3\%$ ammonia. The density was measured to be 940 $\pm$ 50 mg mL^{-1} and the viscosity to 21.8 $\pm$ 0.2 mPa s. Suspensions were made using parlon powder and thereafter with a coarse rubber powder made from of end-of-life rubber, namely, micronized rubber powder (MRP). Suspensions were made by dispersing the parlon powder or MRP in undiluted liquid latex. The weight percentage of suspended MRP or parlon powder was calculated as 'WMRP/(WL+WMRP)' or 'WP/(WL+WP)', where WMRP, WP and WL refer to the weight of MRP, parlon powder and undiluted liquid latex respectively. Synthetic white parlon powder was purchased from IONXIA, UK ($\sim$66% chlorine and $< 2.5\%$ toluene) and MRP was kindly provided by Artis UK. A heterogeneous mixture of MRP was used with a maximum particle size of 0.6 mm. Parlon powder was suspended at concentrations of 3.5 to 6.7 wt. %. MRP was suspended at the concentration 9.6 wt. % when used for printing. Mechanical testing was carried out on cast and cured latex samples containing MRP at concentrations 0, 5, 9 and 16 wt. %.

6.2.2 Print-head and 3D printer setup

For our experiments, two print-head designs were used. Both print-heads function under the DoD mode and are similar to the droplet generator described in the experimental setup section (section 2). The print-heads are fed with fresh ink through an attached syringe which in turn is attached to a fast-acting meniscus controller (Inca Digital Printers Ltd., UK) used to balance the pressure inside the print-head and the atmospheric pressure, keeping the meniscus pinned at the nozzle. Two print-head sizes were used to assess their performance with the colloidal inks. The small

print-head uses a 20.0 mm diameter loudspeaker (8 Ohms, 0.1 W), has an inner liquid reservoir volume of 4 mL, and a conical nozzle with an outer diameter of 1.0 mm. A larger print-head uses a Visaton Structure-Borne Driver loudspeaker (8 Ohms, 25 W) with a 9 mL volume reservoir, and a 0.85 mm conical nozzle. We claim that these drivers (loudspeakers) have more actuation power than other piezoelectric driven print-heads, e.g. MicroFab and MicroDrop, so making the printing of high viscosity liquids a reality. The driving signals on both systems are produced using a (TTi) pulse generator, an acoustic amplifier, and recorded by a digital oscilloscope. The waveform is kept to a single pulse, with control over the pulse amplitude and width, to adjust the droplet speed and size.

The small print-head was mounted on to a 2D motorised stage and the substrate (Kodak inkjet paper) was secured to a support at a fixed distance. In contrast, the larger print-head was fixed to a vibration damped support and the substrate mounted onto the stage (Fig. 6.2a). The printing distance, i.e. the distance from the print-head to the substrate, was kept constant at approximately 5.0 mm for both systems. The stages were operated by stepper motors and controlled by the GRBL protocol. In brief, the GRBL code transforms a digital structure into coordinates and a series of orders that control the motion of the stepper motors and trigger the jetting of the print-head. The jetting trigger activates (gated mode) the pulse generation signal that is sent to the speaker to print on demand. The GRBL properties, stepper speed, and printing frequency were adjusted to obtain a placement resolution below $\sim$300 μm. Both meniscus controllers were set to a negative pressure in the range of 8.0 - 9.0 mmH_2O to keep the meniscus pinned at the nozzle and avoid flooding.

The following procedure was followed for printing; Initial loading of print-head and syringe followed by adjusting the backpressure. The driving signal for droplet formation was adjusted in terms of pulse duration and amplitude for each ink composition. The printing speed and frequency could be adjusted for each ink and system so that adjacent droplets could coalesce on the substrate and form a continuous line, or form a string of equally spaced separated droplets. Two-dimensional patterns were created by controllably printing on the substrate, and three-dimensional

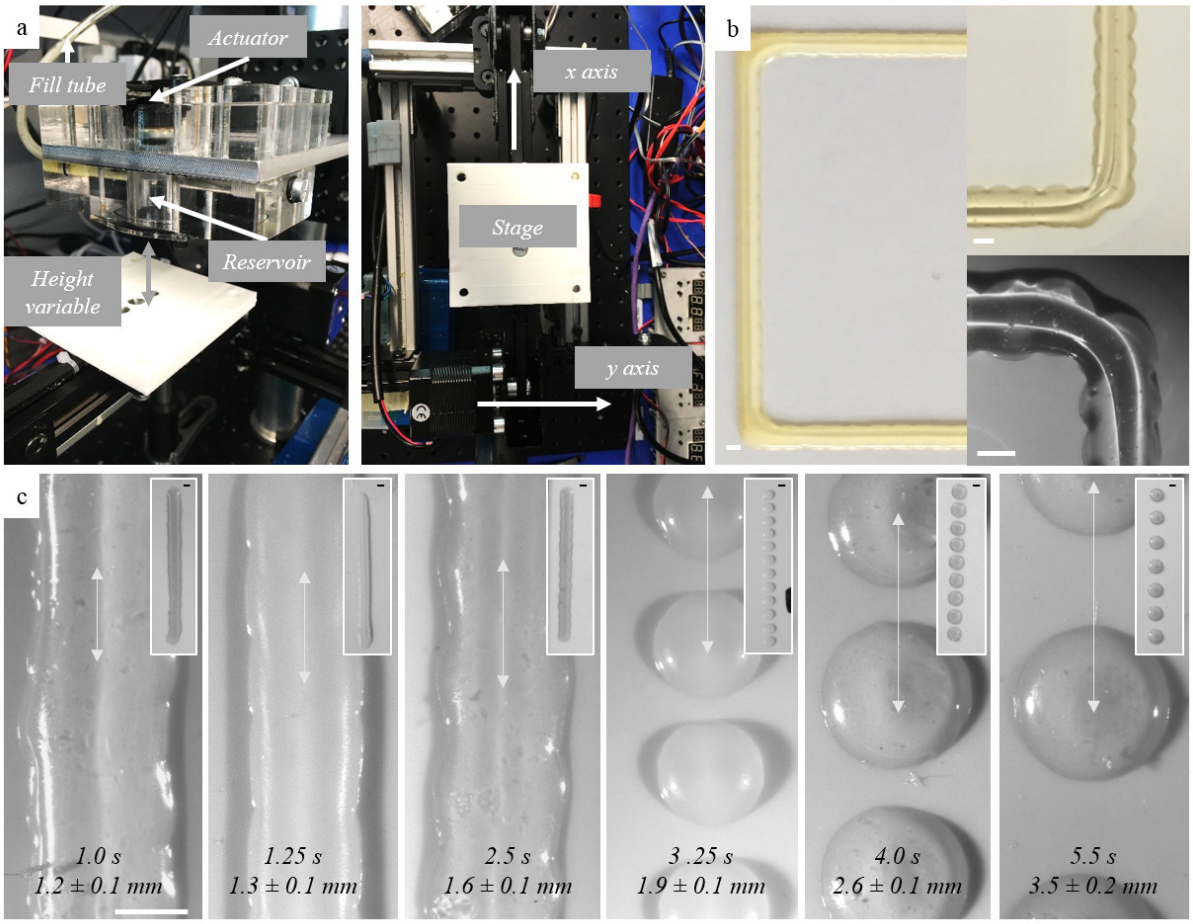

Figure 6.2: Printing with liquid latex. (a) The experimental setup showing the Grbl controlled stage and the print-head support (the 9 mL reservoir print-head is shown); (b) an example of a single layer structure made from pure liquid latex, using a droplet interval of 2.5 s with two close-ups of the corner resolution; (c) varying the droplet interval keeping the pulse signal and nozzle diameter constant: from left to right increasing the interval length from 1.0 to 5.5 s (inserts show bird-eye perspective). All scale bars 1 mm..

constructs were attempted by overlaying consecutive printing layers. Two methods of drying were tested, i) ambient air curing (where individual 1.0 mm width layers take up to 4 min to solidify) and ii) blowing hot air ($\approx$ 400 C from a 2.3 W heat gun) onto the individual print layers for 10 s to achieve curing of the pattern surface.

6.2.3 Material Characterisation

Air dried constructs and ink samples were imaged using standard bright field microscopy from Leica Instruments, USA (Leica MZ12.5 Stereomicroscope with an external light source Leica CLS150X). All standard microscopy images were analysed using the software ImageJ, with at least five measurements taken per determined value (for example construct and droplet dimensions).

An indentation test was run on cast samples (Fig. 6.3e) containing varying concentrations of MRP (0, 5, 9 and 16 wt. %) to determine the effects of rubber on the material stiffness. Three different samples per concentration were tested, with 3 tests on each sample. The Young's modulus, E, was derived from the resulting force-displacement data. Tensile testing was carried out on printed pure liquid latex samples (1 layer and 4 layers), as well as on cast latex samples containing varying amounts of MRP (0, 5, 9 and 16 wt. %). All samples tested were of a rectangular shape. The experiments were carried out on an Instron 5566 UTM with a $\pm$ 100N static load cell and a constant strain rate of 30 min^{-1}. The tensile stress and strain at the breaking point were determined from the data, as well as the Young's modulus. A minimum of 2 samples were tested per concentration. Statistical analysis was carried out using the software GraphPad Prism 5. A one-way analysis variance (ANOVA) was used, and a statistical significance was accepted when $p \leq 0.05$.

6.3 Results and Discussion

6.3.1 Inkjet printing with liquid latex

Initial tests were focused on establishing reliable printing conditions with pure liquid latex, evaluated in terms of droplet formation and reproducibility, as well as jetting

stability over time. Pulse signals were adjusted by changing the pulse width and voltage, to obtain fully formed droplets and avoid satellite droplets [153]. Conical nozzles were used in both printing systems, leading to droplets of uniform size both in-flight and post impact. We have previously shown that our systems can produce droplet impacting speeds in the range of 0.5-2.0 m s^{-1}, where droplet creation was dependent on the ink properties, the nozzle geometry, and the signal voltage and width [154]. Repetition rates were restricted by the nozzle re-filling time, i.e. the time taken by the meniscus controller and surface tension to "fill" the missing/jetted liquid at the reservoir. Given the high viscosity of the liquid latex, a droplet deposition rate (linear printing speed) of 0.15 cm s^{-1} was used. Our results indicate that, under our conditions, latex droplets produce a footprint of twice its original diameter, i.e. a droplet from a 1.0 mm nozzle produces a circular dot footprint of a 2.2 ± 0.9 mm diameter. Within a range, the droplet size can be adjusted by modifying the pressure pulse width and amplitude, without having to change the nozzle diameter. Both print-heads were shown to be capable of jetting pure liquid latex, obtaining consistent jetting with liquid latex containing 60 wt. % solid content and of relatively high viscosity (21.8 ± 0.2 mPa s). In conventional DoD printing, often a critical droplet spacing is defined by which the droplets are close enough to coalesce forming a parallel sided line. Above and below the critical spacing, either bulging of the line or no coalescence occurs respectively [109]. Figure 6.2b shows the range of droplet intervals tested, keeping the motor speed and nozzle diameter constant. As evident, the deposited latex droplets remain isolated (un-coalesced) at droplet jetting intervals greater than 2.5 s, whilst reducing the interval to ≤ 2.5 s leads to droplet coalescence and path formation. At smaller droplet jetting intervals, the increased overlap leads to instability and bulging. Figure 6.2c shows the left-side of a square pattern fabricated with the larger print-head and using a droplet jetting interval of < 2.5 s. These vertical and horizontal lines demonstrate the accuracy and stability of the print. The two close-ups seen in Fig. 6.2c show examples of the achievable resolution at the corners. Printing at corners was controlled by adding a gap at the turning point to minimise bulging from the potential three-way droplet

coalescence, i.e. the corner droplet, and the neighbouring droplets in the horizontal and vertical direction. Curing at the nozzle is an important limitation for inkjet printing. Whilst a small nozzle is desired to produce small drop sizes that dry fast, a small sessile meniscus can cure itself at the print-head during idle times. In fact, the curing of latex at the meniscus, and so the blocking of the nozzle, occurs within minutes, stopping printing. In our experiments, cleaning the nozzle plate with a fibre-free swab was sufficient to unblock the meniscus.

6.3.2 Colloidal constructs and inks

In AM, a degree of versatility in the ink composition is often needed to meet end product specifications. Ink formulation normally rely on the addition of solid particles to alter the properties of the end product, such as reinforce the material strength and durability, or to add colour using pigments. Restrictions in solid particle loading is a well-known problem in inkjet technology, with conventional printing inks only containing < 10 wt. % solid residue [144]. Having already shown that the developed system is capable of printing with pure liquid latex of a high solid content, the next step was to prove the feasibility of printing with a suspension of undiluted liquid latex with the addition of either parlon powder or MRP (colloidal ink suspension). The test was designed to include MRP made from end-of-life tire waste. MRP is a heterogeneous mixture of rubber, and is comparatively crude. As such, preliminary experiments were carried out using fine parlon powder, which has a very narrow size distribution, and an average particle size in the nanometre range. Colloidal ink suspensions of 3.5 and 6.7 wt. % parlon powder were prepared and tested in the print-head. In both instances, consistent jetting was observed (example shown in Fig. 6.3a). The printing of the rubber particle and latex ink was demonstrated by jetting a series of defined arrays, as seen in Fig. 6.3a,d. The parlon powder remained suspended in solution throughout the duration of printing, as observed through the printed droplets. The quality of the parlon distribution post printing was analysed using microscopy imagining. The parlon powder was shown to aggregate in the suspension (Fig. 6.3b-c) leading to a non-uniform size distribution of the

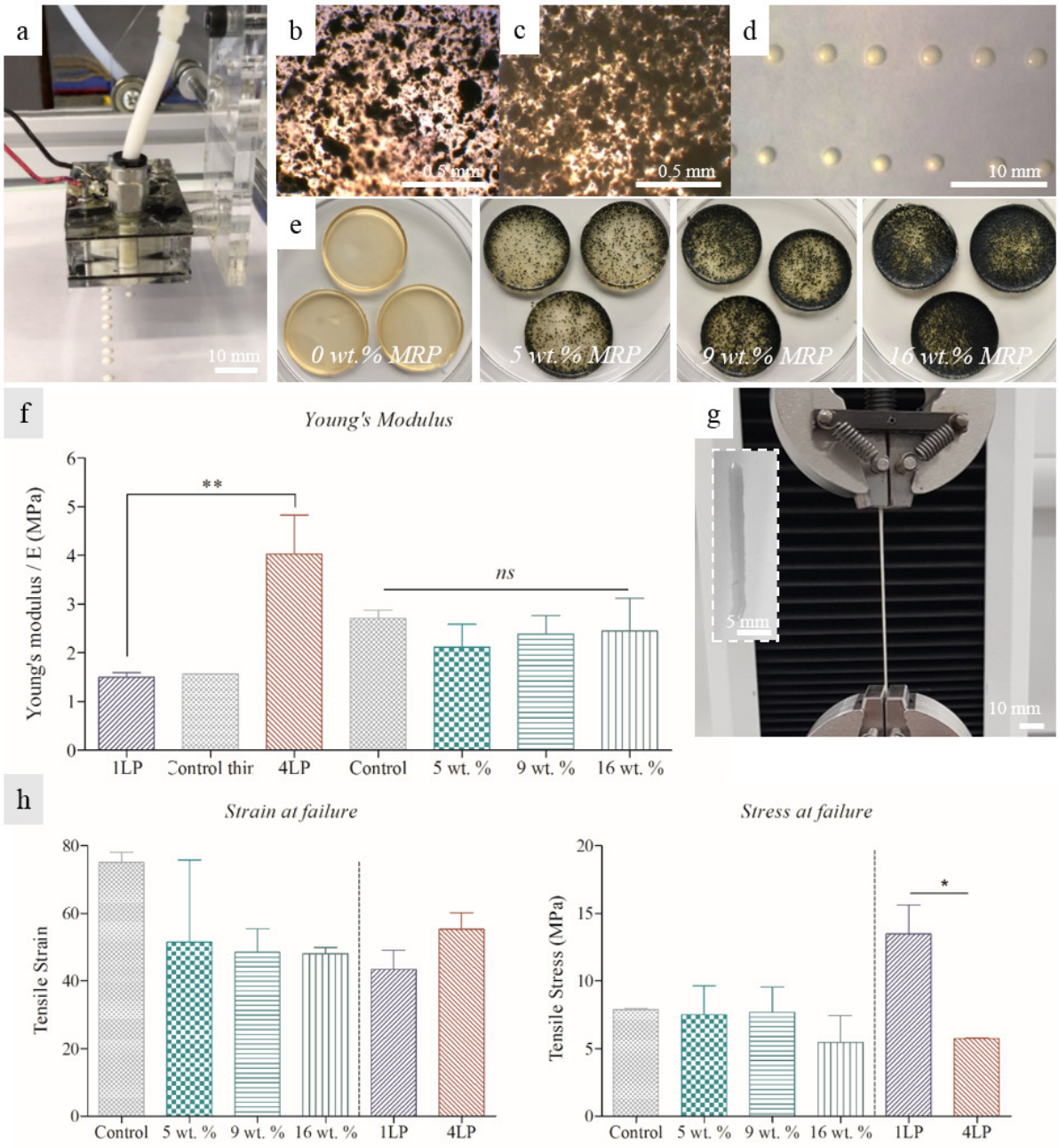

Figure 6.3: Liquid latex with rubber particle loading. (a) the print-head mounted to a $x-y$ stage, jetting pure liquid latex (1 drop/1.5 s). (b) microscopy images of liquid latex with 3.5 wt. % and (c) 6.7 wt. % parlon loading; (d) a defined array made by jetting liquid latex containing 6.7 wt. % parlon powder; (e) cast rubber samples of pure liquid latex and with increasing MRP loading (5, 9, and 16 wt. %); (f) a graph of Young's Modulus, determined using indentation and tensile testing, of cast samples with 5, 9, and 16 wt. % MRP (control; 0 wt. % MRP), and printed samples of one and four layers (1LP and 4LP, respectively) (control thin: a pure latex cast). Data reported as mean – standard deviation; (g) example of elongation of a one layer printed sample (1LP) under a constant strain tensile test (insert: original sample) and (h) tensile stress and strain at breaking point, derived from the constant tensile strain experiments ($p < 0.05$). Data reported as mean ± standard deviation. MRP, micronized rubber powder.

suspended particles. However, the parlon was well-distributed within the ink, such that all droplets contain a homogenous mixture of liquid latex and parlon powder. Having shown that a solid loading of fine rubber powder is feasible, our experiments then focused on the jetting of coarse recycled MRP, which is of greater commercial interest due to its recycling potential. The MRP used has an average particle size of 0.6 mm, comparatively larger than the parlon powder but with a narrow size distribution. The parlon powder experiments were repeated using a 9.6 wt. % MRP particle loading. A uniform droplet size was observed throughout each print, although unlike parlon powder, a non-homogenous distribution of MRP was visible post curing. Solid tire rubber could be clearly visualised in 90 % of the droplets. The non-uniform distribution of MRP can be attributed to two factors; the MRP tended to aggregate in solution creating large clusters, and secondly, due to the weight of coarse MRP they were prone to settle on the bottom of the print-head. This issue is common to all colloidal ink suspensions, and not a property specific to the liquid latex system. In fact, many commercially available print-heads continuously recirculate the ink within the print-head to avoid aggregation and clogging the nozzles [155, 156]. Implementing a more defined and rigours mixing procedure within the printer or using smaller particles [142], could mitigate agglomeration of the particles in solution as well as reducing the observed settling in the print-head. Alternatively, gentle vibration of the print-head reservoir could be introduced.

The impact on the mechanical properties was tested for a range of MRP particle loadings. Samples were prepared using casting, as shown in Fig. 6.3e, with a range of 0 to 16 wt. % MRP solid content. The samples were tested by the standard indentation and constant strain tensile tests. The two experimental methods yielded comparative values for the Young's Modulus (the overall mean $\pm$ standard deviation are reported in Table 1). The results indicate that the stiffness of these materials are not greatly affected by the colloid content, and any differences are within error of each other and not statistically significant (Fig. 6.3f). However, the tensile test indicates that adding MRP to the latex reduces the maximum elongation length from 750% to 480% (Fig. 6.3h, strain graph. The ultimate tensile stress (stress at the

breaking point) was found to be equal, within error, for all 4 sample types (Fig. 6.3h, stress graph). Having determined the impact of MRP on the mechanical properties, next the effect of printing was tested. Two types of printed pure liquid latex samples were tested, namely, a one layer (1LP) and a four layer (4LP) printed rectangles. The stress-strain plots are shown in Fig. 6.4. An example of the one layer print being tested is shown in Fig. 6.3g. Firstly, in terms of stiffness a higher Young's modulus was observed in the case of four layers compared with one layer. However, in both instances the printed samples yield similar Young's modulus to the cast controls. The one layer printed line (Figs. 6.3g and 6.3h) was elongated by $434 \pm 60\%$ prior to breaking, whereas the 4 layer printed line (4 layers printed overlaying each other) was elongated by $553 \pm 50\%$ (Fig. 6.3h). The one layer print showed a higher ultimate tensile stress compared to the 4 layer print (statistically significant). Overall, we can conclude the droplet-to-droplet and layer-to-layer bonding in the printing do not significantly change the mechanical properties of the latex, however there is a clear dependency on sample thickness as seen in the difference of the ultimate tensile stress. Combining these results, we infer that the effect of MRP particles in latex reduces the elasticity without affecting the stiffness of the printed samples. This is in line with other works, such as Mueller et al. in 2017, that have established that the global and local mechanical properties of inkjet manufactured parts can be affected in manufactured mixed-materials parts [157]. We have demonstrated the ability to print high solid content latex and with suspended recycled rubber, which from an AM perspective brings new possibilities to the recycling potential of rubber tire waste.

6.3.3 Transition to three-dimensional objects

Having shown that it is possible to print reliably with liquid latex as well as a colloidal ink, along with the added material benefits, next the possibility of creating three-dimensional objects was explored. Initially precision and resolution of the system were determined. In the first instance, pure liquid latex was used. The first patterns created were circles with a diameter of 22 mm (Fig. 6.5a-b), with

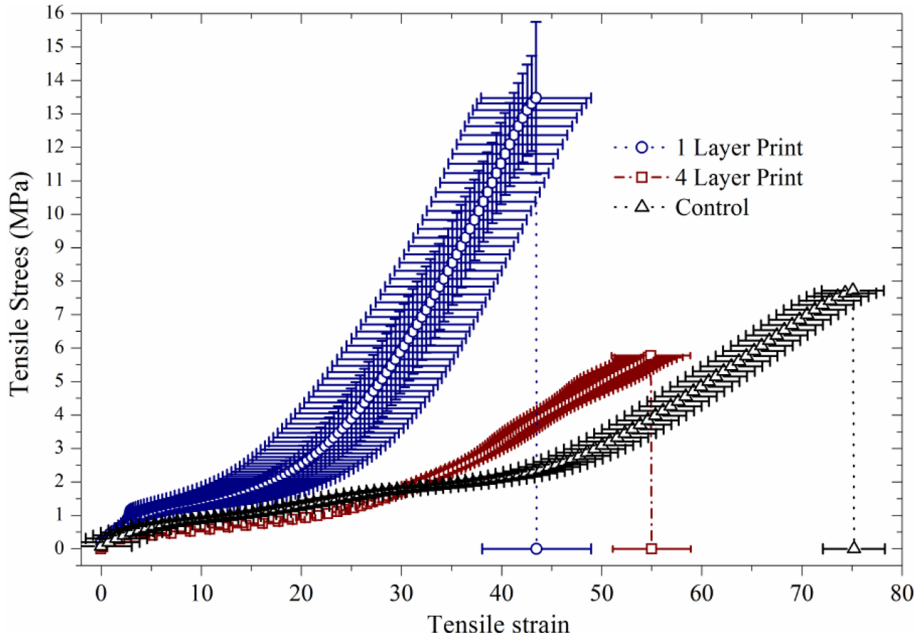

Figure 6.4: The stress–strain plot for the samples "one layer print (1LP)," "four layer print (4LP)" and "control" (pure latex). All data points are reported as the mean – standard deviation.

a droplet interval of 2.5 s to produce a continuous string formation.As previously described, two approaches to drying were tested; firstly, drying under ambient air conditions resulting in 4 min drying time for a 1.0 mm width layer. The second method consisted in blowing hot air (≈ 400 C) onto the individual print layers for 10 s to achieve a fast curing of the pattern surface. Three consecutive layers were completed with intermittent hot air blowing allowing each layer to dry the last layer before applying the next layer. The print resolution was reduced with increasing layers as evident by the increase in width. This can, for example, be seen in Fig. 6.5a-b, where the wall thickness of the circular pattern increases from 1.7 ± 0.2 mm at layer 1, to 2.6 ± 0.2 mm at layer 3. This effect is also the result of the drying/curing speed as the droplet cures into a spherical cap and not as a pancake shape as in other applications of 3D printing. However, the initial couple of layers retain the precision of the coordinated stage movement and droplet formation, showing that high resolution is achievable. Connecting interfaces were visualised using bright field microscopy. Individual droplets were clearly visualised, showing the layered structure of droplets in the constructs, originating from stepwise layering (Fig. 6.5c). Increasing the speed of drying between layers would increase the resolution retention. A star pattern (Fig. 6.5d) was made using a 100 mg

mL $^{-1}$ (9.6 wt. %) MRP suspension. The construct thickness measured 1.9 $\pm$ 0.4 mm and was made from 15 overlaying layers (Fig. 6.5f). Droplets were in this instance placed adjacent, but not overlapping in an attempt to mitigate the pronounced bulging instability as observed with increasing layers [158]. Post drying the construct revealed an increased aggregation of MRP particles in the pattern, visible as distinctive black patches (Fig. 6.5d-e). At the corners (Fig. 6.5e), the printing resolution also decreases going from an angle of 42 $\pm$ 2 degrees to 52 $\pm$ 3 degrees, meaning that sharpness of each corner is decreased with increasing layers.

Lastly, more complex one-pass printing patterns were attempted using pure liquid latex. Fig. 6.5g-h demonstrate the ability of our technique to create more complex structures, whilst retaining good placement resolution. Zooming in on the connection points (Fig. 6.5h) evidence that whilst a clearly defined three-way corner is possible (top and bottom left), bulging can still occur from three-way coalescence. Further fine-tuning of the meshing GRBL/G-code instructions at the corners can remove this problem by reducing jetting at the corners. Whilst the fluid properties and curing mechanisms require further development to decrease the time of solidification, our results show that single or few layers printing is achievable.

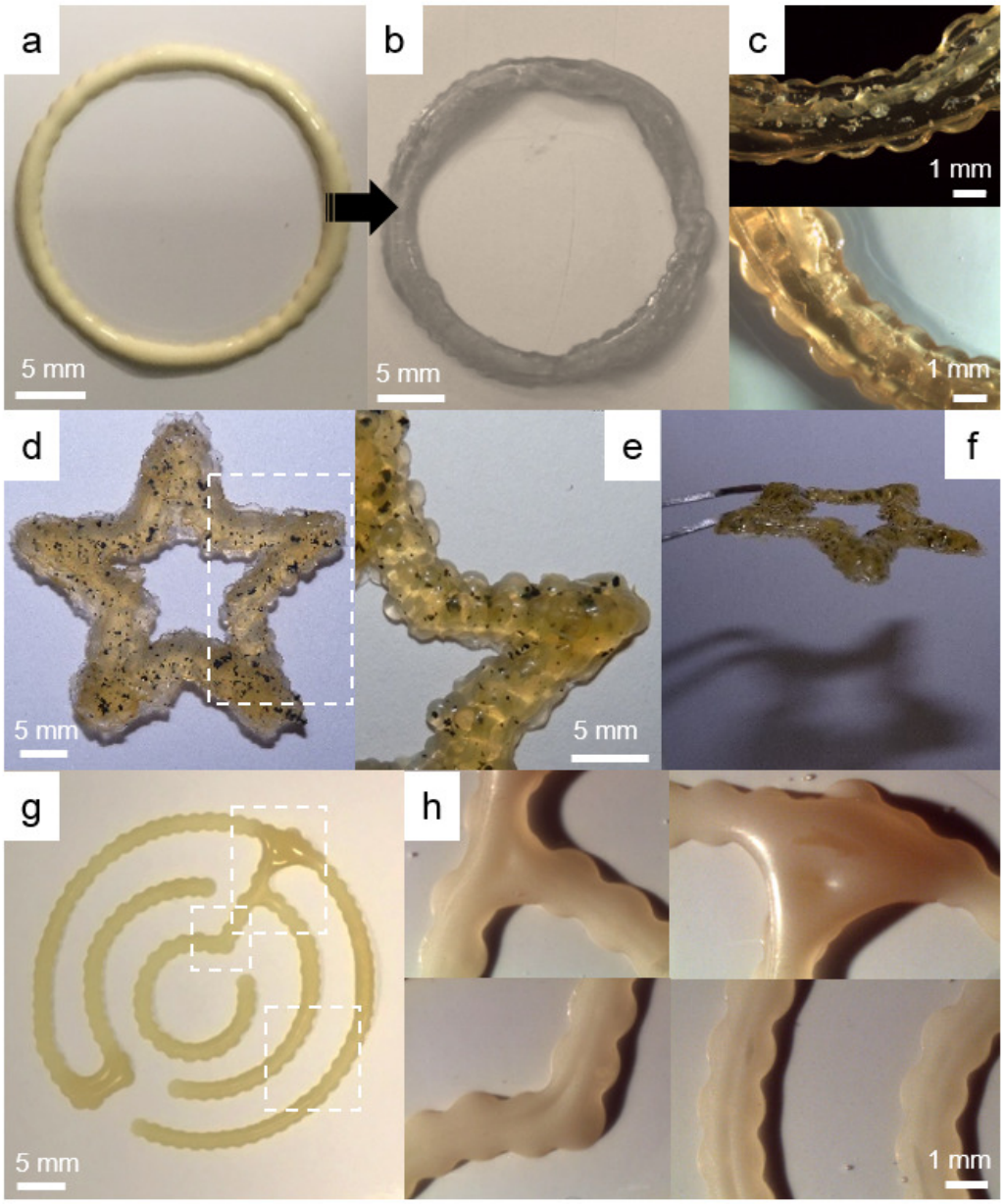

Figure 6.5: Three-dimensional latex constructs. (a) Three layers of pure liquid latex in wet and (b) dry state, with (c) close-ups of the layer structure; (d) a three-dimensional star construct made from liquid latex with 100 mg/mL (9.6 wt. %) MRP, with (e) close-up of the dotted area in d and (f) a side view; (g) a more complex one layer structure made from pure liquid latex and (h) close-ups of the dotted areas in g showing the corners and line width.

6.4 Conclusions

In this section, we have introduced an inkjet based AM process capable of printing liquid latex with of up to 60 wt. % solid content and a liquid viscosity of 21.8 ± 0.2 mPa s, both significantly higher than previous printing methods. Moreover, this system is able to print with a mixture of liquid latex and tire rubber particles of 0.5 times the nozzle diameter. Multiple layer objects were fabricated with both pure liquid latex as well as with liquid latex with the addition of MRP. The Young's modulus as well as the strain at the breaking point showed no change when adding the MRP, while maximum elongation length is reduced. Moreover, the printing process does not affect the Young's modulus of the objects. The capability of printing with a high particle loading (high solid content latex with the addition of parlon powder or MRP) and a heterogeneous particle size distribution, shows that the print-head design can operate in a wide range of solid particle loadings. This is a great advance, as most conventional inkjet-based 3D printers cannot operate with viscous liquids or liquids with solid particle loading. The study has demonstrated the potential of AM with liquid latex, however there is still scope for improvement. For example, the drying time of the liquid latex should be shortened further, by for example including a heating source in the stage or in the printing bed. Improvement of the stage and pattern control would enhance the resolution and reliability of the print quality. A reliable method of AM with liquid latex would bring great merits to the industry, by reducing cost of manufacturing (no moulds needed), and adding an unprecedented degree of flexibility in the manufacturing process. Moreover, the study has highlighted a novel method of recycling end-of-life tires. With this work, it is foreseeable that in the future we can create 3D printed objects with rubber tire waste, expanding the current recycling and waste management methods.

This thesis has focused on the interaction of liquid droplets on solid substrates with different characteristics. In particular, we have described the droplet impact dynamics on solid substrates and textiles with different properties. Moreover, in this chapter we presented an application to the droplet impact dynamics and remarked its importance in DoD 3D printing. In particular, we showed that, for the creation

of straight lines, droplet dynamics are extremely important. For example, for the printing of straight lines, if droplets coalesce too close from each other, an instability occurs, distorting the printed line. In contrast, if droplets impact far away from each other, they may not coalesce and the line would not form. In the next and last chapter of this thesis (Chapter 7), we summarise the results obtained in this thesis and suggest future work based on limitations of our research.

Chapter 7

Conclusions and Future Perspectives

This chapter summarises the overall findings. The chapter includes a perspective on the significance of the work, and suggestions for future work based on the limitations of the study.

7.1 Summary of contributions

For this thesis, I experimentally investigated droplet impact on solid and porous substrates with different properties. The substrates ranged from hydrophilic to superhydrophobic, and from smooth to rough. As part of my work, I used simple theoretical models to characterise the experimental data and to predict the impact outcome. Furthermore, I explored the application of this phenomenon to develop the first (to the best of our knowledge) liquid latex 3D printer. The main results are summarised in this section.

First, in Chapter 2, I further developed an automated MATLAB algorithm that can extract the impact velocity, size of a jetted droplet bound to impact a substrate, and the spreading diameter and contact angle from high-speed imaging frames. The MATLAB algorithm uses a polynomial fitting around the contact line to calculate the contact angle. In Chapter 2, I carried out a parametric study of the droplet parameters and the polynomial affecting measure the contact angle. The study showed that, for the four stages of droplet impact investigated in this thesis, a second order polynomial fit is the most reliable and stable (Fig. 2.8). In addition, an optimal number of pixels to adjust the polynomial is necessary (Fig. 2.6), 30 pixels for the experiments in this thesis. Moreover, our results highlight the importance of measuring the contact angle as close as possible to the contact line (Fig. 2.9). Secondly, I studied the contact line dynamics on solid substrates with different wettabilities in Chapters 3 and 4. I concluded that the maximum spreading diameter is influenced by the wettability of the substrate and the Weber number (Fig. 3.8). For impact velocities of approximately 1.0 m/s, we found three characteristic behaviours of the contact line dynamics in terms of the contact line speed (Fig. 4.3). For the hydrophilic substrates, I observed an asymptotic contact angle that kept decreasing until $u_{cl} = 0.0$ m/s and no receding was observed. For the hydrophobic surfaces, I observed asymptotic advancing and receding angles with the contact angle hysteresis shown at $u_{cl} = 0.0$ m/s. For superhydrophobic surfaces the contact angle is almost constant during spreading and receding, only varying when the droplet is about to bounce. Furthermore, we used the asymptotic contact angle, the substrate rough-

ness properties and the splashing ratio to predict the transition from no splashing to splashing (Fig. 4.17).

Thirdly, Chapter5 studies the contact line dynamics of droplets impacting on textiles. We showed that the contact line dynamics on textiles with a solid fraction larger than 66% is almost identical to the contact line dynamics on solid substrates. In contrast, substrates with solid fraction less than 66%, the maximum spreading diameter deviates from the scaling law for solid substrates due to leaking. Additionally, we found that for all textiles at early times ($t^* < 0.1$) the droplet is not deformed and no lamella is generated, in contrast to solid substrates (Figs. 5.4 and 5.5). Furthermore, by doing a balance between kinetic and capillary pressures, we found scaling arguments that separate the complete penetration from the partial penetration regimes (Eq. 5.5 and Fig. 5.7).

Finally, I used a DoD system to create 3D latex structures. The printhead was based on the DoD design described in Chapter 2 and was mounted in a two-dimensional stage (Fig. 6.2). The 3D constructs were formed by depositing a continuous line of droplets, which are left to cure, and then by the subsequent printing of layers on top. I optimised the frequency of the deposition and the movement of the droplets so straight lines could be printed without bulking (Fig. 6.2 c). Furthermore, I did mechanical testing analysis and proved that the printing process does not affect the material properties of the cured latex, even when loaded with solid rubber particles (Fig. 6.3). The first (to the best of my knowledge) 3D printed latex structures are shown in Fig. 6.5. This is the first step to broaden the choice of materials for 3D printing, which are normally constrained to cured liquids or absorbing substrates.

7.2 Future Work

The results presented in this thesis have advanced our understanding of droplet impact and contact line dynamics. However, the droplet impact phenomena is extremely rich and new questions remain unanswered.

In our experiments, low surface tension liquids always spread at low contact

angles. Consequently, superamphipbhobic substrates would allow the study of low surface tension liquids spreading dynamics at large contact angles ($\theta_{DA} > 100$ degrees). This information would complement our spreading experiments and complete the splashing map presented in Chapter 4, Fig. 4.10.

Previous studies have found that splashing for both, smooth and rough substrates is suppressed at low ambient pressures [62]. Additionally, our results show that splashing is promoted by high dynamic contact angles. Consequently, it would be interesting to investigate the contact angle dynamics at reduced ambient pressures. Our hypothesis is that θ_{max} decreases, with decreasing ambient pressure.

Droplet splashing on solid substrates is commonly classified as corona and prompt splashing. However, there is no precise definition or a standard criterion to differentiate them. Consequently, a thorough study is required to further understand their differences. For that, faster recording speeds and better spatial resolution would be required. A two camera system would be useful too, one looking close to the impact point, to detect small and fast drops and the ejection of the thin sheet (if created), and another view to look at the overall spreading process to detect any secondary droplets that may have been ejected at later times.

Regarding textiles, this work just explored the impact onto *rigid* single layer textiles. In practice, e.g., in clothes, textiles can bend and are formed of several textile layers. Therefore, the influence of textile deformation on the penetration threshold would be interesting to explore. This could be done within our existing setup, by varying the extensile force applied to the textile. Additionally, the influence of various textile layers and emulate a piece of clothing could be studied by superposing two or more single textile layers. The superposition of the textiles can be varied in a way that the pores centres are completely aligned, or offset by a given controlled distance. Furthermore, as clothes are not always positioned horizontally with respect to rain, a further study could consist on study the contact line dynamics of a droplet impacting onto an inclined textile. The experiments would consist in placing the stretching device on a tilting platform.

Finally, the latex 3D printer is just a proof of concept. There are still issues to

solve or improve. The drying and curing of the droplets needs to be better controlled. This could be done either by controlling the temperature of both the liquid (ink) at the printhead and the substrate; or with a continuous dry air blowing system. Additionally, a further study of the contact line dynamics of liquid latex droplets impacting dried latex droplets would help us understand the underlying process of additive manufacturing by inkjet processes.

Appendix A

Error propagation in the measurement of the Weber and Reynolds numbers

The Reynolds and Weber numbers are used throughout the thesis to measure the importance between inertia and viscous forces and inertia and surface tension. Given the importance of this numbers, we have included an estimated error for this quantities. All the involved quantities for calculating the Reynolds and Weber numbers were measured at the laboratory. In general, to find the uncertainty δq, of $q = x + y$, we can think of the maximum and minimum values that q can take. The maximum/minimum value is obtained when the values of x and y take their maximum/minimum value within the measured uncertainty, i.e. $q = x+y+(\delta x+\delta y)/q = x + y - (\delta x + \delta y)$. Therfore the value of q will be always between this two values and $\delta q = \delta x + \delta y$. In general, if $q = x_1 + x_2 + ...x_n$ and $\delta q = \delta x_1 + \delta x_2 + ...\delta x_n$. Correspondingly, for quotients and products if $q = \frac{x_1 x_2 ... x_n}{y_1 y_2 ... y_n}$ then,

$$\frac{\delta q}{|q|} = \frac{\delta x_1}{|x_1|} + ... + \frac{\delta x_n}{|x_n|} + \frac{\delta y_1}{|y_1|} + ... + \frac{\delta y_n}{|y_n|} \tag{A.1}$$

However, eq. A.1 overestimate the error for quantities that are independent and random. Therefore if measurement errors follow a Gaussian distribution, adding the quadrature is a better approximation to the error, that is,

$$\frac{\delta q}{|q|} = \sqrt{\left(\frac{\delta x_1}{|x_1|}\right)^2 + ... + \left(\frac{\delta x_n}{|x_n|}\right)^2 + \left(\frac{\delta y_1}{|y_1|}\right)^2 + ... + \left(\frac{\delta y_n}{|y_n|}\right)^2} \tag{A.2}$$

As shown in Chapter 2, the associated errors of the measured viscosity, surface

tension and density are ± 0.0001 Pa s, ± 0.5 mN/m and 1 kg/m^3. Additionally spatial resolution of the system is 6.47 ± 0.13 μm per pixel. Considering an error of ± 2 pixels when measuring the diameter of the droplets D_0 then $\delta D_0 = \pm 13.2$ μm. Additionally, U0 is calculated by doing a linear regression over time of the droplet position prior impact. In our experiments, the resolution in time and space is in the order of milliseconds and micrometers and the impact speed is in the order of m/s. Therefore, we take the associated error to the slope as the error in U_0. In our experiments the error was found to be $\delta U_0 \sim 0.005$ m/s for $U_0 \sim 1$ m/s and $U_0 \sim 0.02$ for $U_0 \sim 4$ m/s.

The typical values of the viscosity, surface tension, density, droplet diameter and impact velocity are: $\mu \sim 1$ mPa s, $\sigma \sim 50$ mN/m, $\rho \sim 1000$, $D_0 \sim 1$mm and $U_0 \sim 1$ m/s. These values lead to typical Reynolds $Re \sim 1000$ Weber $We \sim 20$ numbers. Therefore, the associated error with the Reynolds number is $\delta Re \sim 100$ and for the Weber number $\delta We \sim 0.2$. For the largest values of the impact velocity used in the thesis $U_0 \sim 5$ m/s (Re ~ 5000, We ~ 500) the error associated to the Reynolds and Weber numbers are $\delta Re \sim 500$ and $\delta We \sim 15$. In conclusion, the largest percentage error associated with the calculated Reynolds and Weber numbers are $\sim 10\%$ and $\sim 3\%$ respectively.

Bibliography

[1] AM Worthington. *The splash of a drop*, volume 27125. Society for Promoting Christian Knowledge, 1895.

[2] R Rioboo, C Tropea, and M Marengo. Outcomes from a drop impact on solid surfaces. *Atomization and Sprays*, 11(2), 2001.

[3] L Xu, WW Zhang, and SR Nagel. Drop splashing on a dry smooth surface. *Physical review letters*, 94(18):184505, 2005.

[4] CJ Howland, A Antkowiak, JR Castrejón-Pita, SD Howison, JM Oliver, RW Style, and AA Castrejón-Pita. It's harder to splash on soft solids. *Physical review letters*, 117(18):184502, 2016.

[5] AL Yarin. Drop impact dynamics: splashing, spreading, receding, bouncing.... *Annu. Rev. Fluid Mech.*, 38:159–192, 2006.

[6] V Bergeron, D Bonn, Jean Y Martin, and L Vovelle. Controlling droplet deposition with polymer additives. *Nature*, 405(6788):772, 2000.

[7] HB Eral, DJCM 't Mannetje, and JM Oh. Contact angle hysteresis: a review of fundamentals and applications. *Colloid and polymer science*, 291(2):247–260, 2013.

[8] JF Joanny and P-G De Gennes. A model for contact angle hysteresis. *The journal of chemical physics*, 81(1):552–562, 1984.

[9] L Chen. *Dynamic Wetting by Viscous Liquids: Effects of Softness, Wettability and Curvature of the Substrate and Influence of External Electric Fields*. PhD thesis, University of Darmstadt, 2013.

[10] Y Yuan and TR Lee. Contact angle and wetting properties. In *Surface science techniques*, pages 3–34. Springer, 2013.

[11] D Bonn, J Eggers, J Indekeu, J Meunier, and E Rolley. Wetting and spreading. *Reviews of modern physics*, 81(2):739, 2009.

[12] RJ Good. Contact angle, wetting, and adhesion: a critical review. *Journal of adhesion science and technology*, 6(12):1269–1302, 1992.

[13] A Marmur. Thermodynamic aspects of contact angle hysteresis. *Advances in colloid and interface science*, 50:121–141, 1994.

[14] Š Šikalo, H-D Wilhelm, IV Roisman, S Jakirlić, and C Tropea. Dynamic contact angle of spreading droplets: Experiments and simulations. *Physics of Fluids*, 17(6):062103, 2005.

[15] CW Extrand and Y Kumagai. An experimental study of contact angle hysteresis. *Journal of Colloid and Interface Science*, 191(2):378–383, 1997.

[16] RN Wenzel. Resistance of solid surfaces to wetting by water. *Industrial & Engineering Chemistry*, 28(8):988–994, 1936.

[17] ABD Cassie and S Baxter. Wettability of porous surfaces. *Transactions of the Faraday society*, 40:546–551, 1944.

[18] V Belaud, S Valette, G Stremsdoerfer, M Bigerelle, and S Benayoun. Wettability versus roughness: multi-scales approach. *Tribology International*, 82:343–349, 2015.

[19] B He, J Lee, and NA Patankar. Contact angle hysteresis on rough hydrophobic surfaces. *Colloids and Surfaces A: Physicochemical and Engineering Aspects*, 248(1-3):101–104, 2004.

[20] NA Patankar. On the modeling of hydrophobic contact angles on rough surfaces. *Langmuir*, 19(4):1249–1253, 2003.

[21] D Bartolo, F Bouamrirene, E Verneuil, A Buguin, P Silberzan, and S Moulinet. Bouncing or sticky droplets: Impalement transitions on superhydrophobic micropatterned surfaces. *EPL (Europhysics Letters)*, 74(2):299, 2006.

[22] M Reyssat, A Pépin, F Marty, Y Chen, and D Quéré. Bouncing transitions on microtextured materials. *EPL (Europhysics Letters)*, 74(2):306, 2006.

[23] E Pierce, FJ Carmona, and A Amirfazli. Understanding of sliding and contact angle results in tilted plate experiments. *Colloids and Surfaces A: Physicochemical and Engineering Aspects*, 323(1):73–82, 2008.

[24] Y Rotenberg, L Boruvka, and AW Neumann. Determination of surface tension and contact angle from the shapes of axisymmetric fluid interfaces. *Journal of Colloid and Interface Science*, 93(1):169–183, 1983.

[25] A Bateni, SS Susnar, A Amirfazli, and AW Neumann. A high-accuracy polynomial fitting approach to determine contact angles. *Colloids and Surfaces A: Physicochemical and Engineering Aspects*, 219(1-3):215–231, 2003.

[26] G Lamour, A Hamraoui, A Buvailo, Y Xing, S Keuleyan, V Prakash, A Eftekhari-Bafrooei, and E Borguet. Contact angle measurements using a simplified experimental setup. *Journal of chemical education*, 87(12):1403–1407, 2010.

[27] JB Lee, N Laan, KG de Bruin, G Skantzaris, N Shahidzadeh, D Derome, J Carmeliet, and D Bonn. Universal rescaling of drop impact on smooth and rough surfaces. *Journal of Fluid Mechanics*, 786, 2016.

[28] JB Lee, D Derome, R Guyer, and J Carmeliet. Modeling the maximum spreading of liquid droplets impacting wetting and nonwetting surfaces. *Langmuir*, 32(5):1299–1308, 2016.

[29] D Biolè and V Bertola. A goniometric mask to measure contact angles from digital images of liquid drops. *Colloids and Surfaces A: Physicochemical and Engineering Aspects*, 467:149–156, 2015.

[30] E Atefi, JA Mann Jr, and H Tavana. A robust polynomial fitting approach for contact angle measurements. *Langmuir*, 29(19):5677–5688, 2013.

[31] JH Snoeijer and B Andreotti. Moving contact lines: scales, regimes, and dynamical transitions. *Annual Review of Fluid Mechanics*, 45, 2013.

[32] C Huh and LE Scriven. Hydrodynamic model of steady movement of a solid/liquid/fluid contact line. *Journal of Colloid and Interface Science*, 35(1):85–101, 1971.

[33] S Afkhami, S Zaleski, and M Bussmann. A mesh-dependent model for applying dynamic contact angles to VOF simulations. *Journal of Computational Physics*, 228(15):5370–5389, 2009.

[34] P-G De Gennes, F Brochard-Wyart, and D Quéré. *Capillarity and wetting phenomena: drops, bubbles, pearls, waves*. Springer Science & Business Media, 2013.

[35] OV Voinov. Hydrodynamics of wetting. *Fluid dynamics*, 11(5):714–721, 1976.

[36] PA Thompson and MO Robbins. Simulations of contact-line motion: slip and the dynamic contact angle. *Physical Review Letters*, 63(7):766, 1989.

[37] M Renardy, Y Renardy, and J Li. Numerical simulation of moving contact line problems using a volume-of-fluid method. *Journal of Computational Physics*, 171(1):243–263, 2001.

[38] S Afkhami, J Buongiorno, A Guion, S Popinet, Y Saade, R Scardovelli, and S Zaleski. Transition in a numerical model of contact line dynamics and forced dewetting. *Journal of Computational Physics*, 374:1061–1093, 2018.

[39] S Afkhami and M Bussmann. Height functions for applying contact angles to 2d vof simulations. *International journal for numerical methods in fluids*, 57(4):453–472, 2008.

[40] O Weinstein and LM Pismen. Scale dependence of contact line computations. *Mathematical Modelling of Natural Phenomena*, 3(1):98–107, 2008.

[41] K Yokoi, D Vadillo, J Hinch, and I Hutchings. Numerical studies of the influence of the dynamic contact angle on a droplet impacting on a dry surface. *Physics of Fluids*, 21(7):072102, 2009.

[42] DC Vadillo, A Soucemarianadin, C Delattre, and DCD Roux. Dynamic contact angle effects onto the maximum drop impact spreading on solid surfaces. *Physics of Fluids*, 21(12):122002, 2009.

[43] V Cristini and Y-C Tan. Theory and numerical simulation of droplet dynamics in complex flows—a review. *Lab on a Chip*, 4(4):257–264, 2004.

[44] H Liu, Y Ju, N Wang, G Xi, and Y Zhang. Lattice boltzmann modeling of contact angle and its hysteresis in two-phase flow with large viscosity difference. *Physical Review E*, 92(3):033306, 2015.

[45] J Eggers, MA Fontelos, C Josserand, and S Zaleski. Drop dynamics after impact on a solid wall: theory and simulations. *Physics of Fluids*, 22(6):062101, 2010.

[46] ST Thoroddsen, K Takehara, and TG Etoh. Bubble entrapment through topological change. *Physics of Fluids*, 22(5):051701, 2010.

[47] C Josserand and ST Thoroddsen. Drop impact on a solid surface. *Annual Review of Fluid Mechanics*, 48:365–391, 2016.

[48] R Rioboo, M Marengo, and C Tropea. Time evolution of liquid drop impact onto solid, dry surfaces. *Experiments in Fluids*, 33(1):112–124, 2002.

[49] IS Bayer and CM Megaridis. Contact angle dynamics in droplets impacting on flat surfaces with different wetting characteristics. *Journal of Fluid Mechanics*, 558:415–449, 2006.

[50] Š Šikalo, Marco Marengo, Cameron Tropea, and EN Ganić. Analysis of impact of droplets on horizontal surfaces. *Experimental thermal and fluid science*, 25(7):503–510, 2002.

[51] C Clanet, C Béguin, D Richard, and D Quéré. Maximal deformation of an impacting drop. *Journal of Fluid Mechanics*, 517:199–208, 2004.

[52] N Laan, KG de Bruin, D Bartolo, C Josserand, and D Bonn. Maximum diameter of impacting liquid droplets. *Physical Review Applied*, 2(4):044018, 2014.

[53] G Lagubeau, MA Fontelos, C Josserand, A Maurel, V Pagneux, and P Petitjeans. Spreading dynamics of drop impacts. *Journal of Fluid Mechanics*, 713:50–60, 2012.

[54] CW Visser, PE Frommhold, S Wildeman, R Mettin, D Lohse, and C Sun. Dynamics of high-speed micro-drop impact: numerical simulations and experiments at frame-to-frame times below 100 ns. *Soft Matter*, 11(9):1708–1722, 2015.

[55] SF Lunkad, VV Buwa, and KDP Nigam. Numerical simulations of drop impact and spreading on horizontal and inclined surfaces. *Chemical Engineering Science*, 62(24):7214–7224, 2007.

[56] C Antonini, A Amirfazli, and M Marengo. Drop impact and wettability: From hydrophilic to superhydrophobic surfaces. *Physics of Fluids*, 24(10):102104, 2012.

[57] JE Sprittles and YD Shikhmurzaev. Finite element simulation of dynamic wetting flows as an interface formation process. *Journal of Computational Physics*, 233:34–65, 2013.

[58] D Attinger, C Moore, A Donaldson, A Jafari, and HA Stone. Fluid dynamics topics in bloodstain pattern analysis: comparative review and research opportunities. *Forensic Science International*, 231(1-3):375–396, 2013.

[59] L Hulse-Smith, NZ Mehdizadeh, and S Chandra. Deducing drop size and impact velocity from circular bloodstains. *Journal of Forensic Science*, 50(1):JFS2003224–10, 2005.

[60] RF Allen. The role of surface tension in splashing. *Journal of Colloid and Interface Science*, 51:350–351, 1975.

[61] ST Thoroddsen and Jun Sakakibara. Evolution of the fingering pattern of an impacting drop. *Physics of fluids*, 10(6):1359–1374, 1998.

[62] A Latka, A Strandburg-Peshkin, MM Driscoll, CS Stevens, and SR Nagel. Creation of prompt and thin-sheet splashing by varying surface roughness or increasing air pressure. *Physical Review Letters*, 109:054501, Jul 2012.

[63] MM Driscoll and SR Nagel. Ultrafast interference imaging of air in splashing dynamics. *Physical Review Letters*, 107:154502, Oct 2011.

[64] J Palacios, J Hernández, P Gómez, C Zanzi, and J López. Experimental study of splashing patterns and the splashing/deposition threshold in drop impacts onto dry smooth solid surfaces. *Experimental Thermal and Fluid Science*, 44:571–582, 2013.

[65] G Riboux and JM Gordillo. Experiments of drops impacting a smooth solid surface: A model of the critical impact speed for drop splashing. *Physical review letters*, 113(2):024507, 2014.

[66] IV Roisman, A Lembach, and C Tropea. Drop splashing induced by target roughness and porosity: The size plays no role. *Advances in Colloid and Interface Science*, 222:615 – 621, 2015. Reinhard Miller, Honorary Issue.

[67] Cacey S Stevens. Scaling of the splash threshold for low-viscosity fluids. *EPL (Europhysics Letters)*, 106(2):24001, 2014.

[68] RL Vander Wal, GM Berger, and SD Mozes. The splash/non-splash boundary upon a dry surface and thin fluid film. *Experiments in fluids*, 40(1):53–59, 2006.

[69] CHR Mundo, M Sommerfeld, and C Tropea. Droplet-wall collisions: experimental studies of the deformation and breakup process. *International Journal of Multiphase Flow*, 21(2):151–173, 1995.

[70] Shreyas Mandre and Michael P Brenner. The mechanism of a splash on a dry solid surface. *Journal of Fluid Mechanics*, 690:148–172, 2012.

[71] H Almohammadi and A Amirfazli. Droplet impact: Viscosity and wettability effects on splashing. *Journal of Colloid and Interface Science*, 2019.

[72] H Almohammadi and A Amirfazli. Understanding the drop impact on moving hydrophilic and hydrophobic surfaces. *Soft Matter*, 13(10):2040–2053, 2017.

[73] CS Stevens, A Latka, and SR Nagel. Comparison of splashing in high- and low-viscosity liquids. *Phys. Rev. E*, 89:063006, Jun 2014.

[74] John M. Kolinski, L. Mahadevan, and Shmuel M. Rubinstein. Lift-off instability during the impact of a drop on a solid surface. *Physical Review Letters*, 112:134501, Apr 2014.

[75] A Latka. Thin-sheet creation and threshold pressures in drop splashing. *Soft Matter*, 13(4):740–747, 2017.

[76] Z Jian, C Josserand, S Popinet, P Ray, and S Zaleski. Two mechanisms of droplet splashing on a solid substrate. *Journal of Fluid Mechanics*, 835:1065–1086, 2018.

[77] Y Liu, P Tan, and L Xu. Kelvin–helmholtz instability in an ultrathin air film causes drop splashing on smooth surfaces. *Proceedings of the National Academy of Sciences*, 112(11):3280–3284, 2015.

[78] DA Burzynski and SE Bansmer. Role of surrounding gas in the outcome of droplet splashing. *Physical Review Fluids*, 4(7):073601, 2019.

[79] J Liu, H Vu, SS Yoon, RA Jepsen, and G Aguilar. Splashing phenomena during liquid droplet impact. *Atomization and Sprays*, 20(4), 2010.

[80] D GK Aboud and AM Kietzig. Splashing threshold of oblique droplet impacts on surfaces of various wettability. *Langmuir*, 31(36):10100–10111, 2015.

[81] S Douezan and F Brochard-Wyart. Decorating a liquid interface promotes splashing. *Langmuir*, 27(16):9955–9960, 2011.

[82] C Duez, C Ybert, C Clanet, and L Bocquet. Making a splash with water repellency. *Nature Physics*, 3(3):180, 2007.

[83] K Yokoi. Numerical studies of droplet splashing on a dry surface: triggering a splash with the dynamic contact angle. *Soft Matter*, 7(11):5120–5123, 2011.

[84] J Hao. Effect of surface roughness on droplet splashing. *Physics of Fluids*, 29(12):122105, 2017.

[85] H Nakae, R Inui, Y Hirata, and H Saito. Effects of surface roughness on wettability. *Acta Materialia*, 46(7):2313–2318, 1998.

[86] K Range and F Feuillebois. Influence of surface roughness on liquid drop impact. *Journal of Colloid and Interface Science*, 203(1):16–30, 1998.

[87] C Tang, M Qin, X Weng, X Zhang, P Zhang, J Li, and Z Huang. Dynamics of droplet impact on solid surface with different roughness. *International Journal of Multiphase Flow*, 96:56–69, 2017.

[88] V Vaikuntanathan and D Sivakumar. Maximum spreading of liquid drops impacting on groove-textured surfaces: effect of surface texture. *Langmuir*, 32(10):2399–2409, 2016.

[89] S-C Zhao, R de Jong, and D van der Meer. Liquid-grain mixing suppresses droplet spreading and splashing during impact. *Physical review letters*, 118(5):054502, 2017.

[90] Y Liu, L Moevius, X Xu, T Qian, JM Yeomans, and Z Wang. Pancake bouncing on superhydrophobic surfaces. *Nature Physics*, 10(7):515, 2014.

[91] P Tsai, S Pacheco, C Pirat, L Lefferts, and D Lohse. Drop impact upon micro- and nanostructured superhydrophobic surfaces. *Langmuir*, 25(20):12293–12298, 2009.

[92] A Lafuma and D Quéré. Superhydrophobic states. *Nature Materials*, 2(7):457, 2003.

[93] C Josserand, L Lemoyne, R Troeger, and S Zaleski. Droplet impact on a dry surface: triggering the splash with a small obstacle. *Journal of Fluid Mechanics*, 524:47–56, 2005.

[94] L Xu, L Barcos, and SR Nagel. Splashing of liquids: Interplay of surface roughness with surrounding gas. *Physical Review E*, 76(6):066311, 2007.

[95] R Zhang, P Hao, X Zhang, F Niu, and F He. Tunable droplet breakup dynamics on micropillared superhydrophobic surfaces. *Langmuir*, 34(26):7942–7950, 2018.

[96] K Connington and T Lee. Lattice boltzmann simulations of forced wetting transitions of drops on superhydrophobic surfaces. *Journal of Computational Physics*, 250:601–615, 2013.

[97] F Varnik, M Gross, N Moradi, G Zikos, P Uhlmann, P Müller-Buschbaum, D Magerl, D Raabe, I Steinbach, and M Stamm. Stability and dynamics of droplets on patterned substrates: insights from experiments and lattice boltzmann simulations. *Journal of Physics: Condensed Matter*, 23(18):184112, 2011.

[98] T Koishi, K Yasuoka, S Fujikawa, T Ebisuzaki, and XC Zeng. Coexistence and transition between cassie and wenzel state on pillared hydrophobic surface. *Proceedings of the National Academy of Sciences*, 106(21):8435–8440, 2009.

[99] É Lorenceau and D Quéré. Drops impacting a sieve. *Journal of Colloid and Interface Science*, 263(1):244–249, 2003.

[100] A Delbos, E Lorenceau, and O Pitois. Forced impregnation of a capillary tube with drop impact. *Journal of Colloid and Interface Science*, 341(1):171–177, 2010.

[101] YC Jung and B Bhushan. Dynamic effects of bouncing water droplets on superhydrophobic surfaces. *Langmuir*, 24(12):6262–6269, 2008.

[102] H Ghadiri and D Payne. Raindrop impact stress. *Journal of Soil Science*, 32(1):41–49, 1981.

[103] S Ryu, P Sen, Y Nam, and C Lee. Water penetration through a superhydrophobic mesh during a drop impact. *Physical review letters*, 118(1):014501, 2017.

[104] A Kumar, A Tripathy, Y Nam, C Lee, and P Sen. Effect of geometrical parameters on rebound of impacting droplets on leaky superhydrophobic meshes. *Soft Matter*, 14(9):1571–1580, 2018.

[105] AD Bordoloi and EK Longmire. Drop motion through a confining orifice. *Journal of Fluid Mechanics*, 759:520–545, 2014.

[106] YS Joung and CR Buie. Scaling laws for drop impingement on porous films and papers. *Physical Review E*, 89(1):013015, 2014.

[107] E Kissa. Capillary sorption in fibrous assemblies. *Journal of Colloid and Interface Science*, 83(1):265–272, 1981.

[108] G Zhang, R Parwani, CA Stone, AH Barber, and L Botto. X-ray imaging of transplanar liquid transport mechanisms in single layer textiles. *Langmuir*, 33(43):12072–12079, 2017.

[109] B Derby. Inkjet printing of functional and structural materials: fluid property requirements, feature stability, and resolution. *Annual Review of Materials Research*, 40:395–414, 2010.

[110] M Pasandideh-Fard, S Chandra, and J Mostaghimi. A three-dimensional model of droplet impact and solidification. *International Journal of Heat and Mass Transfer*, 45(11):2229–2242, 2002.

[111] M Fogliati, D Fontana, M Garbero, M Vanni, G Baldi, and R Donde. CFD simulation of paint deposition in an air spray process. *Journal of Coatings Technology and Research*, 3(2):117–125, 2006.

[112] Jens Eggers. Theory of drop formation. *Physics of Fluids*, 7(5):941–953, 1995.

[113] X Zhang and OA Basaran. An experimental study of dynamics of drop formation. *Physics of fluids*, 7(6):1184–1203, 1995.

[114] GF Scheele and BJ Meister. Drop formation at low velocities in liquid-liquid systems: Part i. prediction of drop volume. *American Institute of Chemical Engineers Journal*, 14(1):9–15, 1968.

[115] CL Hedegaard, EC Collin, C Redondo-Gómez, Luong TH Nguyen, KW Ng, AA Castrejón-Pita, JR Castrejón-Pita, and A Mata. Hydrodynamically guided hierarchical self-assembly of peptide–protein bioinks. *Advanced Functional Materials*, 28(16):1703716, 2018.

[116] Y Niimura and K Hasegawa. Evaporation of droplet in mid-air: Pure and binary droplets in single-axis acoustic levitator. *PloS One*, 14(2):e0212074, 2019.

[117] N Otsu. A threshold selection method from gray-level histograms. *IEEE Transactions on Systems, Man, and Cybernetics*, 9(1):62–66, 1979.

[118] S Farshid Chini and A Amirfazli. A method for measuring contact angle of asymmetric and symmetric drops. *Colloids and Surfaces A: Physicochemical and Engineering Aspects*, 388(1-3):29–37, 2011.

[119] FJ Montes Ruiz-Cabello, MA Rodríguez-Valverde, and M Cabrerizo-Vilchez. A new method for evaluating the most stable contact angle using tilting plate experiments. *Soft Matter*, 7(21):10457–10461, 2011.

[120] JK Park, J Ryu, BC Koo, S Lee, and KH Kang. How the change of contact angle occurs for an evaporating droplet: effect of impurity and attached water films. *Soft Matter*, 8(47):11889–11896, 2012.

[121] J San Lee, BM Weon, JH Je, and K Fezzaa. How does an air film evolve into a bubble during drop impact? *Physical Review Letters*, 109(20):204501, 2012.

[122] TC de Goede, KG de Bruin, N Shahidzadeh, and D Bonn. Predicting the maximum spreading of a liquid drop impacting on a solid surface: Effect of surface tension and entrapped air layer. *Physical Review Fluids*, 4(5):053602, 2019.

[123] J Wang, M Do-Quang, JJ Cannon, F Yue, Y Suzuki, G Amberg, and J Shiomi. Surface structure determines dynamic wetting. *Scientific Reports*, 5:8474, 2015.

[124] A Latka, A M Boelens, SR Nagel, and JJ de Pablo. Drop splashing is independent of substrate wetting. *Physics of Fluids*, 30(2):022105, 2018.

[125] AU Alam, MMR Howlader, and MJ Deen. The effects of oxygen plasma and humidity on surface roughness, water contact angle and hardness of silicon, silicon dioxide and glass. *Journal of Micromechanics and Microengineering*, 24(3):035010, 2014.

[126] P Chen, C Zhang, X Zhang, B Wang, W Li, and Q Lei. Effects of oxygen plasma treatment power on surface properties of poly (p-phenylene benzobisoxazole) fibers. *Applied Surface Science*, 255(5):3153–3158, 2008.

[127] DY Kwok, R Lin, M Mui, and AW Neumann. Low-rate dynamic and static contact angles and the determination of solid surface tensions. *Colloids and Surfaces A: Physicochemical and Engineering Aspects*, 116(1-2):63–77, 1996.

[128] ST Thoroddsen, K Takehara, and TG Etoh. Micro-splashing by drop impacts. *Journal of Fluid Mechanics*, 706:560–570, 2012.

[129] JC Bird, SSH Tsai, and HA Stone. Inclined to splash: triggering and inhibiting a splash with tangential velocity. *New Journal of Physics*, 11(6):063017, 2009.

[130] T C de Goede, N Laan, KG de Bruin, and D Bonn. Effect of wetting on drop splashing of newtonian fluids and blood. *Langmuir*, 34(18):5163–5168, 2017.

[131] TC de Goede, KG de Bruin, and D Bonn. Splashing of impacting drops. *arXiv preprint arXiv:1701.02504*, 2017.

[132] C Lv, P Hao, X Zhang, and F He. Drop impact upon superhydrophobic surfaces with regular and hierarchical roughness. *Applied Physics Letters*, 108(14):141602, 2016.

[133] Y Lee, N Matsushima, S Yada, S Nita, T Kodama, G Amberg, and J Shiomi. Revealing how topography of surface microstructures alters capillary spreading. *Scientific Reports*, 9(1):7787, 2019.

[134] JC Bird, R Dhiman, H-M Kwon, and KK Varanasi. Reducing the contact time of a bouncing drop. *Nature*, 503(7476):385–388, 2013.

[135] C Cao, M Ge, J Huang, S Li, S Deng, S Zhang, Z Chen, K Zhang, SS Al-Deyab, and Y Lai. Robust fluorine-free superhydrophobic pdms–ormosil@ fabrics for highly effective self-cleaning and efficient oil–water separation. *Journal of Materials Chemistry A*, 4(31):12179–12187, 2016.

[136] Stuart A Brewer and Colin R Willis. Structure and oil repellency: textiles with liquid repellency to hexane. *Applied Surface Science*, 254(20):6450–6454, 2008.

[137] RM Rossi, R Stämpfli, A Psikuta, I Rechsteiner, and PA Brühwiler. Transplanar and in-plane wicking effects in sock materials under pressure. *Textile Research Journal*, 81(15):1549–1558, 2011.

[138] EMP Williams, M Dodds, MC Taylor, J Li, and S Michielsen. Impact dynamics of porcine drip bloodstains on fabrics. *Forensic Science International*, 262:66–72, 2016.

[139] C Duprat, S Protiere, AY Beebe, and HA Stone. Wetting of flexible fibre arrays. *Nature*, 482(7386):510–513, 2012.

[140] SA Kooij, AM Moqaddam, TC de Goede, D Derome, J Carmeliet, N Shahidzadeh, and D Bonn. Sprays from droplets impacting a mesh. *Journal of Fluid Mechanics*, 871:489–509, 2019.

[141] E Villermaux and B Bossa. Single-drop fragmentation determines size distribution of raindrops. *Nature Physics*, 5(9):697, 2009.

[142] Y Guo, HS Patanwala, Brice Bognet, and AW Ma. Inkjet and inkjet-based 3d printing: connecting fluid properties and printing performance. *Rapid Prototyping Journal*, 23(3):562–576, 2017.

[143] AA Castrejón-Pita, JR Castrejón-Pita, and GD Martin. A novel method to produce small droplets from large nozzles. *Review of Scientific Instruments*, 83(11):115105, 2012.

[144] JR Castrejon-Pita, WRS Baxter, J Morgan, S Temple, GD Martin, and IM Hutchings. Future, opportunities and challenges of inkjet technologies. *Atomization and sprays*, 23(6), 2013.

[145] I Raza, L Iannucci, and PT Curtis. Introducing a multimaterial printer for the deposition of low melting point alloys, elastomer, and ultraviolet curable resin. *3D Printing and Additive Manufacturing*, 4(2):83–89, 2017.

[146] M Lukić, J Clarke, C Tuck, W Whittow, and G Wells. Printability of elastomer latex for additive manufacturing or 3d printing. *Journal of Applied Polymer Science*, 133(4), 2016.

[147] B Derby and N Reis. Inkjet printing of highly loaded particulate suspensions. *MRS bulletin*, 28(11):815–818, 2003.

[148] KKB Hon, L Li, and IM Hutchings. Direct writing technology—advances and developments. *CIRP Annals*, 57(2):601–620, 2008.

[149] M Forrest. *Recycling and re-use of waste rubber*. Smithers Rapra, 2014.

[150] Rubber Manufacturers Association et al. Scrap tire markets in the united states: 9th biennial report. *Washington, DC. Available from: http://www.rma. org/download/scrap-tires/market-reports/US_ STMarkets2009. pdf (accessed April 11, 2014)*, 2009.

[151] A Aranda Uson, G Ferreira, I Zabalza Bribian, and D Zambrana Vasquez. Study of the environmental performance of end-of-life tyre recycling through a simplified mathematical approach. *Thermal Science*, 16(3), 2012.

[152] RC Kind. The use of tyre crumb as a major ingredient in re-tread compound. *Proceedings of RubberCon. Manchester, United Kingdom*, 2014.

[153] B Derby. Inkjet printing ceramics: From drops to solid. *Journal of the European Ceramic Society*, 31(14):2543–2550, 2011.

[154] JR Castrejón-Pita, GD Martin, SD Hoath, and IM Hutchings. A simple large-scale droplet generator for studies of inkjet printing. *Review of Scientific Instruments*, 79(7):075108, 2008.

[155] Y Matsumoto, N Kobayashi, and H Kawamura. Liquid discharge head and recording device, 2017. KYOCERA Corp, US Patent Application, 15/128,263.

[156] C Brook, A Ristea, M Walsh, and C Gosling. Droplet deposition apparatus and method for manufacturing the same, February 14 2017. US Patent 9,566,786.

[157] J Mueller, D Courty, M Spielhofer, R Spolenak, and K Shea. Mechanical properties of interfaces in inkjet 3d printed single-and multi-material parts. *3D Printing and Additive Manufacturing*, 4(4):193–199, 2017.

[158] J Stringer and B Derby. Formation and stability of lines produced by inkjet printing. *Langmuir*, 26(12):10365–10372, 2010.